Approaching broadband quantum-limited displacement noise in a deformable optical cavity

by

Shannon Reynier Sankar

B.S., University of Florida, 2005

M.S., University of Colorado, 2009

A thesis submitted to the

Faculty of the Graduate School of the

University of Colorado in partial fulfillment

of the requirements for the degree of

Doctor of Philosophy

Department of Physics

2012

This thesis entitled:
Approaching broadband quantum-limited displacement noise in a deformable optical cavity
written by Shannon Reynier Sankar
has been approved for the Department of Physics

_____
Nergis Mavalvala

_____
Konrad Lehnert

Date _____

The final copy of this thesis has been examined by the signatories, and we find that both the content and the form meet acceptable presentation standards of scholarly work in the above mentioned discipline.

Sankar, Shannon Reynier (Ph.D., Physics)

Approaching broadband quantum-limited displacement noise in a deformable optical cavity

Thesis directed by Prof. Nergis Mavalvala

An outstanding goal of the optomechanics community, particularly in the field of gravitational wave detection, is to demonstrate a system with a broadband displacement sensitivity limited by quantum fluctuations of the probe field. This thesis presents significant progress in this direction, namely a means of achieving a sufficiently small off-resonant thermal noise of a deformable optomechanical cavity through the incorporation of a low mass, highly compliant, cryogenically cooled mirror structure with a sensitive motional readout. We conclusively demonstrate the mitigation of Brownian fluctuations in this system by the reduction of the thermal bath temperature, and our measurements are shown to be in close agreement with a finite element analysis of the device. This analysis has been utilized in devising improved oscillator geometries. This work provides a clear path towards the observation of quantum fluctuations in our system and demonstrates the Brownian properties of the crystalline multilayers which make them a promising technology for the realization of low-thermal-noise reflectors in the quantum regime.

Dedication

To my family, for their unwavering love and support.

Acknowledgements

I would firstly like to thank Nergis Mavalvala for being a thoughtful, caring advisor. Nergis was instrumental in getting me involved in this research at MIT and it has been a sincere pleasure to be part of her research team. Her remarkable knowledge, patience and advice have been key to the success of this experiment and to the completion of my doctoral degree.

I also express my gratitude to Konrad Lehnert for being a supportive mentor and also for his scientific advice on cryogenic optomechanics. Additionally, I thank Jun Ye, Cindy Regal, Alan Mickelson and Charles Rogers for serving on my committees.

I thank Thomas Corbitt for his leadership and his knowledge of optomechanics. Without Thomas's involvement, this experiment would likely not have happened and he deserves immense credit for the success we have enjoyed. Together, we built a wonderful experimental framework which I expect will continue to deliver interesting results in the coming years. I have learned much from my interaction with Thomas, and I am absolutely certain he will be very successful as a professor at LSU.

I also acknowledge Markus Aspelmeyer and his exceptional research team, and I thank them for their collaboration with us on this project. In particular, I thank Garrett Cole for fabricating the compliant mechanical oscillators used in our work and for his insight into the modeling of the oscillators by finite element analysis. It is only through Garrett's painstaking effort and attention to detail that we have been able to work with such exceptionally well-suited mechanical devices.

I would like to thank the wonderful people of LIGO, particularly those based at MIT. Our administrative assistant, Marie Woods, deserves special thanks for all her help, especially regarding logistics, organization and purchasing. I thank Lisa Barsotti for sharing an office with me and attempting, albeit

unsuccessfully, to teach me the italian language. I thank Matt Evans for some very interesting and informative discussions, particularly regarding electronics. I thank Sam Waldman for the many discussions we have had about several LIGO subsystems. I thank Mike Zucker for humorous anecdotes, encouragement and for teaching me how one would build a nitrogen-based pulsed laser out of easily available items. I thank Rich Mittleman for our detailed discussions of colloquium topics, and for being a great source of information about cryogenics. I thank Peter Fritschel and Rai Weiss for asking very thought-provoking questions and for their tangible interest in our research.

I thank my family, and my parents in particular, for their love and support. I am continually amazed by their kindness and their encouragement. I am truly lucky to have such a supportive, loving family.

Contents

Chapter

List of Tables

Table

List of Figures

Figure

Chapter 1

Introduction to gravitational waves and their detection

Gravitational waves, which emerge directly from Einstein's Relativity [3, 4, 5, 6, 7], are thought to play a significant role in astronomy. These gravitational waves have never been directly detected, through there has been indirect evidence for their existence - most notably from the Hulse-Taylor pulsar, where the orbital decay is seen to be consistent with the emission of graviational radiation from a binary system [8, 9, 10, 11]. Due to the lack of direct gravitational wave detection, most of the information currently known about the universe has been gleaned from the detection of electromagnetic waves. At several observatories around the world, efforts are currently underway to detect these elusive gravitational waves and perhaps in the process open a new frontier of observational gravitational wave astronomy.

1.1 Gravitational waves from general relativity

To fully understand the method by which these observatories plan to detect gravitational waves, it is necessary to first understand gravitational radiation and its effect on matter. This topic is covered in several textbooks on the subject such as [12, 13] and their canonical method is followed in sections 1.1 and 1.2. For this discussion, geometric units are utilized (the speed of light and Newton's gravitational constant are both set to unity). In those units, the spacetime metric for free space ds (also called the Minkowski metric) can be written in Cartesian coordinates as

$$ds^2 = -dt^2 + dx^2 + dy^2 + dz^2 \tag{1.1}$$

This metric, the simplest of all physically relevant metrics, can be more elegantly expressed in tensor notation

$$ds^2 = \eta_{\mu\nu} dx^\mu dx^\nu \tag{1.2}$$

where the Einstein summation convention is utilized here (and throughout this discussion) and once again Cartesian coordinates are used $x^\mu = \{\text{t, x, y, z}\}$. The Minkowski tensor $\eta_{\mu\nu}$ is defined simply as

$$\eta_{\mu\nu} = \begin{pmatrix} -1 & 0 & 0 & 0 \\ 0 & 1 & 0 & 0 \\ 0 & 0 & 1 & 0 \\ 0 & 0 & 0 & 1 \end{pmatrix} \tag{1.3}$$

This tensor satisfies Einstein's equations, the set of equations which form the core of general relativity and relate the curvature of spacetime with the location and motion of masses and energy. Expressed in simplified form, these equations are written as

$$R_{\mu\nu} - \frac{R}{2} g_{\mu\nu} = 8\pi T_{\mu\nu} \tag{1.4}$$

where $R_{\mu\nu}$ is the Ricci curvature tensor (simply, the application of a second order non-linear differential operator to an arbitrary metric tensor $g_{\mu\nu}$), $R = g^{\mu\nu} R_{\mu\nu}$ is often called the scalar tensor, and $T_{\mu\nu}$ is the stress-energy tensor. The left hand side of equation 1.4 is often re-written as $G_{\mu\nu} = R_{\mu\nu} - \frac{1}{2} g^{\mu\nu} R_{\mu\nu} g_{\mu\nu}$, with $G_{\mu\nu}$ called the Einstein curvature tensor:

$$G_{\mu\nu} = 8\pi T_{\mu\nu} \tag{1.5}$$

This form serves to emphasize that the distribution of mass-energy imposes the curvature of spacetime, upon which free masses must travel along geodesics. There are very few analytic solutions to these equations, with Minkowski space being the easiest to analyze. Perturbation on the Minkowski spacetime is known as weak field general relativity and results in the natural mathematical development of gravitational radiation. To see this, one can now define

$$g_{\mu\nu} = \eta_{\mu\nu} + h_{\mu\nu} \tag{1.6}$$

where $h_{\mu\nu}$ is a small perturbation to the Minkowski tensor $\eta_{\mu\nu}$ or expressly $|h_{\mu\nu}| \ll 1$. From here on, all equations in this discussion will be truncated to linear dependence on $h_{\mu\nu}$. Furthermore, it is noted here that - as with electromagnetic potentials - guage freedom permits changes to $h_{\mu\nu}$ without affecting observables. One commonly used group of gauges is the Lorenz gauge set, characterized by

$$\bar{h}^{\mu\nu}{}_{\nu} = \frac{\delta \bar{h}^{\mu\nu}}{\delta x^{\nu}} = 0 \tag{1.7}$$

where $\bar{h}_{\mu\nu} = h_{\mu\nu} - \frac{1}{2} h^{\alpha}_{\alpha} n_{\mu\nu}$. It is noted at this point that equation 1.7 actually broadly encompasses several possible gauge choices, and further gauge specification will be made in a subsequent section. Without loss of generality, one can now use this gauge set to write the Einstein equations in the weak field limit

$$n^{\alpha\beta} \frac{\delta}{\delta x^{\alpha}} \frac{\delta}{\delta x^{\beta}} \bar{h}^{\mu\nu} = -16\pi T_{\mu\nu} \tag{1.8}$$

The wave nature inherent in the above equation becomes evident when the operator $n^{\alpha\beta} \frac{\delta}{\delta x^{\alpha}} \frac{\delta}{\delta x^{\beta}}$ is written out in, say, Cartesian form as $\nabla^2 - \frac{\delta^2}{\delta t^2}$ where ∇ is the Laplace operator. It is in fact a general tensor form of the wave equation and its solutions are known as Gravitational Waves. Comparison with more familiar wave equations, such as the inhomogeneous wave equations for electromagnetic vector and scalar potentials, already yields useful insight into gravitational waves - they are fluctuations in the local spacetime metric sourced by changes in the stress-energy tensor, and propagating at the speed of light (in these units, unity). Explicitly, solutions will take the form

$$\bar{h}^{\mu\nu}(x^{\mu}) = A^{\mu\nu} \exp(i k_{\mu} x^{\mu}) \tag{1.9}$$

with an amplitude tensor $A^{\mu\nu}$ and a four dimensional wave vector k^{μ}. These solutions are gravitational waves.

1.2 Effect of gravitational waves on free masses

Having now shown that gravitational waves naturally emerge from Einstein's general relativity, and with an eye towards how they could be detected, it is now useful to see the interaction of gravitational waves with matter. For this exercise, it is helpful to resort to the Transverse-Traceless (TT) gauge, which belongs to the Lorenz gauge set used in the previous discussion. The TT gauge is specifically defined by

$$\bar{h}_{\mu 0} = 0 \tag{1.10}$$

which corresponds to the perturbation metric lacking temporal coordinates, and

$$\bar{h}^{\mu}_{\mu} = 0 \tag{1.11}$$

which refers to the fact that the metric is traceless. It should also be noted here that these conditions imply that $\bar{h}^{\mu\nu} = h^{\mu\nu}$ and the bar will be dropped in subsequent discussions. One can write out the perturbation metric in this gauge as

$$h^{(TT)}_{\mu\nu} = \begin{pmatrix} 0 & 0 & 0 & 0 \\ 0 & h_{xx} & h_{xy} & 0 \\ 0 & h_{xy} & -h_{xx} & 0 \\ 0 & 0 & 0 & 0 \end{pmatrix} \tag{1.12}$$

or in terms of basis tensors $\hat{h}_+$ and $\hat{h}_\times$as

$$h^{(TT)}_{\mu\nu} = h_+ \hat{h}_+ + h_\times \hat{h}_\times \tag{1.13}$$

where

$$\hat{h}_+ = \frac{1}{\sqrt{2}} \begin{pmatrix} 0 & 0 & 0 & 0 \\ 0 & 1 & 0 & 0 \\ 0 & 0 & -1 & 0 \\ 0 & 0 & 0 & 0 \end{pmatrix} \tag{1.14}$$

and

$$\hat{h}_\times = \frac{1}{\sqrt{2}} \begin{pmatrix} 0 & 0 & 0 & 0 \\ 0 & 0 & 1 & 0 \\ 0 & 1 & 0 & 0 \\ 0 & 0 & 0 & 0 \end{pmatrix} \tag{1.15}$$

In analogy with equation 1.9, h_+ and $h_\times$ each represents a wave solution of the form

$$h_{+,\times} = A_{+,\times} \exp(ik_\mu x^\mu) \tag{1.16}$$

and equation 1.13 can be understood as representative of two orthogonal graviational wave polarizations which, in linearized theory, independently interact with matter.

This interaction is can be intuitively understood by examining the geodesic deviation equation, which describes the relative changes between two nearby geodesics:

$$\ddot{\xi}^\mu = R^\mu_{\alpha\beta\nu} V^\alpha U^\beta \xi^\nu \tag{1.17}$$

where the vector ξ^μ links the two geodesics where $R^\mu_{\alpha\beta\nu}$ is the Riemann tensor. V^α and U^β are the particle velocity spacetime vectors. In the weak perturbative limit where $|h_{\mu\nu}| \ll 1$, the Riemann tensor is

$$R^\mu_{\alpha\beta\nu} = \frac{1}{2}\eta^{\mu\sigma}\left(h_{\sigma\beta,\nu\alpha} + h_{\nu\alpha,\sigma\beta} - h_{\sigma\alpha,\nu\beta} - h_{\nu\beta,\sigma\alpha}\right) \tag{1.18}$$

With these two equations in mind, one may consider the situation of two particles initially at rest, separated by an initial distance ϵ in the x-direction interacting with a gravitational wave travelling in the z-direction. The vectors in the above equation become $\xi^\mu = (0, \epsilon, 0, 0)$ and $V^\alpha = U^\beta = (1, 0, 0, 0)$, and the geodesic deviation equation becomes

$$\ddot{\xi}^\mu = -\epsilon R^\mu_{0x0} \tag{1.19}$$

Inserting the derived expressions for $h^{\mu\nu}$ in the TT gauge into equation 1.18 one can reduce equation 1.19 above simply to

$$\begin{aligned} \ddot{\xi}^x &= \tfrac{1}{2}\epsilon\ddot{h}_+ \\ \ddot{\xi}^y &= \tfrac{1}{2}\epsilon\ddot{h}_\times \end{aligned} \tag{1.20}$$

A similar analysis for particles separated in the y-direction yields

$$\begin{aligned} \ddot{\xi}^x &= \tfrac{1}{2}\epsilon\ddot{h}_\times \\ \ddot{\xi}^y &= -\tfrac{1}{2}\epsilon\ddot{h}_+ \end{aligned} \tag{1.21}$$

These equations reveal that the free masses oscillate about their rest positions in spacetime, with a frequency equal to the gravitational wave frequency. Using the results in equations 1.20 and 1.21 above, the effect of

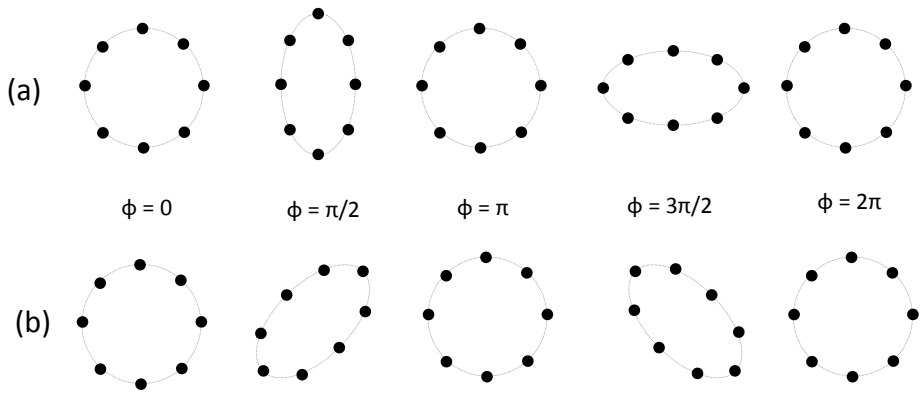

Figure 1.1: Qualitative representation of the effect of the passage of a gravitational wave on an initially circular ring of masses, for (a) + polarization and (b) × polarization. Φ is the phase of the gravitational wave as it passes.

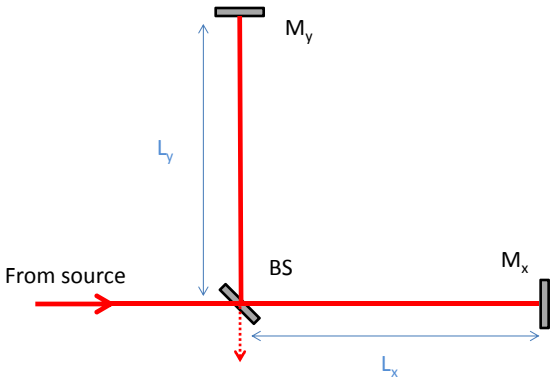

Figure 1.2: A canonical Michelson interferometer, consisting of mirror M_x, M_y and beamsplitter BS, is sensitive to differential arm length changes as discussed in the text.

the passage of one period of a gravitational wave on a ring of particles is qualitatively illustrated in figure 1.1. A detector of gravitational waves must be capable of measuring this motion, a criterion which is naturally achieved utilizing a Michelson interferometer. It is noted here that equations 1.20 and 1.21 lend themselves to the characterization of a strain amplitude, or a length change per unit separation. Gravitational wave detectors are often characterized by this strain sensitivity.

Figure 1.2 shows a canonical Michelson interferometer. As the beam propagates from the beamsplitter

to the end reflectors and back, it will acquire a phase ϕ of

$$\phi_{x,y}(t) = \frac{4\pi}{\lambda} L_{x,y}(t) \tag{1.22}$$

where λ is the beam wavelength and L is the length of the Michelson arm. Upon recombination at the beamsplitter, the beams will have a phase difference of

$$\Delta\phi(t) = \phi_x(t) - \phi_y(t) = \frac{4\pi}{\lambda} \left[L_x(t) - L_y(t)\right] \tag{1.23}$$

and by measuring this phase difference, information about relative changes of the proper length of the arms is obtained. This phase difference is basically ω times the difference in travel time perturbations of the beams returning to the beamsplitter. In the simplest case of a Michelson oriented in with arms in the $\hat{x}$ and $\hat{y}$ directions, and a gravitational wave with + polarization propagating in the $\hat{z}$ direction, there will be equal and opposite perturbations in the light travel time in the two arms [13]. If the period of the graviational wave is large compared to the round-trip travel time of the light in the arms, the phase shift can be written as

$$\Delta\phi(t) = h(t)\frac{4\pi L}{\lambda} \tag{1.24}$$

where the gravitational wave is assumed to have an amplitude of $h_{11} = -h_{22} = h$. There are several known techniques for extracting this phase information, including the Pound-Drever-Hall-type RF sideband method [14, 15] and DC homodyne readout [16, 17, 18].

1.3 LIGO

Now, having motivated the use of the Michelson interferometer in the previous section, the scientific implementation of this design is discussed. One of the most widely-known realizations of the Michelson design as a gravitational wave detector is the Laser Interferometer Gravitational wave Observatory, known by the acronym LIGO [19, 20].

LIGO was designed as a pioneering dual-site large-scale observatory focused primarily on the search for elusive gravitational radiation from astronomical sources. When construction of LIGO began in 1992, it represented the largest single experimental undertaking of the National Science Foundation - after several

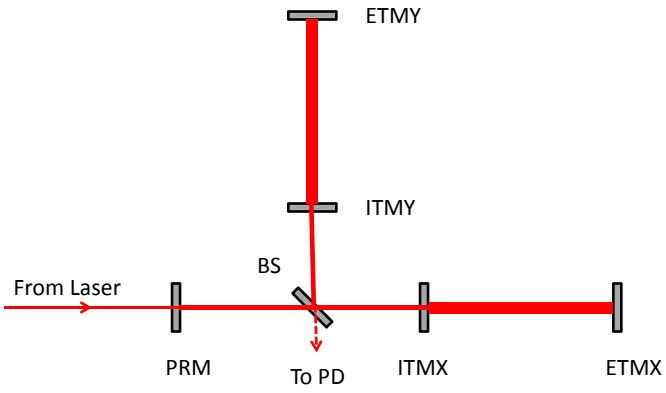

Figure 1.3: Basic overview of the LIGO interferometer. For simplicity, several key subsystems are not shown. Optics shown include Power Recycling Mirror (PRM), 50/50 beamsplitter (BS), input test masses (ITMX, ITMY) and end test masses (ETMX, ETMY). The photodiode is denoted PD.

years of extensive experimental feasibility studies performed largely at a 40m test facility at the California Institute of Technology and a 5m test facility at the Massachusetts Institute of Technology. The two sites chosen for housing the observatories are in Livingston Loiusiana and Hanford Washington, and form part of a global array of gravitational wave detectors, including the Italian-French-Dutch VIRGO interformeter (in Italy) [21, 22, 23, 24, 25] and the German-British interferometer GEO600 (in Germany) [26, 27, 28].

1.3.1 Description of the interferometer

A schematic representation of the LIGO interferometer is shown in figure 1.3. There are several key differences between this design and that of the canonical Michelson. Firstly, the arms of the interferometer consist of optical Fabry-Perot cavities. This feature serves to improve the phase sensitivity of the interferometer, by boosting the phase response due to a given change in length of the arms. The topic of such optical cavities is discussed in more detail later in the thesis. Secondly, a mirror (known as the Power Recycling Mirror, or PRM) is placed at the symmetric port of the interferometer. Since the interferometer is operated to have a dark fringe (destructive interference) at the anti-symmetric port, the PRM reflects light back toward the beamsplitter and serves to increase the optical power stored in the interferometer. In effect, the

PRM forms a resonant cavity with the rest of the interferometer. Together, these features reduce technical and fundamental noise sources, and make the detector several orders of magnitude more sensitive than a canonical Michelson interferometer.

Furthermore, the beamsplitter and mirrors are all suspended from seismic isolation-stages, with both passive and active forms of isolation. The mirror suspensions permit the optical elements to behave as free masses over significant frequency bands (this point is discussed in more detail in chapter 2).

1.3.2 LIGO Performance and predicted detectable event rate

LIGO has performed several stretches of data acquisition (in addition to one shorter data run, S6), all interspersed between upgrades and technical improvements. Known as science runs, these periods are denoted S1, S2, S3, S4, S5 and S6, and are each several months long. A representative noise spectrum for science run S5 is shown in figure 1.4 and demonstrates that the interferometers operate at, or near, LIGO design goals over a large range of frequencies.

Despite having met the design goals, the rate of detectable events is quite low. The detectable event rate is defined as the predicted average rate of detection of a gravitational wave from a particular type of astrophysical source in a specified period of time, such as a year. It therefore takes into account the sensitivity of the detector, the expected signal strength and the number of such astrophysical events occuring per unit time in our cosmological vicinity. For instance, two reasonable indicators for detectable event rates are the frequency of detecting the coalescense of a neutron star and black hole binary system (NS-BH rate), and the frequency of detecting a pair of black holes in a binary system (BH-BH rate). For the first phase of LIGO, also known as initial LIGO or iLIGO, the NS-BH detection event rate is approximately 0.05 per year and that of a BH-BH system is, optimistically, 1 per year [29] .

These low predicted rates have been known for a long time and therefore, although initial LIGO is the most sensitive detector ever constructed, it has always been viewed as a stepping stone to a more sensitive detector. In order to perform observational gravitational wave astronomy, a detector with improved sensitivity is necessary - Advanced LIGO is the realization of that aim.

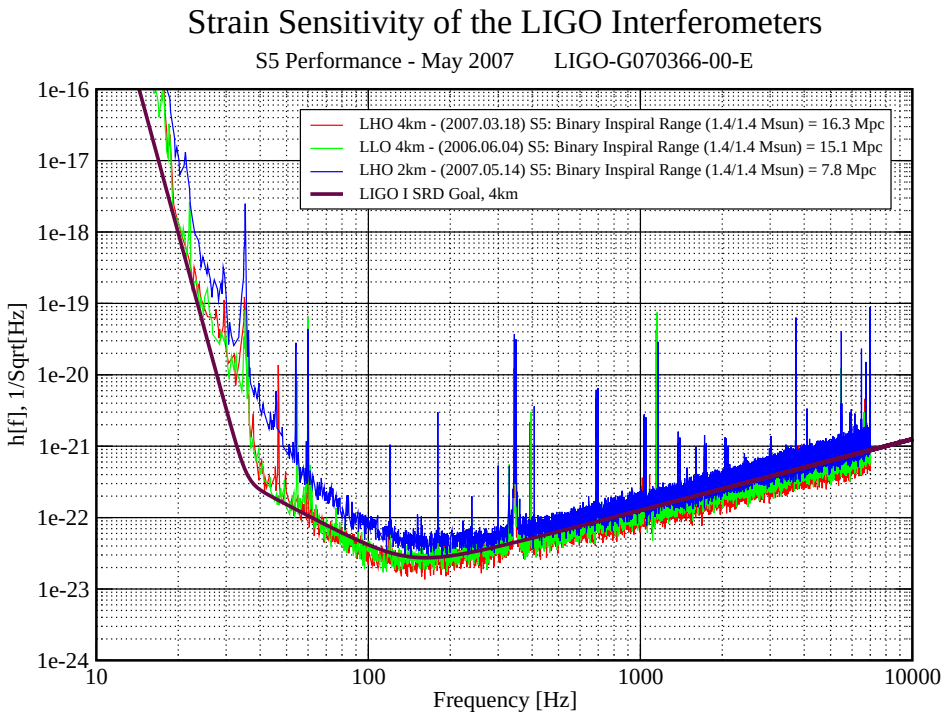

Figure 1.4: Representative noise curves for the 5th LIGO science run and comparison to target sensitivity. Noise is expressed as a strain (the displacement change per unit arm length). Plot obtained from the LIGO Document Control Center [1].

Merger type	LIGO	Advanced LIGO
NS-BH	0.05 yr^{-1}	400 yr^{-1}
BH-BH	1yr^{-1}	500-7300 yr^{-1}

Table 1.1: Estimated detectable event rate for LIGO and Advanced LIGO for two astrophysical merger categories.

1.4 Advanced LIGO

Advanced LIGO will be the most sensitive displacement detector yet constructed when it becomes operational in 2014 [30, 31, 32]. The predicted detectable event rates for a NS-BH binary in Advanced LIGO is estimated to be approximately 400 per year, and BH-BH events are expected to be detected between 500 and 7300 times per year [29] . The comparison of the detection rate is summarized in table 1.1.

The upgrade to Advanced LIGO has already begun. It involves improvements to several key areas of

the interferometers [33], including:

- The introduction of a signal recycling cavity (SRM). The SRM is to be placed at the asymetric port of the interferometer and serves to return light containing a gravitational wave signal into the interferometer to accrue more signal. The cavity formed by the interferometer and the SRM allows tuning of the interferometer sensitivity.

- Upgrades to the input optics and the main laser to allow for more optical power entering the interferometer. The mass of the mirrors is increased to mitigate the effect of higher radiation pressure due to more optical power.

- High quality optical coatings and upgrades to thermal compensation systems. Furthermore, the arm cavities will be close to confocal - making the beam on the mirrors as large as possible - to lower the sensitivity to coating thermal noise.

- Improvement to the mirror suspension system to provided more environmental isolation and better thermal noise performance.

Coupled with existing infrastructure, as well as many other upgrades, these improvements result in an Advanced LIGO estimated noise floor shown in figure 1.5. The displacement sensitivity, in the frequency band of maximum sensitivity, is limited only by quantum effects and the thermal noise of the reflective mirror surface - two noise sources studied in this thesis.

1.5 Relation to thesis

As can be seen in figure 1.5, in addition to a coating thermal noise contribution near 100Hz, the dominant source of imprecision results directly from the quantum fluctuations. Briefly, the thermal noise contribution is due to the Brownian motion of the reflective surface. The quantum noise, on the other hand, is a source of imprecision caused by the shot noise of the probe light and the momentum transfer of the photons reflected off the mirror (called quantum radiation pressure). These two quantum noise sources combine to produce the standard quantum limit, where the imprecision due to shot noise is equal to that

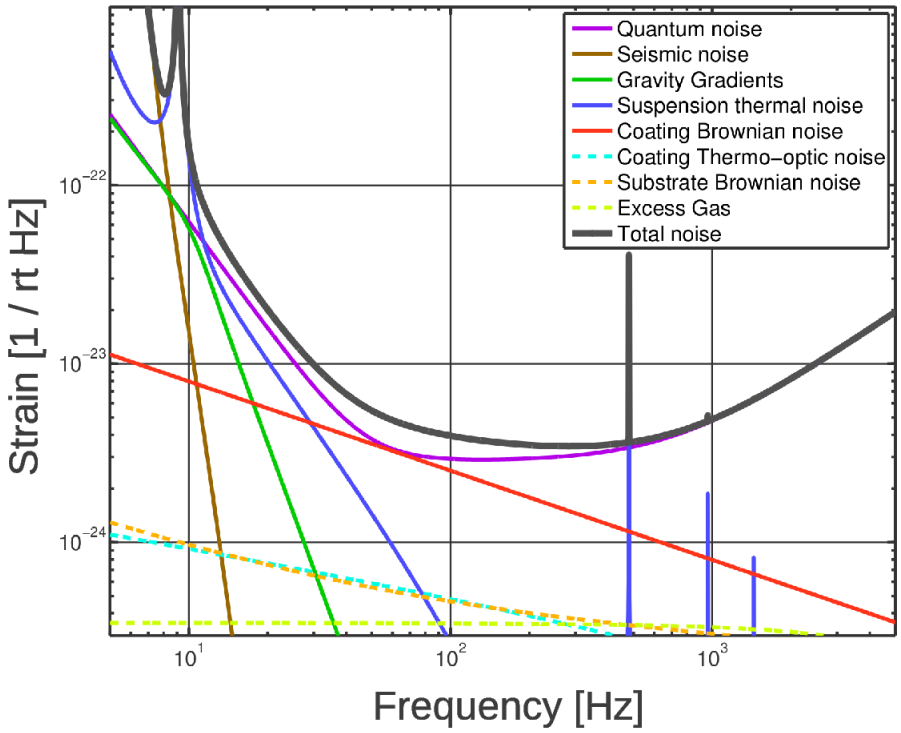

Figure 1.5: Advanced LIGO noise budget. To convert strain to displacement noise, simply multiply by the arm length (4km). Plot reproduced from [2].

due to radiation pressure and the total quantum noise is at a minimum. These noise sources will be further discussed in chapter 2.

In the body of research covered by this thesis, the experimental groundwork is laid for the detection of these important noise sources in a small-scale tabletop experiment before it is encountered in Advanced LIGO. This work opens up future avenues for the possible mitigation of the limiting noises, thereby resulting in the possibility of even more sensitive gravitational detectors in the future, and consequentially an improvement in our ability to observe the universe through gravitational radiation.

In this tabletop experiment, a 1 cm long optical cavity (similar to a scaled-down version of one arm of the LIGO interferometer) is probed with a low noise laser source. One of the mirrors is a essentially a "free-standing optical coating" and is designed to be free to move under the influence of forces due to the light. This motion is monitored using the transmitted cavity beam. The thermal motion of this movable mirror presents the largest obstacle to the detection of this quantum source of motion, and is mitigated by

cooling the optical cavity in a liquid helium cryostat. The long term goals of this experiment are:

- To measure the standard quantum limit in the broadband motional spectrum. The first step in this goal is to observe quantum radiation pressure noise as a significant contribution to the total measured displacement noise.

- To develop and investigate techniques for the mitigation of quantum noise, as this aim has much potential for Advanced LIGO and other advanced detectors. In addition to the mitigation of this noise source, the manipulation of quantum noise using optomechanical devices is also of prime interest. One class of these devices, commonly referred to as a quantum filter cavity, offers the incentive of possibly further reducing the quantum readout noise in the detection band of Advanced LIGO.

- To develop optomechanical devices which are sensitive to the quantum nature of the probe light. This goal involves both designing the most effective geometry, as well as investigating the types of materials which give optimum performance.

This thesis presents significant progress toward these ultimate goals and is organized as follows: Chapter 1 has provided the context of the experiment to the broader academic community, particularly regarding gravitational wave detection and Advanced LIGO. Chapter 2 advocates the use of compliant mechanical oscillators as broadband displacement sensors of weak forces and derives the fundamental sources of noise in such an optomechanical system. Chapter 3 describes the physical implementation of that concept in this experiment, including oscillator design, fabrication and modeling. The inclusion of the oscillator into an optical cavity is analyzed. Chapter 4 documents the experimental apparatus and its function, particularly for future graduate students for whom details of the system's implementation and function will be crucial. Chapter 5 analyzes suggestions for improving the future performance of the system, with a view to being quantum-limited in a broad frequency band. Finally, Chapter 6 offers concluding remarks and summarizes the accomplishments of this body of research.

Chapter 2

Noises of Interest

2.1 Compliant oscillators as free masses

In chapter 1, it was demonstrated that gravitational radiation produces a measureable displacement change on a free mass. In fact, the ideal broadband transducer of a minuscule force is a free mass - an object for which all stronger forces balance out exactly, leaving behind only the small force one intends to measure as the sole unbalanced push or pull. If the resulting motion of the free mass can be measured, one can then deduce information about the weak causative unbalanced force. However, in a terrestrial environment, it is difficult to produce a truly free mass. In this section, the method for simulating a free mass in a particular frequency band, is detailed. This method is utilized by all earth-bound interferometric gravitational wave detectors, including LIGO and Advanced LIGO detectors.

A free mass is described by the equation

$$m\ddot{x} = F_{\text{drive}} \tag{2.1}$$

where the product of mass m and the acceleration $\ddot{x}$ is equal to a small applied force F_{drive}. It is often the case that it is easier experimentally to measure x, and deduce F_{drive} from the measurement. In the frequency domain, solution to the free mass equation is given by

$$x_{\text{free}}(\omega) = -\frac{F_{\text{drive}}}{m\omega^2} \tag{2.2}$$

One can then tailor the response of the measurement sensor to closely mimic a free mass, at least within the measurement band. Consider now the response of a classical harmonic oscillator, such as a mass-on-a-spring

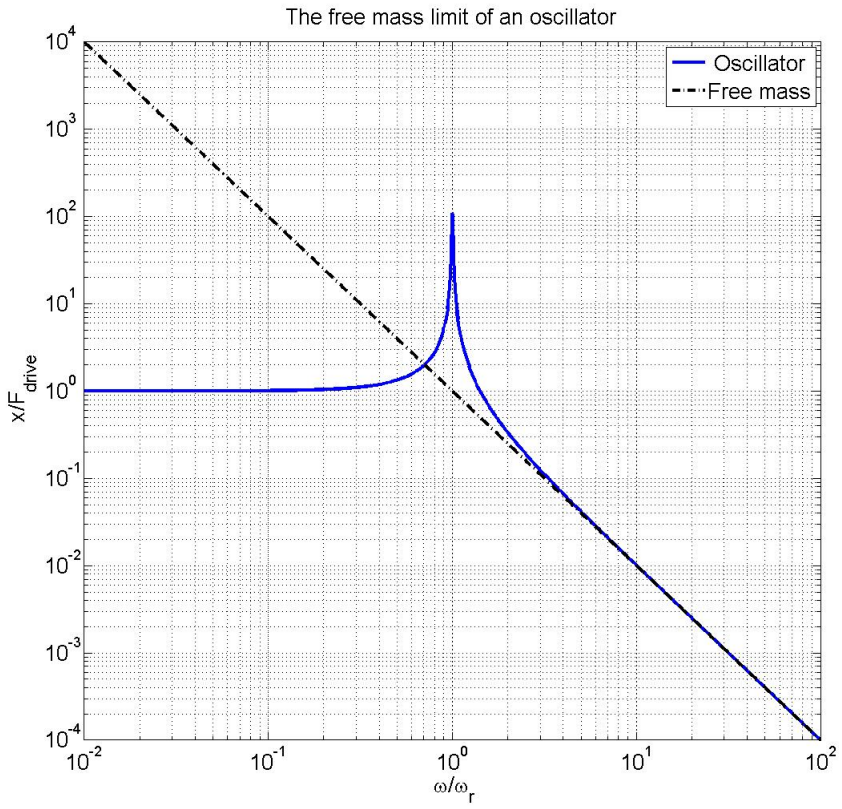

Figure 2.1: The displacement per unit applied force for a compliant oscillator and a free mass. The response of the oscillator mimics that of the free mass in the limit $\omega \gg \omega_r$.

or a pendulum, connected to the drive. For an oscillator of mass m and with resonant frequency $\omega_{\rm r} = 2\pi f_{\rm r}$, its motion due to an applied force is described by the equation

$$m\ddot{x} + m\omega_{\rm r}^2 x = F_{\rm drive} \tag{2.3}$$

which has a solution given in the frequency domain by

$$x_{\rm osc}(\omega) = -\frac{F_{\rm drive}}{m(\omega^2 - \omega_{\rm r}^2)} \tag{2.4}$$

In the limit $\omega \gg \omega_r$ it is clear from equations 2.2 and 2.4 that $x_{\rm osc} \to x_{\rm free}$ and the oscillator response mimics that of the free mass. One can use a sufficiently low frequency oscillator to mimic the response of a free-mass for frequencies higher than the oscillator resonant frequency. This fact is illustrated in figure 2.1.

2.1.1 The fluctuation-dissipation theorem

The fluctuation-dissipation theorem [34, 35] states that thermodynamic noise will result from any non-reversible dissipation process. At non-zero temperature, any oscillator with non-zero damping of a driving force will exhibit spontaneous fluctuations. Specifically, these fluctuations can be considered a thermal driving force with a spectral density given by

$$F_{th}^2(\omega) = 4k_B T \Re(Z) \tag{2.5}$$

where $\Re(Z)$ is the real part of the mechanical impedance Z. Similarly, the motional noise of the mass will be given by

$$x^2(\omega) = \frac{4k_B T}{\omega} \Re(Y) \tag{2.6}$$

where $\Re(Y)$ denotes the real part of the mechanical admittance $Y = Z^{-1}$.

2.1.2 Thermal motion of the ideal single oscillator

Now, having made the case for the use of highly compliant mechanical oscillators as a substitute for a truly free mass, it is time to take into account the thermally driven motion of the mechanical element [35]. The equations of section 2.1 ignore the dissipation present in real oscillators. This dissipation results in fluctuations which, in some cases, may be comparable to (or larger than) quantum fluctuations and thus limit quantum measurement [36].

This damping can be represented via a modification of Hooke's Law to include an imaginary component to the spring constant

$$F = -k\left(1 + i\phi(\omega)\right)x \tag{2.7}$$

where $\phi(\omega)$ is known as the loss angle. The equation of motion then becomes

$$m\ddot{x} + k\left(1 + i\phi(\omega)\right)x = F_{\text{th}} \tag{2.8}$$

where $F_{\text{th}}^2 = 4k_B T \dfrac{k\phi(\omega)}{\omega}$ is the equivalent thermal driving term. Solving the equation of motion in the frequency domain is simple and results in thermal Brownian motion x_{th} given by

$$x_{\text{th}}^2(\omega) = \frac{4k_B T k\phi(\omega)}{\omega\left[\left(k - m\omega^2\right)^2 + \left(k\phi(\omega)\right)^2\right]} \tag{2.9}$$

It is also noted here that this result satisfies the fluctuation-dissipation theorem in equations 2.5 and 2.6, with a mechanical impedance of

$$Z = \frac{k\phi(\omega)}{\omega} + i\omega m + \frac{k}{i\omega} \tag{2.10}$$

and a mechanical admittance given explicitly by

$$Y = \frac{\omega k\phi(\omega) + i\omega(k - m\omega^2)}{(k - m\omega^2)^2 + (k\phi(\omega))^2} \tag{2.11}$$

Note that the frequency dependence of the loss angle impacts the off-resonant thermal spectrum of the oscillator. This feature is discussed in more detail in subsection 2.1.4.

2.1.3 Thermal motion of a distributed-mass oscillator

The canonical ideal oscillator is a massless spring connected to a point mass. However, this notion is often insufficient to describe real-world mechanical oscillators. Often it is necessary to work with distributed mass systems. Consider one such system of length L and mass density distribution $\rho(x)$, analyzed in the method of [35]. In general, the system will possess normal modes $\psi_n(x)$ where

$$\int_0^L \rho(x)\psi_n(x)\psi_m(x)dx = \delta_{nm} \tag{2.12}$$

expresses modal orthogonality. δ_{nm} is the usual Kronecker delta. Any arbitrary displacement $y(x,t)$ of the oscillator can be expressed in terms of these orthogonal modes as

$$y(x,t) = \sum_{n=1}^{\infty} \psi_n(x)q_n(t) \tag{2.13}$$

where $q_n(t)$ is a generalized variable, denoting the displacement contribution due to the n-th mode at a time t. Switching to the frequency domain and assuming (without loss of generality) that the n-th mode damps according to a particular loss angle $\phi_n(\omega)$, the equation of motion can be written then as

$$\ddot{q}_n(\omega) + \omega_n^2 \left[1 + i\phi_n(\omega)\right] q_n(\omega) = Q_n(\omega) \tag{2.14}$$

where $Q_n(\omega)$ is the generalized force on the n-th mode, and can be computed from a distributed force density $f(x,\omega)$ by

$$Q_n(\omega) = \int_0^L f(x,\omega)\psi_n(x)dx \tag{2.15}$$

Specifically, if a force F is applied at one end $x = L$ of the system, the generalized force can be explicitly written as $Q_n = F\psi_n(L)$ and the equation of motion can be solved, giving the displacement of the n-th mode in terms of its respective q_n as

$$q_n(\omega) = \frac{F\psi_n(L)}{(1 + i\phi_n(\omega))\,\omega_n^2 - \omega^2} \tag{2.16}$$

One can revert to the usual spatial coordinates from the generalized q using the frequency domain version of equation 2.13, giving

$$y(L,\omega) = \sum_{n=1}^{\infty} \frac{F\psi_n^2(L)}{(1 + i\phi_n(\omega))\,\omega_n^2 - \omega^2} \tag{2.17}$$

The admittance $Y = \dfrac{\dot{y}}{F}$ can be now written as $\dfrac{i\omega y(\omega)}{F}$ and the displacement noise at $x = L$ due to thermal fluctuations can be written explicitly from the fluctuation-dissipation theorem as

$$x^2(\omega) = \frac{4k_BT}{\omega} \sum_{n=1}^{\infty} \frac{\psi_n^2(L)\phi_n(\omega)\omega_n^2}{\left(\omega_n^2 - \omega^2\right)^2 + \phi_n^2(\omega)\omega_n^4} \tag{2.18}$$

The thermal noise of many real world oscillators take the form of equation 2.18 above, including the initial LIGO and Advanced LIGO test masses, certain suspension systems and coatings on optical elements. Comparing equations 2.9 and 2.18, it is clear that the distributed system can be considered to the weighted sum of many ideal oscillators. The relative weights (that is, the coupling of each mode to the measurement) can be thought of as an effective mass of that mode.

2.1.4 On the loss angle ϕ

Damping occurs as a result of irreversible energy loss. The mechanism by which this energy loss occurs may vary from one system to the next and, therefore, the functional form of the loss angle $\phi(\omega)$ is not universal. For instance, one particular type of damping (commonly called viscous damping) comes from a frictional force proportional to the velocity $\vec{F}_{\text{vis}} = -C\vec{v}$. In this case, the loss angle will increase proportionally with frequency $\phi_{\text{vis}} = \dfrac{C}{k}\omega$. Another case is that of structural damping, where the loss angle is constant over all frequencies. Yet another source of energy dissipation is called thermo-elastic damping, and occurs when bending a structure induces thermal gradients and the resulting heat flow dissipates energy.

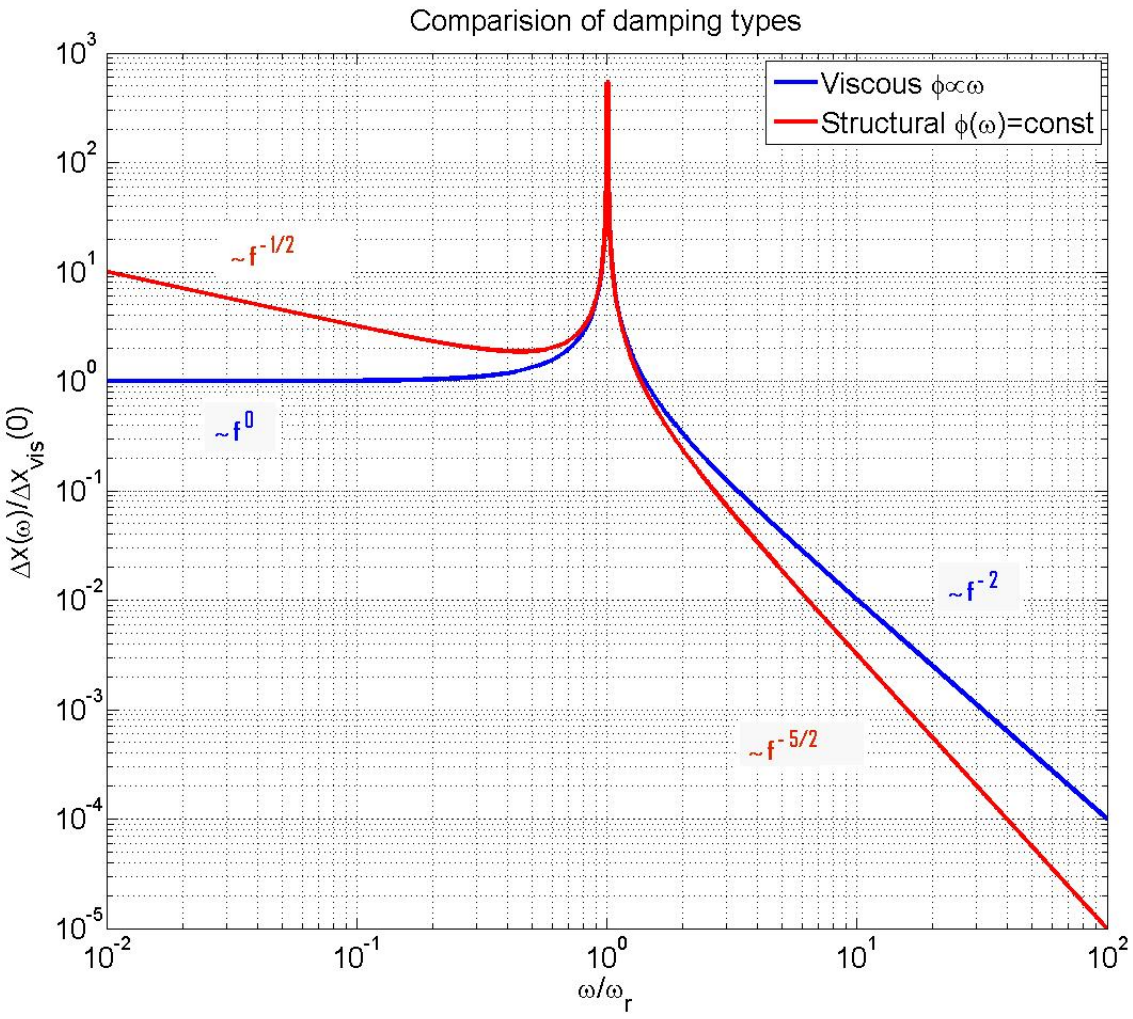

Figure 2.2: The thermal noise of an arbitrary oscillator from structural damping (red) compared to the thermal noise due to viscous damping (blue). Note that the y-axis is normalized to the DC displacement noise from viscous damping and is therefore unitless.

There are several other forms of damping and, as shown in equations 2.9 and 2.18 and figure 2.2, this affects the thermal noise spectrum. In systems operating in the free-mass regime, structural damping is generally preferred due to the faster fall-off of thermal noise above resonance.

A related variable is the mechanical quality factor Q_m. It is generally defined as the ratio of the stored energy to the energy lost during one radian of oscillation or, for high Q_m, the ratio of the resonant frequency to the full-width at half maximum of that resonance. Q_m is an important and often-quoted variable for experiments which occur at the mechanical resonance frequency, or for broadband experiments where

structural damping is present. For the latter, the two quantities are related by

$$\phi_{\text{struct}} = \frac{1}{Q_m} = \text{constant} \tag{2.19}$$

However, in the general sense, when the functional form of the broadband thermal noise is required it is more common to show the loss angle as a function of frequency.

2.2 Quantum noise

The quantum noise in interferometers like Advanced LIGO can be subdivided into two main categories: quantum shot noise and quantum radiation pressure noise. Before looking specifically at these noise sources, it is helpful to understand the origins of quantum noise in an optical system.

2.2.1 Introduction to quantum noise

An ideal laser beam can be thought of as a canonical coherent state $|\alpha\rangle$ (see [37, 38]), which is an eigenstate of the annihilation operator $\hat{a}$ and is therefore explicitly defined by the eigenequation

$$\hat{a}\,|\alpha\rangle = \alpha\,|\alpha\rangle \tag{2.20}$$

At the same time, the single-mode electric field operator $\hat{E}$ can be represented in the form

$$\hat{E} = \sqrt{\frac{\hbar\omega}{2V\epsilon_0}}(\hat{a}^\dagger e^{-i\phi} + \hat{a}e^{i\phi}) \tag{2.21}$$

where $\phi = \dfrac{2\pi z}{\lambda} + \omega t$ is the accumulated phase for an optical frequency ω, V is the mode volume, ϵ_0 and $\hbar$ are fundamental constants representing the permittivity of free space and the reduced Planck's constant, respectively. Re-writing equation 2.21 explicitly in terms of real and imaginary parts, one arrives at

$$\hat{E} = \sqrt{\frac{2\hbar\omega}{V\epsilon_0}}(\hat{X}_1\cos(\phi) + \hat{X}_2\sin(\phi)) \tag{2.22}$$

where $\hat{X}_1 = \dfrac{1}{2}(\hat{a} + \hat{a}^\dagger)$ and $\hat{X}_2 = \dfrac{1}{2i}(\hat{a} - \hat{a}^\dagger)$. It is clear that the individual sine and cosine quadratures have identical variances

$$(\Delta X_1)^2 = (\Delta X_2)^2 = \frac{1}{4} \tag{2.23}$$

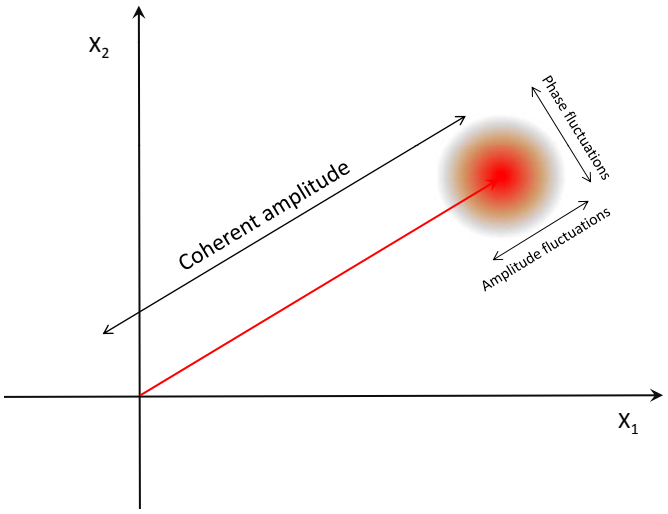

Figure 2.3: Ball and stick representation of a coherent state.

if the electric field is measured in units of $\sqrt{\frac{2\hbar\omega}{V\epsilon_0}}$. Figure 2.3 qualitatively illustrates the existence of these fluctuations on the coherent field, and is commonly called the ball-and-stick representation. It is clear from this representation that the fluctuations on the coherent state occur in both amplitude and phase quadratures of the stick vector. These quadrature fluctuations, when considered in the context of an optical resonator or interferometer, result in quantum radiation pressure and shot noise, respectively.

2.2.2 Optical shot noise

Optical shot noise originates from the fact that the number of photons arriving at a photodetector fluctuates in any given measurement time interval. To understand this concept one should first express the coherent state in terms of Fock states $|n\rangle$, which are a complete set of orthogonal basis states. One arrives at

$$|\alpha\rangle = \sum_{n=0}^{\infty} |n\rangle \langle n| \alpha\rangle = \sum_{n=0}^{\infty} \frac{\alpha^n}{\sqrt{n!}} \langle 0| \alpha\rangle |n\rangle \tag{2.24}$$

The factor $\langle 0| \alpha\rangle$ can be obtained from the normalization condition for coherent states, $\langle \alpha| \alpha\rangle = 1$, as

$$1 = \langle \alpha| \alpha\rangle = \sum_n \sum_m \langle m| n\rangle \frac{(\alpha^\star)^m \alpha^n}{\sqrt{m!}\sqrt{n!}} = e^{|\alpha|^2} |\langle 0| \alpha\rangle|^2 \tag{2.25}$$

which results in

$$\langle 0|\ \alpha\rangle = e^{-\frac{|\alpha|^2}{2}} \tag{2.26}$$

and therefore the coherent state can be written out in terms of number states from equation 2.24 as

$$|\alpha\rangle = e^{-\frac{|\alpha|^2}{2}} \sum_{n=0}^{\infty} \frac{\alpha^n}{\sqrt{n!}} |n\rangle \tag{2.27}$$

The probability $P(n)$ of finding photon number n in coherent state $|\alpha\rangle$ is then

$$P(n) = |\langle n|\ \alpha\rangle|^2 = \frac{e^{-|\alpha|^2} |\alpha|^{2n}}{n!} \tag{2.28}$$

which is a Poissonian distribution. The mean photon number $\langle \hat{n} \rangle = \sum_{n=0}^{\infty} nP(n)$ is then

$$\langle \hat{n} \rangle = |\alpha|^2 \tag{2.29}$$

and the variance $(\Delta \hat{n})^2 = \langle \hat{n}^2 \rangle - \langle \hat{n} \rangle^2$ is also

$$(\Delta \hat{n})^2 = |\alpha|^2 \tag{2.30}$$

As seem from the previous two equations, the variance and mean of the photon number for a coherent state are equal. Writing this out explicitly, one arrives at

$$\Delta \hat{n} = \sqrt{\langle \hat{n} \rangle} \tag{2.31}$$

If we consider measuring the power P_{meas} of an optical beam over a long time interval τ, the mean photon number can be re-written as $\langle \hat{n} \rangle = \left\langle \frac{dn}{dt} \right\rangle \tau$ where

$$\left\langle \frac{dn}{dt} \right\rangle = \frac{P_{\text{meas}}}{\hbar \omega_{\text{opt}}} = \frac{P_{\text{meas}} \lambda}{2\pi \hbar c} \tag{2.32}$$

is the mean number of photons per unit time detected. Here $\lambda = \frac{2\pi\hbar c}{\omega_{\text{opt}}}$ is the wavelength of the optical beam. Using this notion, equation 2.31 can be re-written as

$$\Delta \hat{n} = \sqrt{\frac{P_{\text{meas}} \lambda}{2\pi \hbar c} \tau} \tag{2.33}$$

If one assumes the measured power P_{meas} carries information about the displacement of a test mass, one can convert this uncertainty in photon number to an uncertainty in displacement. However, in general, the

functional form of the power change per unit length $\frac{dP_{\rm meas}}{dl}$ must first be known before applying the relation $\Delta x_{\rm shot} = \frac{\Delta\hat{n}}{\langle\hat{n}\rangle}\left(\frac{1}{P_{\rm meas}}\frac{dP_{\rm meas}}{dl}\right)^{-1}$. More concretely,

$$\Delta x_{\rm shot}(\tau) = \sqrt{\frac{2\pi\hbar c}{P_{\rm meas}\lambda\tau}}\left(\frac{1}{P_{\rm meas}}\frac{dP_{\rm meas}}{dl}\right)^{-1} \tag{2.34}$$

The conversion factor often depends on exact interferometer topology. For instance, the frequency response of the LIGO and Advanced LIGO arm cavities gives a shot noise floor which increases with frequency, as seen in figure 1.4 and 1.5. One way of thinking of this floor is that higher sideband frequencies possess less power due to the arm cavity response, thus the shot noise increases. Nevertheless, in the simplest case of a canonical Michelson with a flat interferometer response, one can determine that

$$\Delta x_{\rm shot}(\tau) = \sqrt{\frac{\hbar c\lambda}{4\pi P_{\rm in}\tau}} \tag{2.35}$$

at a power $P_{meas} = P_{out} = \frac{P_{in}}{2}$ where the power change per unit differential displacement is $\frac{dP_{\rm meas}}{dl} = \frac{2\pi}{\lambda}P_{\rm in}$. In the frequency domain, these length fluctuations can be re-written

$$\Delta x_{\rm shot}(f) = \sqrt{\frac{\hbar c\lambda}{2\pi P_{\rm in}}} \tag{2.36}$$

where the factor of $\sqrt{2}$ comes from the use of a one-sided spectral density. It is noted here, and discussed further in section 2.3, that the uncertainty due to shot noise in a displacement measurement scales as $P^{-\frac{1}{2}}$.

2.2.3 Quantum radiation pressure noise

The other manifestation of quantum noise is referred to as quantum radiation pressure noise. This noise type can be characterized as an uncertainty in a test mass position due to quantum fluctuations of the electromagnetic field imparting momentum onto the test mass. In the case of an optical interferometer, the photons bouncing off the mirrors induce motion in the mirrors, and this motion is sensed. In effect, the measurement field induces uncertainties in the measurement - for this reason, quantum radiation pressure noise can be thought of as a manifestation of quantum backaction.

Consider an optical beam of power P hitting a perfectly reflective moveable mirror, as illustrated in figure 2.4. The force imparted on the mirror due to the light is given by

$$F_{\rm RP} = \frac{2P}{c} \tag{2.37}$$

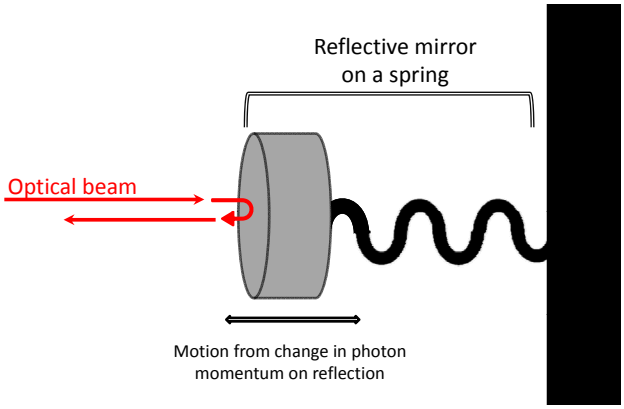

Figure 2.4: Light bouncing off a perfectly reflective movable mirror, represented here by a mass on a spring. Discussed further in the text.

Note here that the force contains a DC frequency component, due to the average field hitting the mirror, as well as a fluctuating component which originates in the shot noise fluctuations. These power fluctuations can be expressed as $\Delta P = \frac{2\pi\hbar c}{\lambda}\Delta\hat{n}$, giving a fluctuating force of

$$\Delta F_{\mathrm{RP}}(\tau) = \frac{4\pi\hbar}{\lambda}\Delta\hat{n}(\tau) \tag{2.38}$$

where $\Delta\hat{n}$ is provided in equation 2.33. Converting again to the frequency domain, one arrives at

$$\Delta F_{\mathrm{RP}}(f) = \sqrt{\frac{2\pi\hbar P_{\mathrm{in}}}{c\lambda}} \tag{2.39}$$

The conversion to displacement noise occurs by dividing equation 2.39 by the mechanical susceptibility χ_m

$$\Delta x_{\mathrm{RP}}(f) = \frac{\Delta F_{\mathrm{RP}}(f)}{\chi_m(f)} \tag{2.40}$$

For a simple spring-mass system of mass m in the free mass limit, $\chi_m(\omega) = m(2\pi f)^2$ and the displacement noise due to quantum radiation pressure can be written as

$$\Delta x_{\mathrm{RP}}(f) = \frac{1}{2\pi m f^2}\sqrt{\frac{\hbar P_{\mathrm{in}}}{2\pi c\lambda}} \tag{2.41}$$

and it is noted that the radiation pressure displacement noise scales as $P^{\frac{1}{2}}$. This is discussed in more detail in the next section. For a optical Fabry-Perot cavity of finesse $\mathcal{F}$, one needs to take into account the cavity enhancement factor $\frac{\mathcal{F}}{\pi}$ and the radiation pressure noise contribution becomes

$$\Delta x_{\mathrm{RP}}^{(\mathrm{FP})}(f) = \frac{1}{\chi_m(\omega)}\sqrt{\frac{2\hbar P_C\mathcal{F}}{c\lambda}} \tag{2.42}$$

where P_C refers to the power being reflected off the mechanical oscillator. Note that for a cavity on resonance, P_C is proportional to the cavity finesse $\mathcal{F}$ for a given cavity input power meaning that, in that case, $\Delta x_{\mathrm{RP}}^{(\mathrm{FP})} \propto \mathcal{F}$. This subtle fact really states that the signal to quantum noise for the light circulating inside the cavity must be the same as light outside the cavity, as both the coherent amplitude and the quantum fluctuations are enhanced. Radiation pressure noise has not yet been observed in a broadband optomechanical experiment utilizing movable mirrors.

2.3 The standard quantum limit

From the previous subsections, it can be seen that the shot noise contribution to total noise scales as $\frac{1}{\sqrt{P}}$ and the radiation pressure portion scales as $\sqrt{P}$. Therefore, as shown in figure 2.5, there exists a power P_{SQL} at which these two contributions to the total displacement noise are equal. When the imprecision due to shot noise is equal to the imprecision due to radiation pressure, this is known as the standard quantum limit (SQL) of a broadband displacement measurement.

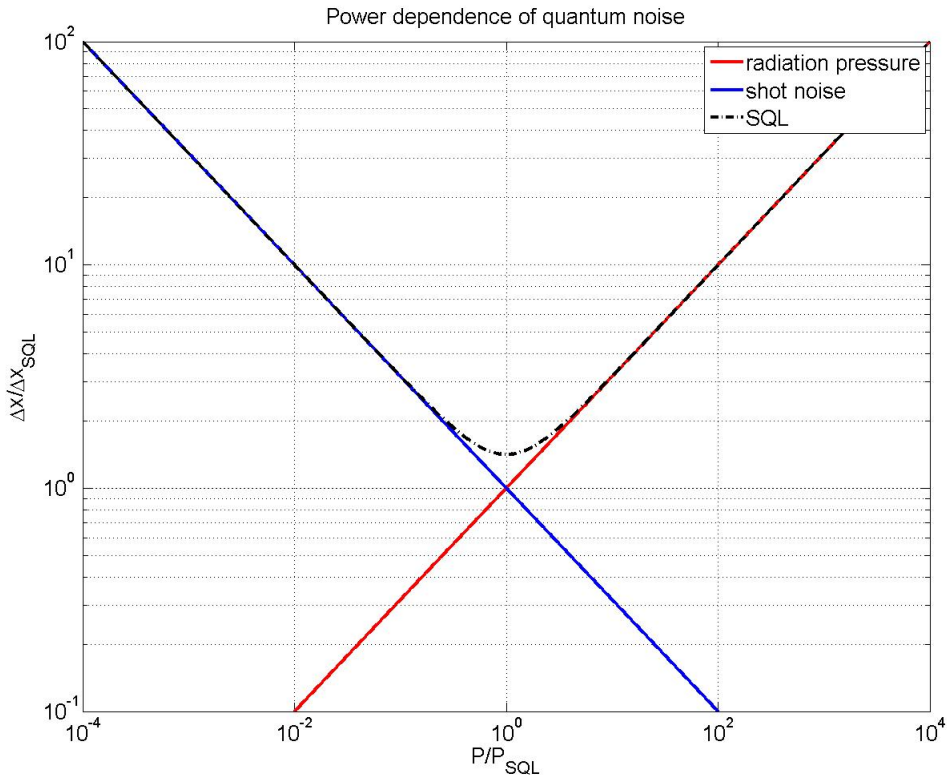

Figure 2.5: The power dependence of quantum noise, indicating a point of minimum total displacement known as the SQL. Discussed further in the text.

For interferometers like LIGO [39], by summing the radiation pressure and shot noise contributions, and minimizing the sum with respect to power, one arrives at

$$\Delta x_{SQL}(\omega) = \sqrt{\frac{4\hbar}{m\omega^2}} \tag{2.43}$$

at a specific power P_{SQL} given by

$$P_{SQL} = \frac{mc\lambda\omega^2}{4\pi} \tag{2.44}$$

In broadband optomechanical displacement measurements, the SQL has not yet been observed. However, certain narrowband on-resonance experiments, have been shown to reach the quantum ground state of oscillator motion [40, 41]. The ground state motion corresponds to the on-resonance form of the general definition of the SQL provided above.

2.4 On-resonance versus off-resonant displacement measurement

For the sole purpose of observation of quantum displacement noise, the question is often asked if there is a benefit to measuring the motion of a low-frequency oscillator with a detection band above the mechanical resonance frequency ($\omega \gg \omega_m^{(\mathrm{Low})}$) or observing a high-frequency oscillator at a measurement frequency equal to the mechanical resonance frequency ($\omega = \omega_m^{(\mathrm{High})}$). The goal of investigating the quantum-limited performance of Advanced LIGO drives the desire to utilise these low frequency mechanical oscillators in the free-mass regime.

However, above an oscillator's resonance frequency, the thermal contribution to oscillator position falls off and the ratio of quantum noise to thermal noise becomes more favorable. In fact, it can be shown [42] that the ratio of quantum to thermal noise is

$$\frac{S_{\mathrm{SQL}}(\omega)}{S_{\mathrm{thermal}}(\omega)} = \frac{\hbar\omega_m}{2k_BT}\frac{\chi(\omega_m)}{\chi(\omega)} \tag{2.45}$$

where $\chi(\omega)$ is the mechanical susceptibility and a detection efficiency of 1 is assumed. Equation 2.45 reduces to the on-resonance case in the limit $\omega \to \omega_m$, but for an off-resonance displacement measurement it shows that one can be SQL-limited even when the mechanical mode possesses more than the ground state energy.

Through the suitable choice of χ, it is clearly possible to measure quantum noise with a signal-to-background even greater than unity. In addition to the boost of quantum noise by this off-resonance factor $\frac{\chi(\omega_m)}{\chi(\omega)}$, operating with a detection frequency away from mechanical resonance also allows direct determination of the damping properties and loss mechanisms of any particular mechanical resonance of the oscillator. Such information can be garnered from the frequency dependence of the off-resonant thermal displacement noise [35] and can then be used in further optimization of shape or composite materials of the mechanical device.

Though such information can be gathered from LIGO-like measurements of low-frequency oscillators, it should be mentioned that several high-frequency oscillators have already been demonstrated in the quantum regime. The motion of those oscillators is quantum-limited, in a very narrow frequency band.

Chapter 3

$Al_xGa_{1-x}As$ mechanical oscillators in an optical cavity

The use of oscillators in the free mass regime for broadband displacement measurement has been motivated in previous chapters. Here the specifics of the chosen oscillators are detailed, including both fabrication and use in an optical cavity. The pertinent optical and mechanical properties are also specified, and measurements are compared to a finite element model, showing good agreement.

3.1 Introduction

The quest to observe optical quantum noise in the broadband displacement spectrum of a free mass has many challenges and requirements, but these can be subdivided into two main categories. Firstly, a suitable oscillator must be designed. Its suitability relies on the expected ratio of the quantum to thermal displacement noise contributions (see chapter 2 for discussions of these noise sources). Having this ratio as high as possible improves the chances of observing quantum contributions to a noise spectrum. Essentially, this requirement encourages the use of very low mass oscillators with very little motional damping (see equations 2.9 and 2.41). Secondly, the motion of this oscillator must be measured with very high precision. This criterion may initially be seen as a requirement for the readout system but, for the method of motional detection presented in this thesis, it also places a requirement on the test mass - one must be able to reflect light off the device without substantial optical losses in order to use it in a sensitive optical cavity (similar to one arm of a LIGO interferometer). Several methods for ensuring this high reflectivity have been investigated by the field. For instance, the attachment of small scale mirrors to AFM cantilevers has been investigated by the Bouwmeester Group [43, 44]. In this thesis however, a different method is advocated - the mechanical oscillators themselves are monolithically fashioned from a reflective material wafer, similar to [45, 46, 47, 48].

As will be discussed more in this chapter, the oscillators are fabricated from an aluminium gallium arsenide (AlGaAS) wafer. The geometry of the chosen structures can be quite varied, but is generally categorized as a cantilever - that is, a singly-bound harmonic oscillator - as this shape provides the most compliance and lowest mass. Modeling the system using finite element analysis allows one to choose the shape which optimizes performance by being both compliant and light. As the entire structure was cut from a single crystalline wafer, very high mechanical quality factors are possible. As a consequence, the thermal noise is comparatively less than that for similar designs made from amorphous materials or non-monolithic designs involving adhesive connections of different substructures.

3.2 Oscillator design fundamentals

In order to observe quantum radiation pressure in the off-resonant displacement spectrum of a mechanical oscillator, there exists several design criteria. Additionally, ease of transport, installation and use places additional requirements on the fragility, yield and survivability of the devices. The shape, materials, modeling and fabrication are all derived from these goals, and the success of experiments of this type are heavily based on the realization of the right oscillator.

Figures 3.1 and 3.2 show the design of two oscillator arrays fabricated and used in this experiment. These oscillators are etched from a single monocrystalline wafer consisting of alternating layers of $Al_{0.12}Ga_{0.88}As$ and $Al_{0.92}Ga_{0.08}As$, which combine to form a Bragg reflector (see subsection 3.2.2 for discussion). Throughout this chapter, the perimeter of the AlGaAs chip (which surrounds the oscillator array) will be referred to as the chip-edge, and acts as a fixed immovable mirror for testing and characterization purposes.

3.2.1 Modal masses and susceptibility

As shown in the analysis presented in section 2.1.3, the effective mass of the mechanical modes of the oscillator are very important to the thermal noise spectrum. Smaller masses are more susceptible to large thermal motion as $x_{\mathrm{th}} \sim \frac{1}{\sqrt{m}}$. Additionally, the analysis of quantum noise in section 2.2.3 shows that lighter masses are more affected by the radiation pressure push $x_{\mathrm{RP}} \sim \frac{1}{m}$. Given these general dependencies on the masses, it becomes clear that making the oscillator lighter shows a weak benefit as $\frac{x_{\mathrm{RP}}}{x_{\mathrm{th}}} \sim \sqrt{m}$. This low mass oscillator is most readily accomplished in a cantilever-style, where the support structure is designed to be as small as possible.

The second consideration is the mechanical susceptibility of the oscillator. Operating in the free-mass regime of the oscillator spectrum has been advocated in chapter 2. However, as calculated in equation 2.18, all physically realizable oscillators possess many modes of motion and the corresponding thermal noise from those modes. If motion is measured in only one direction, some of these motional modes will occur in a plane perpendicular to the direction of interest, and will contribute minimal thermal noise - one can think of these

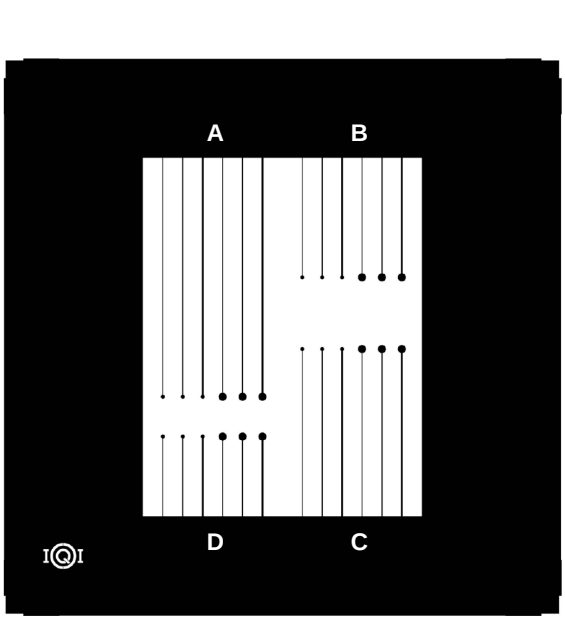

A-cantis, 3 mm long, left to right
1) width: 5 um, pad diam: 50 um
2) width: 10 um, pad diam: 50 um
3) width: 20 um, pad diam: 50 um
4) width: 5 um, pad diam: 100 um
5) width: 10 um, pad diam: 100 um
6) width: 20 um, pad diam: 100 um

B-cantis, 1.5 mm long, left to right
1) width: 5 um, pad diam: 50 um
2) width: 10 um, pad diam: 50 um
3) width: 20 um, pad diam: 50 um
4) width: 5 um, pad diam: 100 um
5) width: 10 um, pad diam: 100 um
6) width: 20 um, pad diam: 100 um

C-cantis, 2 mm long, left to right
1) width: 5 um, pad diam: 50 um
2) width: 10 um, pad diam: 50 um
3) width: 20 um, pad diam: 50 um
4) width: 5 um, pad diam: 100 um
5) width: 10 um, pad diam: 100 um
6) width: 20 um, pad diam: 100 um

D-cantis, 1 mm long, left to right
1) width: 5 um, pad diam: 50 um
2) width: 10 um, pad diam: 50 um
3) width: 20 um, pad diam: 50 um
4) width: 5 um, pad diam: 100 um
5) width: 10 um, pad diam: 100 um
6) width: 20 um, pad diam: 100 um

Figure 3.1: First generation chips, which suffered from poor yield and breakage during shipping.

types of non-coupling modes as having a very large modal mass. Nevertheless, in the direction of interest, there will inevitably be modal motion occuring in addition to that of the fundamental mode. A suitable design will engineer those modes to occur at large frequency intervals, so that a measurement of quantum noise can be made at a frequency between them. This engineering design criterion also motivates the choice of a singly-bound cantilever structure.

3.2.2 Reflectivity

For measurements made on resonance of the optical cavity, intracavity power is enhanced by of order $\frac{\mathcal{F}}{\pi}$, where $\mathcal{F}$ is the cavity finesse. However, the signal-to-quantum-noise of the light must remain fixed, so the measured rms mirror motion due to shot noise must scale as $\frac{1}{\mathcal{F}}$, and that due to quantum backaction must scale as F. Usually, it is possible to obtain $\frac{1}{2}$-inch mirrors with very low losses, so that the cavity finesse is governed primarily by the optical loss of the other mirror - in this case, a micro-cantilever oscillator.

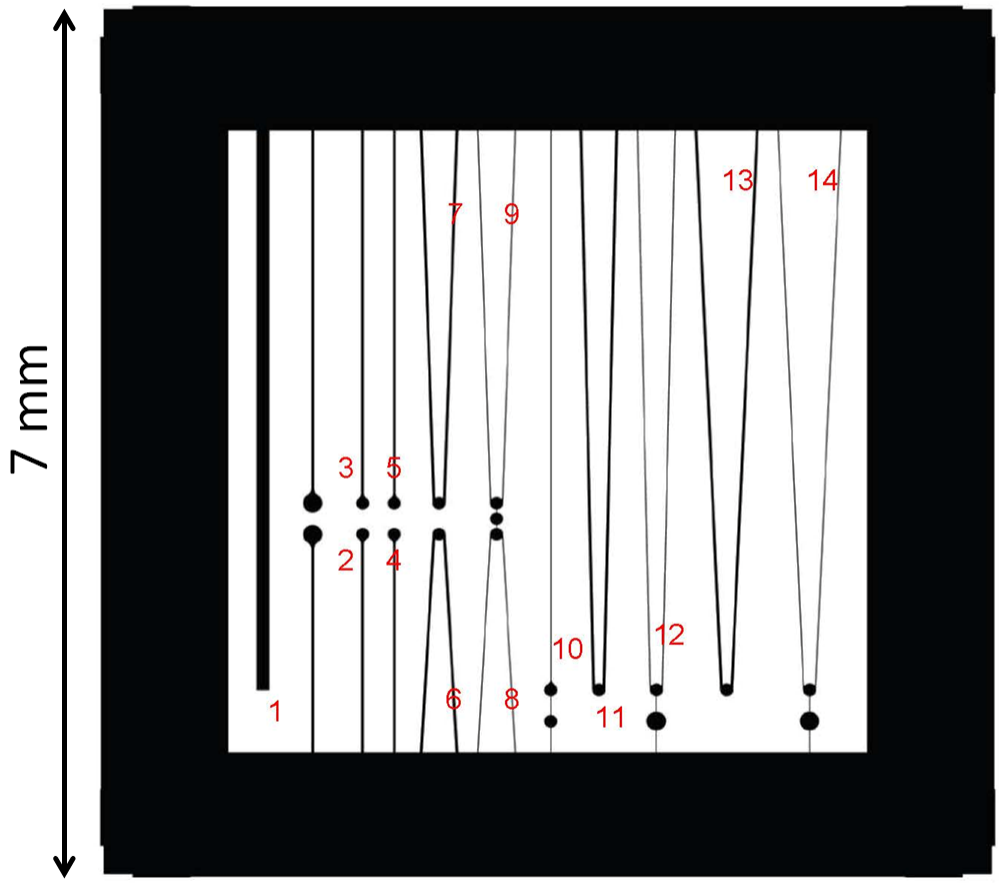

Figure 3.2: Second mask layout with the various oscillator geometries numbered. Majority of measurements in this thesis are performed on device 7. Note the presence of sacrificial pads, teardrop-shaped mirror pads and dual support geometries. All mirror pads are 100μm in diameter, except those of devices 2 and 3 and the sacrificial pads of devices 12 and 14, all of which are 200μm across. Image credit to Garrett Cole.

In this case, the oscillators are constructed from a wafer of a distributed Bragg reflector, consisting of an alternating sequence of high and low index layers. Here the high index layers are $Al_{0.12}Ga_{0.88}As$ and the low index layers are $Al_{0.92}Ga_{0.08}As$. The principle of a Bragg reflector is simple: at each interface between

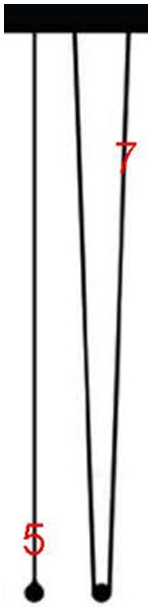

Figure 3.3: An enlarged version of device 7, alongside device 5 for comparison. Of the devices in the second mask layout, these two offer the most promise for observation of quantum effects due primarily to a limit in the cryogenic actuation range of the cavity piezo.

high and low index layers, a Fresnel reflection occurs. If the spacing between the layers is suitably chosen, the reflection components from all the interfaces will interfere constructively thereby constituting a highly reflective structure. The reflectivity is determined primarily by the ratio of the index of refraction for the two materials, and by the number of interfaces where Fresnel reflection occurs. For the oscillators in this experiment, 40 periods of high and low index layers are necessary due to the index contrast between the $Al_{0.12}Ga_{0.88}As$ and $Al_{0.92}Ga_{0.08}As$ layers. This large number of interfaces allowed a measured reflectivity of approximately 99.982%.

The measurement of the distributed Bragg reflectivity was performed by measuring the finesse of a cavity formed by the chip and separate well-characterized mirror. figure 3.4 shows a measurement of the cavity pole of the optical Fabry-Perot on the chip-edge, where the compliance of the structure is negligible and therefore dynamical or ponderomotive effects are insignificant. Given that the large input coupler has

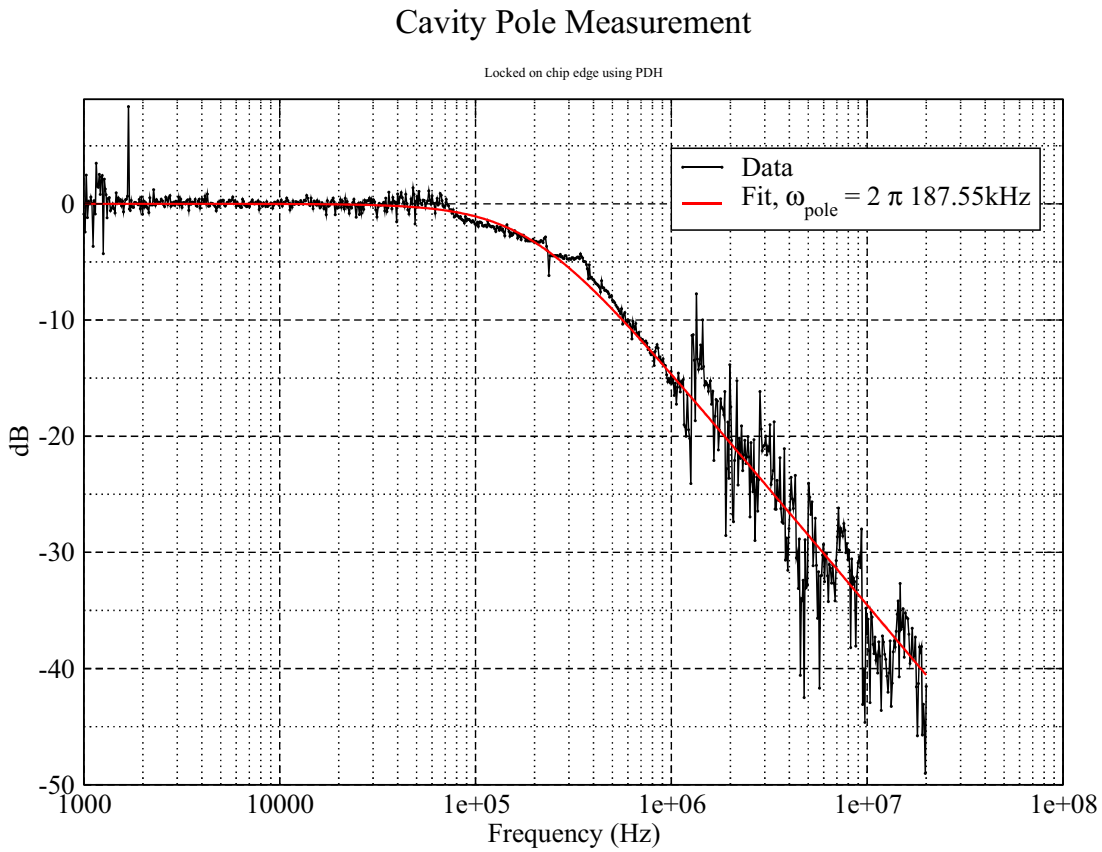

Figure 3.4: Cavity pole as measured using reflection PDH on the chip-edge. From this measurement, one can extract the materials-limited reflectivity of the chip to be 0.99982.

been externally measured and calibrated, we can infer from that measurement the stated material-limited reflectivity of 0.99982. A cavity finesses of 2.3×10^4 has been demonstrated for our oscillators and a superpolished, supercoated mirror. Additionally, the reflectivity curve of the oscillators is also designed to peak at approximately 1.078μm at room temperature, so that at 5K the maximum reflectivity is obtained at 1.064μm.

3.2.3 Mirror pad size

The mirror pad size is now considered, as it contributes a large fraction of the mass of the oscillators (shown in figures 3.1 and 3.2 and 3.3) and also the plays a role in the fraction of light reflected. The diameter

of the mirror pad on the cantilever is set by two competing considerations. Firstly, as motivated in subsection 3.2.1, the oscillator mass should be as low as possible - leading to the desire to make smaller mirror pads. Secondly, the avoidance of diffraction losses and ease of beam alignment would contrastingly promote larger mirror pads. Figure 3.5 illustrates a cavity with significant diffraction losses, where the beam spot size is

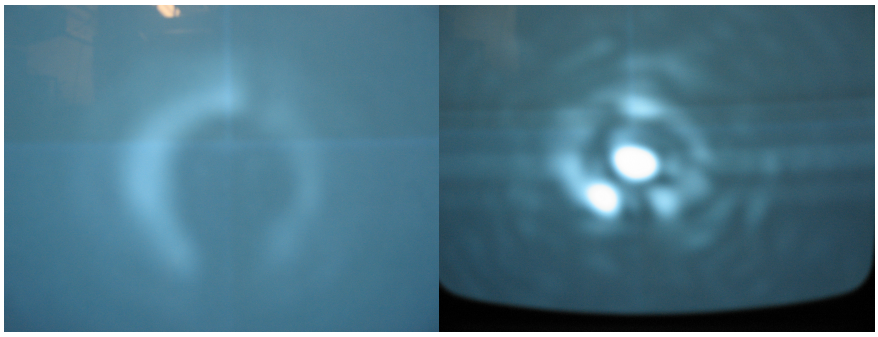

Figure 3.5: CCD image of the cantilever cavity transmission unlocked (left) and locked (right): The cavity length was adjusted to produce a spot size that was comparable to the 50μm cantilever head. Diffraction losses around the edges of the micromirror limited the cavity finesse to approximately 2000. The outline of the cantilever can be seen in the left image.

comparable to the 50 μm pad diameter (note: this prompted an increase in the size of the pads to 100 μm to avoid such losses). Experimentally, oscillator pad size and cavity parameters must be both be chosen so that diffraction losses around the edges of the micromirror do not substantially degrade the cavity finesse. A rough estimate of the role of mirror pad size can be found from the fractional power D going around the edges of the cantilever pad of radius a

$$D = 1 - \frac{2}{\pi w^2}\int_0^a 2\pi r \exp\left(\frac{-2a^2}{w^2}\right) \mathrm{dr} = \exp\left(\frac{-2a^2}{w^2}\right) \tag{3.1}$$

where w is the spot size of a centered gaussian beam on the circular mirror pad. This formula is an approximation, and more detailed calculations can be found in [49].

If one chooses to limit optical diffraction losses to less than $1-R$ where R is the cantilever reflectivity given in subsection 3.2.2, then this criterion constrains the beam size. For a plano-concave optical cavity, the spot size w of the lowest order optical mode on the flat mirror is given by [50, 51]

$$w^2(g) = \frac{L\lambda}{\pi}\sqrt{\frac{g}{1-g}} \tag{3.2}$$

where $g = 1 - \frac{L}{R}$, L is the cavity length and R is the radius of curvature of the curved mirror. The cavity

is only a stable resonator if $0 \leq g \leq 1$ and so as $L \rightarrow R$ the spot size becomes smaller and diffraction losses are lessened. This simple estimate leads to the rule of thumb for the cavity length with a 100 μm diameter cantilever pad: the length of the cavity must be within about 200um of the input coupler radius of curvature (1cm) otherwise diffraction losses imply that the optical performance would be limited by the choice of cavity parameters as opposed to the intrinsic chip properties.

It should also be noted here that figure 3.5 also illustrates another side effect of diffraction losses. Sharp edges and apertures, particularly circular ones, produce diffraction effects which significantly distort the intensity profile of the beam. This distortion occurs in both the near-field (Fresnel) and far-field (Fraunhofer) regimes [50] and, when the effect is large, ultimately leads to a break-down of the concept of orthogonal optical cavity modes.

3.2.4 Mechanical loss and quality factor considerations

One major obstacle when approaching the SQL, or the backaction-dominated regime, is the random Brownian motion of the oscillator. However, above an oscillator's resonance frequency, the thermal contribution to oscillator position falls off and the ratio of quantum noise to thermal noise becomes more favorable [42]. In an experimental setting however, the oscillator often has other higher order mechanical modes which couple thermal noise into the measurement band. When measurements are made between mechanical resonances, the loss angle attributed to higher order mechanical modes must be sufficiently small so as to contribute as little thermal noise as possible.

The monocrystalline AlGaAs mechanical oscillators have been found to have very high Q_m - ranging from approximately 30000 at room temperature to more than 100000 at 10 K. Additionally, the Q_m of the higher order mechanical modes have been found to be equivalent to that of the lowest mechanical mode. The uniformity of Q_m versus frequency suggests that structural damping is the dominant form of mechanical energy loss (see section 2.1.4). The temperature dependence of the mechanical loss has been measured for several devices. This temperature dependence has been found to be strongly dependent on exact device used and several other factors, most notably, the sharpness of the defined etch. Figure 3.6 presents the measured temperature dependence of a few generations of devices.

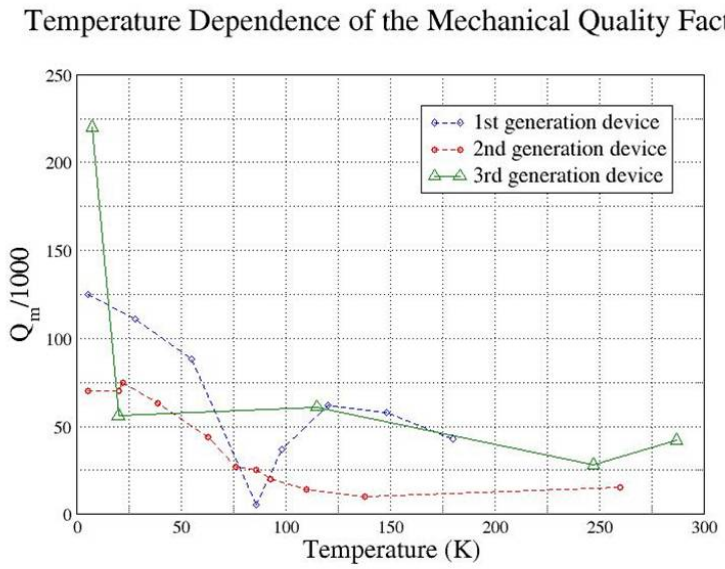

Figure 3.6: Temperature dependence of the mechanical quality factor of several oscillators used in this experiment. 1st generation devices are made in the geometry of figure 3.1, 2nd and 3rd generation devices are made in the geometry of figure 3.2. The increase in Q_m is theorized to come from sharper etches due to refinement of the fabrication process.

3.2.5 Power Handling Capability

Quantum radiation pressure noise scales as $\sqrt{P}$, where P is the intracavity circulating power. The ability to increase the circulating optical power is limited by the power handling capability of the AlGaAs oscillators. Beyond this threshold, increasing the power begins to damage the device and leads to reduced reflectivity and ultimately oscillator breakage. For the presently available devices, this power thresehold usually occurs between 100 mW and 200 mW, dependent on the particular oscillator. There are several theories why this breakage threshold exists, based on a few intentional observations of device breakage. Firstly, most of the devices were observed to break at the juncture between the mirror pad and the support

structure. It was theorized that the absorption loss of the oscillator leads to thermal gradients, which cause breakage via differential expansion and thermally-induced stress should the gradients become to large. This idea lead to the introduction of rounded edges and teardrop-shaped mirror pads, and the changes seemed to result in an increased breakage threshold. Future improvements of material purity and lowered absorption losses are expected to further improve the oscillator power handling performance. Additionally, suitable device shape plays a strong role in avoiding large thermal gradients and thermally-induced stress.

3.2.6 Device Yield and Chip Fragility

As shown in section 3.2, the initial design for the cantilever array was a very canonical one - utilizing straight single supports. However, after fabrication, transportation and installation, it was found that many of the devices had broken or become physically entangled with neighboring devices. Therefore the dual-support oscillators, which stiffen the in-plane mode while minimally affecting the out-of-plane mode, were introduced into the second design. Device yield improved significantly.

Additionally, as seen in figure 3.2, several cantilevers are doubly-bound, with extra mirror pads. These pads and extra supports serve the purpose of allowing a highly robust device for the final fabrication steps and for transatlantic shipping from the manufacturing point in Vienna, Austria to the laboratory in Cambridge, Massachusetts. They are referred to as sacrificial pads and supports and, as the name implies, are removed in the laboratory. The method of removal of these pads is fairly simple. Using excessive laser power on the sacrificial pad, the device breakage threshold (of approximately 150mW) is exceeded. A special high-power fiber coupled beam is utilized in this process, because there is often insufficient power in the main beamline to destroy the cantilever, neglecting cavity enhancement (See section §4.1). Upon release, the CCD image often shows the cantilever moving by several hundred microns in-plane, and presumably the amplitude in the longitudinal direction is even larger. The optical quality of the non-sacrificial mirror pad appears to be unaffected in both cases. It has also been found that this method did not affect the reflectivity of nearby pads. The quality factor of a device that was freed from its sacrificial pad was found to be approximately a factor of 2 lower than the quality factors of the doubly-supported devices. Although the removal of the sacrificial pad appears on the CCD image to be a fairly violent process, it is presently unclear whether this

factor of 2 is due to that process or other factors such as differences in shape or surface-to-volume ratio.

3.3 Fabrication of the $Al_xGa_{1-x}As$ cantilevers

The fabrication of the mechanical oscillators was performed at Universität Wien by Dr. Garrett Cole, and we have relied heavily on his expertise in the microfabrication field. In this section, an outline of the procedure used by Dr. Cole to produce the devices is documented. More about these devices can be found in published articles [47, 45, 48]. The process was developed initially for use in the megahertz oscillators used in ground state cooling experiments in the group of Prof. Markus Aspelmeyer, and modified to allow the highly compliant devices used in this experiment. Fabrication of the mechanical oscillators is based upon a dual-sided bulk micromachining process of pre-grown dielectric multilayers. It is important to note that these resonators are sculpted directly from the multilayer mirror and are ideally equally reflective at all points along the structure.

The process begins with lithographic patterning of the resonator geometry, which defines the shape of the oscillators. This step is then followed by a 7 μm deep high-density plasma etch through the thickness of the multilayer, utilizing real-time monitoring of the etch depth via a laser interferometer. After defining the cantilever array, the substrate is lapped to a thickness of approximately 150 μm and subsequently polished to enable backside lithography. After a thorough clean, a SiN_x hard mask is deposited on the backside of the sample via plasma-enhanced chemical vapor deposition and the chip is bonded face-down with high-temperature wax to a transparent handle. Following an aligned backside lithography step, a SF_6-based reactive ion etching process is used to define a window that allows access to light transmitted through the device. Without this step, the oscillators remain above an optically lossy surface. With the hard mask defined, the GaAs substrate is removed with a selective wet-chemical etch that terminates on the high aluminum content AlGaAs etch-stop layer, which is subsequently removed in dilute HF. With the backside window now open, the sample is demounted by dissolving the wax bonding layer in acetone. Finally, a critical point drying process is used to avoid collapse or damage of the highly compliant devices. Figure 3.7 illustrates the steps utilized in the production of the devices.

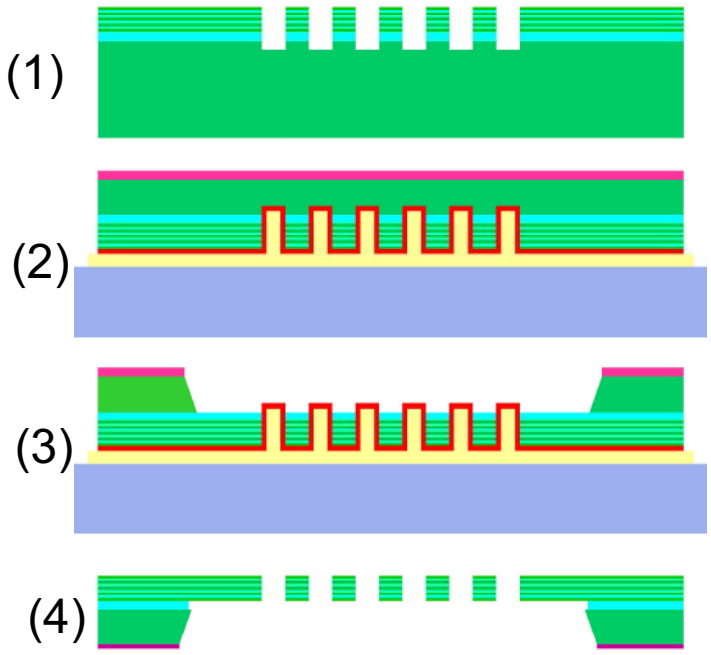

Figure 3.7: Process flow for the production of the mechanical devices as performed by Garrett Cole. This process relies on a dual-sided bulk micromachining procedure with major steps (as outlined in the text) including (1) Definition of the resonator geometry in the epi-structure. (2) Substrate thinning and repolish, followed by hard mask deposition and wax bonding to a temporary glass handle. (3) Backside window definition and GaAs substrate back-etch. (4) Etch stop removal in dilute HF, sample demount, and critical point drying to avoid cantilever collapse. This figure was provided by Garrett Cole.

3.4 Finite element modeling of the oscillator thermal noise

This section presents the documentation of an analysis and prediction of oscillator thermal noise using a finite element model (FEM). After trying common FEM computer programs, most notably ANSYS, it was found that COMSOL was easiest to interface and use for the purposes of modeling the mechanical cantilevers utilized in this experiment. This choise mimics the experience of many other research groups in the optomechanical field. The COMSOL-based model was found to be in close agreement with the

measurements. Figure 3.8 shows a particular group of bending modes for device 7.

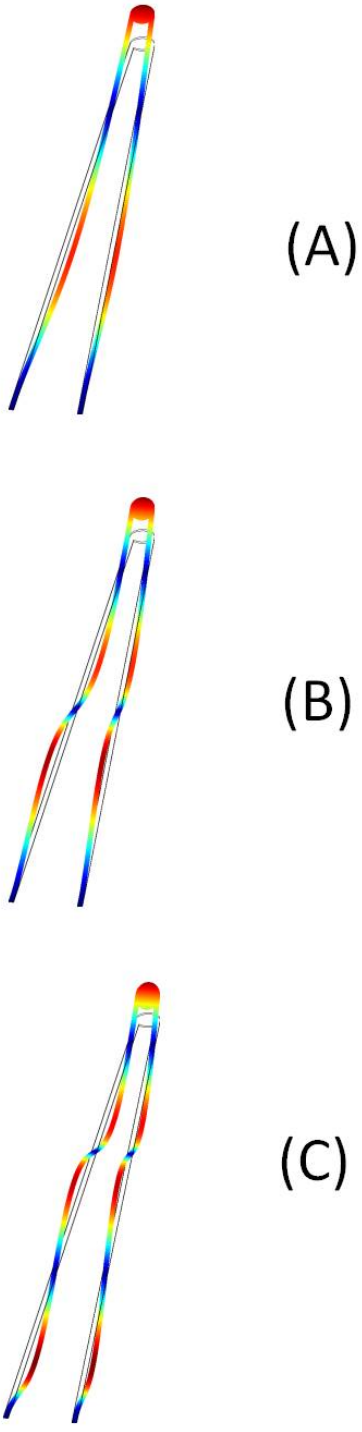

Figure 3.8: Mode shapes predicted by the finite element model for device 7 showing mechanical modes at (A) 3.5 kHz, (B) 10kHz and (C) 20kHz. The colors indicate displacement from the equilibrium rest position with large displacements shown in red and small displacements in blue. These are the dominant longitudinal modes for this device and show up prominently in thermal noise limited spectra.

3.4.1 The Method behind the model

There are two methods by which a thermal noise prediction of a mechanical device might be obtained. Firstly, if one possesses knowledge of the frequency dependence of the loss angle, and the spatial distribution of mechanical losses along the device, one can directly calculate [52] the thermal displacement spectrum from those two pieces of information. However it is not common to possess such information for a particular device, and expanding the model to be applicable to devices of different geometry may be problematic since such information can be largely device-specific. Nevertheless, this method has the advantage of being able to directly predict interference-type effects, which may lower or boost, the thermal noise between mechanical resonances for devices possessing localized regions of high mechanical loss.

The second method by which oscillator thermal noise may be predicted, and the one favored in this experiment, involves the direct calculation of the thermal noise from each individual mechanical mode and summing all the contributions. For this method to work, one needs to know the resonant frequencies and the effective modal masses for each resonance (see analysis in subsection 2.1.3). Additionally, the mechanical quality factor Q_m of each mode needs to be known. Experimental measurements, via time-domain ringdown, of the Q_m of individual modes yields the same number. This result is true for all the device shapes measured, and perhaps indicates that the mechanical loss is uniformly distributed over the device. The uniformity of the Q_m for all mechanical modes makes the calculation of thermal noise by summation the logical choice as a method for the prediction of the thermal spectrum.

Explicitly, from the analysis of subsection 2.1.3, the thermal motion of the device is calculated as

$$x^2_{\text{RMS, therm}} = \sum_{n=1}^{\infty} \frac{4k_{\text{B}}T\phi_n\omega_n^2}{m_n\omega} \frac{1}{(\omega^2-\omega_n^2)^2+(\phi_n\omega_n^2)^2} \tag{3.3}$$

where m_n and ω_n are the FEM-derived modal masses and frequencies respectively, and $\phi_n = \frac{1}{Q_m}$ for all n (velocity-independent, structural damping). In practice, the sum can be truncated to only include a finite number of mechanical modes and still reliably predict the measured thermal noise spectrum in the low frequency measurement band. Equation 3.3 ignores the constructive or destructive interference of thermal noise found in oscillators where there are localised regions of higher than average mechanical loss. Appendix

B contains a table of the lowest frequency mechanical modes for device 7, and their corresponding mechanical modal masses. The FEM is sensitive to motion of a specified point at the center of the mirror pad. Therefore, large modal masses correspond to motion which is in the plane of the reflective surface and does not couple strongly to the optical cavity. Additionally, modeling utilizing a gaussian-weighted sampling of points across the mirror pad has been implemented. This route was taken in an effort to further increase the accuracy of the FEM by more closely mimicing the gaussian optical beam.

3.4.2 Thermal noise spectra from the finite element model

Using equation 3.3 and the list of modal masses and resonant frequencies (such as those presented in Appendix B), one can produce a prediction of the thermal noise spectrum of the oscillator. If motion is sensed in only one direction, the mechanical modes which couple to that direction will be most prominent. Equivalently, these modes will possess the lowest modal mass and therefore the largest motional amplitude. In figure 3.9, the largest motion occurs at 3.5 kHz, 10 kHz and 20 kHz. These peaks correspond to the motion shown in figure 3.8 (A), (B) and (C) respectively - perpendicular to the plane of the reflective mirror pad.

3.5 Use of these oscillators in an optical cavity

In section 2.1, it was shown that a highly-compliant mechanical oscillator can be utilized as a free mass. This method is used in LIGO to suspend reflective optics, which serve as the test masses for gravitational wave sensing. However, as stated in section 1.3, optical gravitational wave interferometers also utilize Fabry-Perot arm cavities as a method for boosting the interferometer response to a given length change - in effect creating a more sensitive detector. The use of the movable mirrors in an optical cavity configuration alters the steady-state response of the interferometer to changes in the optical fields.

3.6 The optical spring

The main effect of the use of a highly-compliant and deformable optical cavity is the optical spring. This effect can be qualitatively understood by considering a detuned deformable optical cavity. If the length

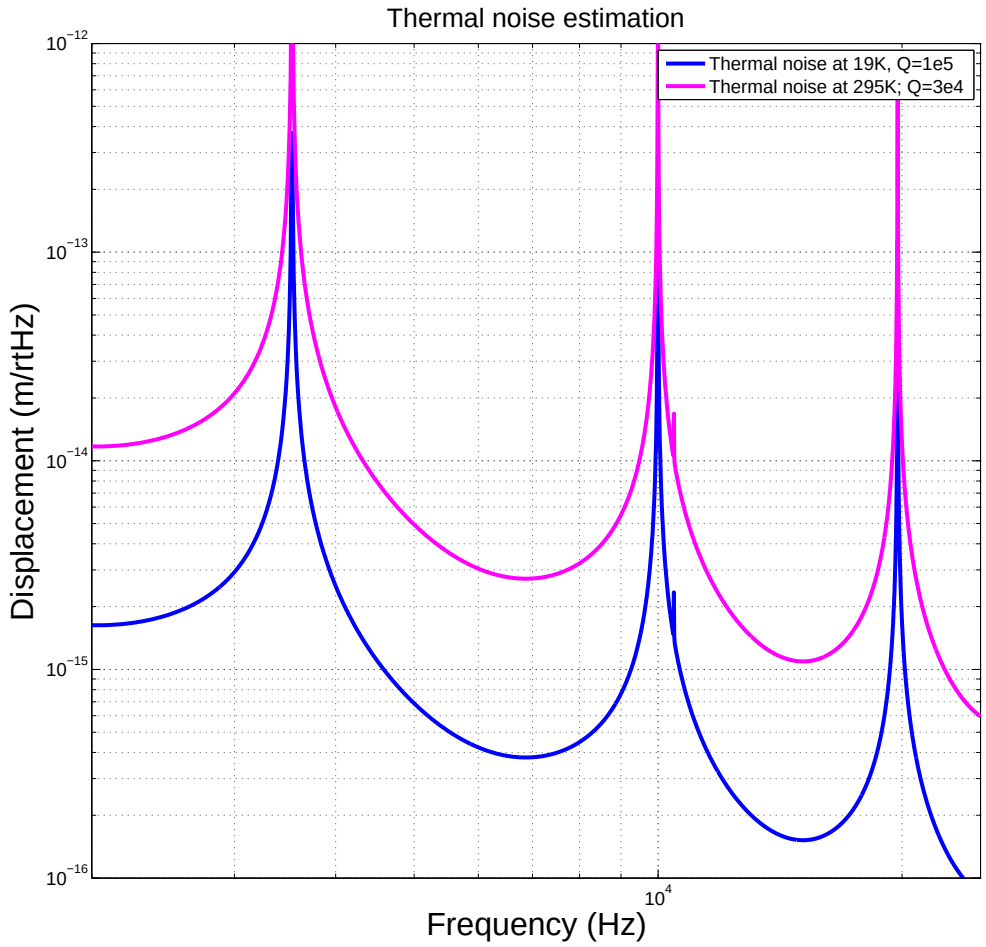

Figure 3.9: Thermal noise prediction for device 7, utilizing the results of the finite element model and measured numerical values for the mechanical quality factor. The spectra predicted for both room temperature and cryogenic measurements are presented. The three most prominent peaks, at 3.5 kHz, 10 kHz and 20 kHz, correspond to the three motional modes shown in figure 3.8 (A), (B) and (C) respectively.

of this detuned cavity is altered, the intracavity circulating power P_c changes and that, in turn, changes the radiation pressure force on the mirrors (see equation 2.37). As the cavity end mirrors are movable, this change in radiation pressure results in a displacement. Alternatively, it should be noted that this cycle can be considered in terms of an initial change in the input fields (either frequency or amplitude).

Mathematically, the steady-state intracavity power as a function of a displacement change x is

$$P_c(x) = \frac{\gamma^2 P_c^{\max}}{\gamma^2 + \left[\delta + \frac{x}{L}\omega_0\right]^2} \tag{3.4}$$

where δ is the cavity detuning, L is the cavity length and γ defines the spectral width of the resonance. $P_c^{\max}$ is the maximum circulating power, which occurs when the cavity is undetuned ($\delta = 0$) and at the unperturbed equilibrium point ($x = 0$).

Using equation 3.4, one can write the force on an end mirror of the cavity as $F(x) = \frac{2P_c(x)}{c}$. An equivalent spring constant is then defined as $k = -\frac{dF}{dx}$. This spring constant, written in the frequency domain, is given by [cite buonanno and chen, 2003, Advanced Gravitational Wave Detectors book]:

$$k_{\rm opt}(\omega) = -\frac{2P_c\omega_0}{cL}\frac{\delta}{(\omega - \delta + i\gamma)(\omega + \delta + i\gamma)} \tag{3.5}$$

From the above equation, it is clear that the spring constant k has both real and imaginary parts. Physically, the imaginary part is a damping term. This damping comes from the fact that the response of the cavity is delayed by the intracavity buildup time. In the limit $\frac{\omega}{\delta} \ll 1$, equation 3.5 can be expanded as a Taylor series [53, 54], giving:

$$k_{\rm opt}(\omega) = \frac{2P_c\omega_0}{cL}\frac{\delta}{\gamma^2 + \delta^2}\left[1 + \frac{2i\gamma\omega}{(\gamma^2 + \delta^2)} + \ldots\right] \tag{3.6}$$

The real part of the above equation gives a real optical force, in analogy with an ideal spring obeying Hooke's Law. The second term is imaginary and emerges from the non-zero cavity buildup time giving a delayed cavity response to any excitation. The total spring constant is the sum of the mechanical and optical components

$$k_{\rm tot} = k_{\rm m} + k_{\rm opt} \tag{3.7}$$

Interestingly, the optical spring is characterised by either anti-damping and a restoring force, or damping and an anti-restoring force [55, 54]. For this reason, a single optical spring is not itself a stable entity. Control systems must provide additional feedback to compensate, or two optical springs may be used to obtain a stable system.

3.7 Cavity response transfer functions

Consider the optical cavity shown in figure 3.10. It is comprised of one fixed mirror and a mirror that is spring-bound and highly compliant (in the free mass limit). The input, output and circulating fields of

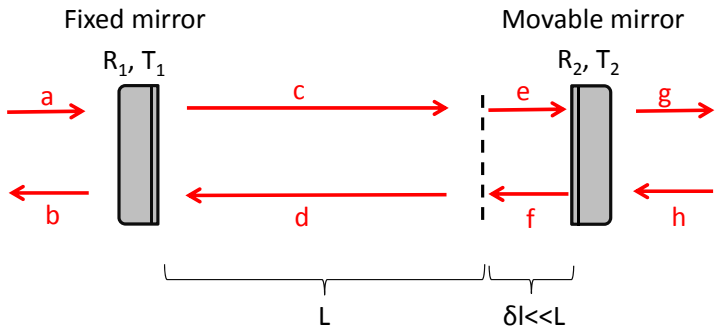

Figure 3.10: A detuned optical cavity, of nominal length L, showing fields a through h as discussed in text. A fixed mirror possess power reflection and transmission coefficients of R_1 and T_1 respectively, while those of the movable end mirror are denoted R_2 and T_2 respectively.

cavity are labeled in the diagram by letters $\boldsymbol{a}$ through $\boldsymbol{h}$. One can now write the relationship between these fields in terms of the power reflection and transmission coefficients of the mirrors, $R_{1,2}$ and $T_{1,2}$ respectively. First look at the DC carrier components of the fields,

$$\boldsymbol{b} = \sqrt{R_1}\boldsymbol{a} + \sqrt{T_1}\boldsymbol{d} \tag{3.8}$$

$$\boldsymbol{c} = \sqrt{T_1}\boldsymbol{a} - \sqrt{R_1}\boldsymbol{d} \tag{3.9}$$

$$\boldsymbol{d} = e^{i\omega_0 \frac{\delta l}{c}}\boldsymbol{f} \tag{3.10}$$

$$\boldsymbol{e} = e^{i\omega_0 \frac{\delta l}{c}}\boldsymbol{c} \tag{3.11}$$

$$\boldsymbol{f} = -\sqrt{R_2}\boldsymbol{e} + \sqrt{T_2}\boldsymbol{h} \tag{3.12}$$

$$\boldsymbol{g} = \sqrt{T_2}\boldsymbol{e} + \sqrt{R_2}\boldsymbol{h} \tag{3.13}$$

in addition to the trivial relations for the front and back input fields. These linear relations can be expressed in matrix form, and the matrix then inverted to find each field in terms of, say, the input field a. The

coefficient matrix is therefore an 8×8 matrix:

$$M_0 = \begin{pmatrix} M_{11} & \cdots & M_{18} \\ \vdots & \ddots & \vdots \\ M_{81} & \cdots & M_{88} \end{pmatrix} \tag{3.14}$$

where

$$M_{21} = \sqrt{R_1} \tag{3.15}$$

$$M_{24} = \sqrt{T_1} \tag{3.16}$$

$$M_{31} = \sqrt{T_1} \tag{3.17}$$

$$M_{34} = -\sqrt{R_1} \tag{3.18}$$

$$M_{46} = e^{i\omega_0 \frac{\delta l}{c}} \tag{3.19}$$

$$M_{53} = e^{i\omega_0 \frac{\delta l}{c}} \tag{3.20}$$

$$M_{65} = -\sqrt{R_2} \tag{3.21}$$

$$M_{68} = \sqrt{T_2} \tag{3.22}$$

$$M_{75} = \sqrt{T_2} \tag{3.23}$$

$$M_{78} = \sqrt{R_2} \tag{3.24}$$

$$M_{88} = 1 \tag{3.25}$$

and the other matrix elements are zero, except for the diagonal entries M_{11} to M_{77} which are all -1. Inverting this matrix, one can define the amplitude of the input field carrier at each point

$$P_n = \sqrt{P_{in}} N_{n1} \tag{3.26}$$

where P_{in} is the input power into the cavity and N is simply M^{-1}. From this carrier amplitude, the radiation pressure force acting on the mirrors can be calculated from the equations of section section 2.2.3, and a mechanical susceptibility χ derived from the finite element model and measured mechanical quality factors Q_m. However, the above calculation currently only holds true for the DC components of the fields

and displacements, as only the carrier was considered. To include the noise sidebands, remember that each field is described by two quadratures. For example,

$$\boldsymbol{a} = \begin{pmatrix} a_1 \\ \\ a_2 \end{pmatrix} \tag{3.27}$$

where a_1 is the incoming laser amplitude and a_2 holds phase/frequency information of the incident field. Similarly, at zero carrier phase, the reflected field r is equal to field b, and the transmitted field t is equal to field g. Free space propagation of the beam is both a phase shift and a quadrature rotation (only the phase shift was considered for the carrier). Now to include the sidebands in this calculation, the quadratures must be evolved. This rotation affects equations 3.10 and 3.11 above, which now become

$$\begin{pmatrix} d_1 \\ \\ d_2 \end{pmatrix} = e^{i\omega\frac{L}{c}}\rho\left(\frac{\omega_0\delta L}{c}\right)\begin{pmatrix} f_1 \\ \\ f_2 \end{pmatrix} \tag{3.28}$$

and

$$\begin{pmatrix} e_1 \\ \\ e_2 \end{pmatrix} = e^{i\omega\frac{L}{c}}\rho\left(\frac{\omega_0\delta L}{c}\right)\begin{pmatrix} c_1 \\ \\ c_2 \end{pmatrix} \tag{3.29}$$

respectively. The rotation matrix ρ serves to evolve the sidebands and is given by

$$\rho\left(\theta\right) = \begin{pmatrix} \cos(\theta) & -\sin(\theta) \\ \\ \sin(\theta) & \cos(\theta) \end{pmatrix} \tag{3.30}$$

One can then solve this system of equations to obtain the transfer functions of the sidebands through the cavity, from the input field a to any other field. Numerical methods are usually best for this calculation as a noise sideband of a particular frequency can be propagated through the system and the response recorded, before proceeding to the adjacent noise sideband. Using this method, the transfer function from, say, an excitation in the input amplitude to the movable mirror position can be also mapped. This is done by calculating the radiation pressure force and converting to displacement, by supplying a known mechanical susceptibility (similar to the method of subsection 2.2.3). As Matlab is uniquely suited to matrix manipulation, code which performs this sideband propagation is presented in appendix C. It should be noted

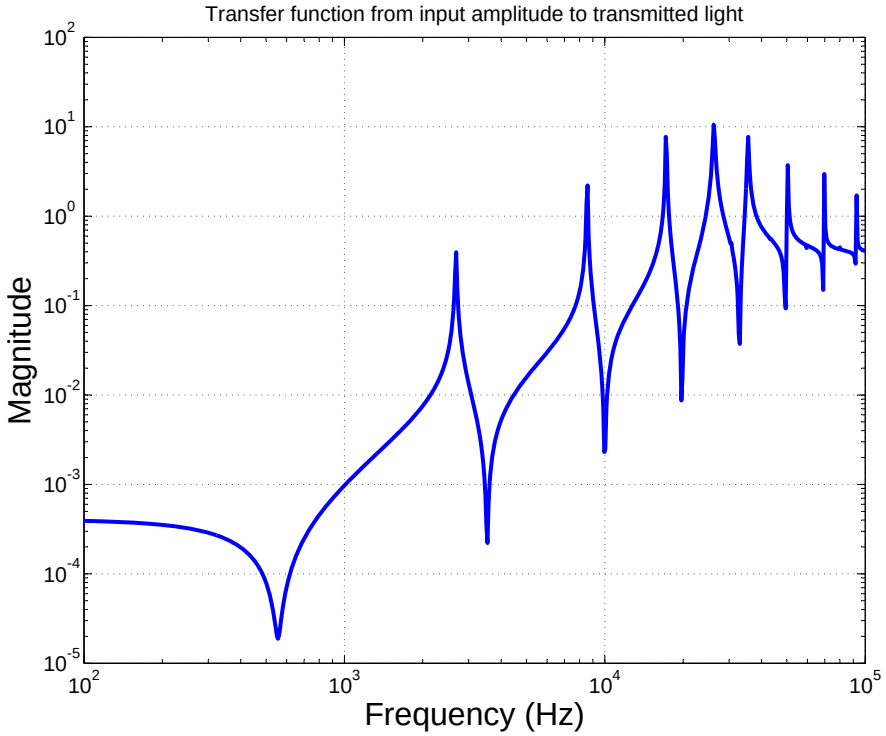

Figure 3.11: Sample output of the Matlab code showing the transfer function from input amplitude to transmitted light amplitude. The peaks and nulls originate in the mechanical susceptibility - as seen, for example, in equation 2.42 - and are modified by the presence of an optical spring (at approximately 30 kHz), which suppresses the optomechanical response at frequencies below the optical spring frequency.

that this formalism automatically includes the optical spring effect in the transfer functions, and that all transfer functions from the amplitude of the input field are normalized to the shot noise of that field.

Chapter 4

The experimental apparatus

This chapter documents the form and function of the individual subsystems which allow for the detection of cantilever motion. Additionally, in order to be dominated by either quantum or thermal motion, the noise in each of these system elements must be small. The system elements include the laser and light delivery layout, intensity stabilization, active and passive motional damping, imaging, cryostat and cryogenics, cavity control and locking and displacement sensing. Figure 4.1 illustrates the inter-connections of these subsystems.

A laser is used as a source of low noise coherent light to probe an optical cavity consisting of a large fixed mirror and a small compliant cantilever (the cantilever is detailed in chapter 3). The entire cavity is housed in a vacuum-sealed liquid helium cryostat capable of a minimum temperature of approximately 5 Kelvin. A control loop is used to stabilize the relative frequency between the laser and the cavity resonance. The control loop has two main paths - a slow path and fast path. The slow path actuates cavity length via a piezo attached to the fixed mirror. It has very large range, but very low bandwidth. The fast path uses the laser's frequency as an actuator and is capable of large bandwidths, but with very small range. Motional detection is accomplished by directly monitoring the transmitted beam power. The classical intensity fluctuations of the cavity input beam are monitored and suppressed using an intensity stabilization servo. The resonant motion of the cantilever is measured independently (but less sensitively) by an optical lever and this signal is used to damp the cantilever if necessary.

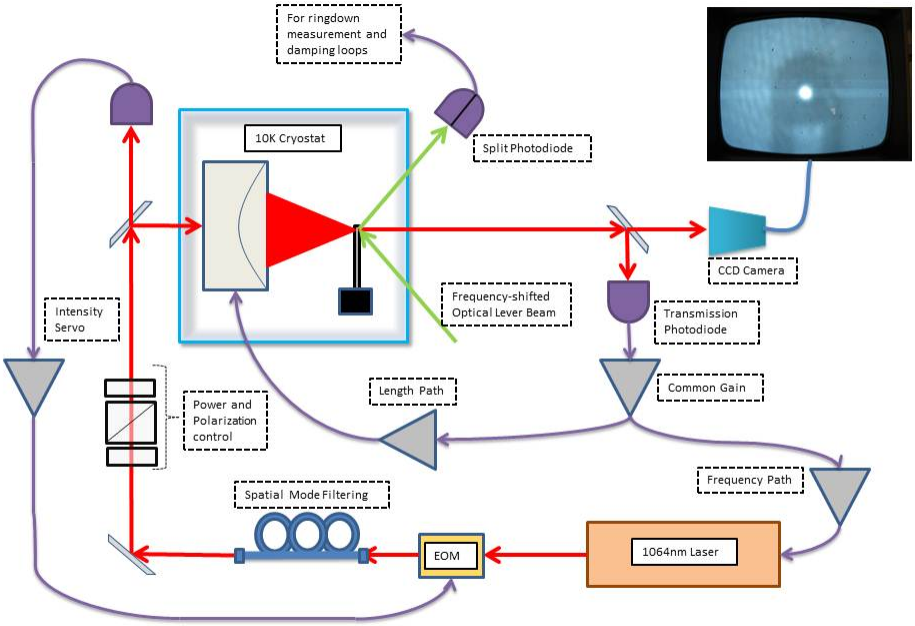

Figure 4.1: Simplified illustration of the inter-connections of the subsystems discussed in this chapter.

4.1 Laser and optical layout

The purpose of the laser system is to produce an output beam which, as closely as possible, resembles a coherent state. In order to accomplish this goal, both the classical laser phase noise and the classical laser amplitude noise must be suppressed to acceptable levels.

Firstly, a cavity tuned away from resonance acts as a phase/frequency to amplitude converter. If then the signal of interest modulates the amplitude of the transmitted beam, the laser phase/frequency noise influences the measurement. The solution here, in addition to the high bandwidth relative frequency stabilization discussed in section 4.7, is to make the conversion ratio small by increasing the ratio of the cavity linewidth to the laser linewidth - for high finesse cavities, this involves making the cavity as short as possible. Information about the laser phase/frequency noise can be measured by forming a beat note between a suitably reference-locked pre-stabilized laser and the laser to be measured. Unfortunately, this measurement required significant re-working of the experiment and relocation to a different room, and was therefore unfeasible. However a sibling laser, of the same type and specified performance, was measured by

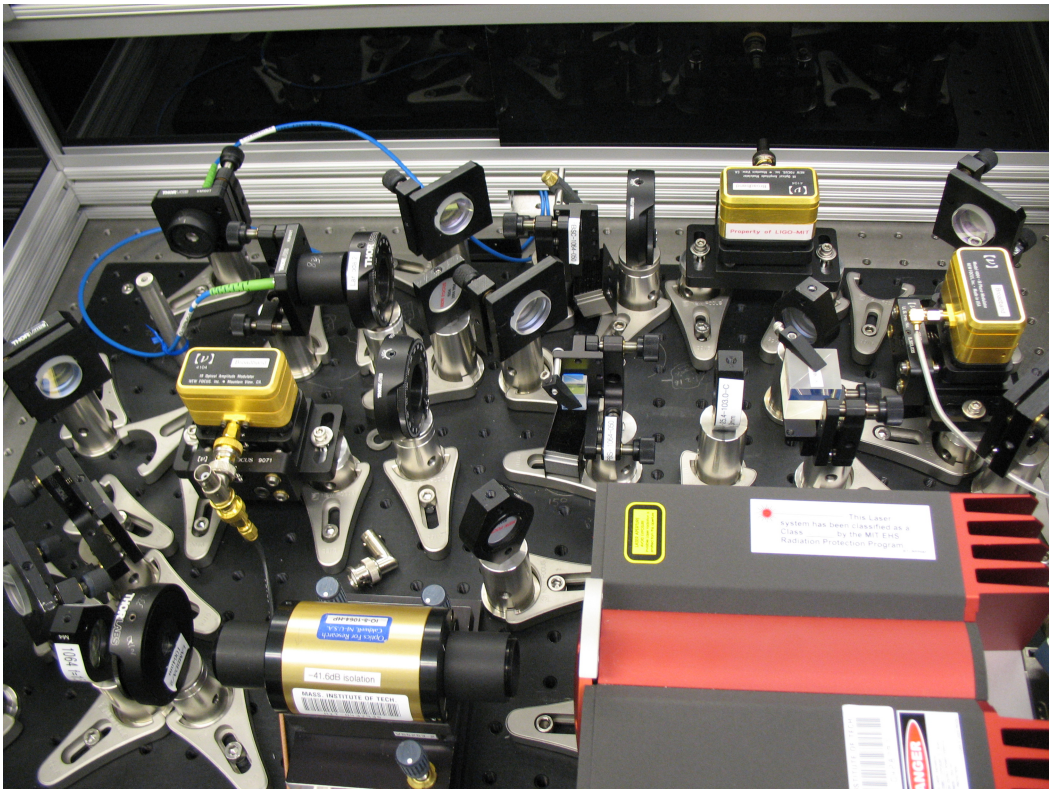

Figure 4.2: Picture of the laser enclosure showing the optical elements which produce a spatially-filtered, intensity-stabilized laser beam with any combination of phase and amplitude modulation.

the group of Danzmann [56]. Their measured frequency noise can be converted to an equivalent displacement noise (for a given set of cantilever and cavity parameters) using the transfer functions derived in section 3.7 and coded in appendix C. For a short cavity close to resonance being probed by a 1 kHz linewidth laser (small detuning is necessary for the full radiation pressure effect, see section 5.1) this effect is very small.

The larger issue concerns classical laser intensity noise. In an experiment seeking to alter a mirror's position through photon radiation pressure, if classical intensity noise persists, it becomes more difficult to attribute the mirror's motion to quantum effects. The inevitable solution in this case is to independently measure and suppress the classical intensity noise, prior to sending the light into the cavity.

The laser subsystem is pictured in Fig. 4.2. The Nd:YAG non-planar ring oscillator laser used in this experiment operates at 1064nm (Innolight Mephisto 500NE Serial # 1759B). It is driven by its companion Innolight controller (Serial # 1759B), which possesses an internal intensity noise suppression system (also known as a noise-eater) - for the suppression of the laser relaxation oscillation at a few hundred kilohertz.

At best, the laser produces approximately 500mW total but the output polarization is elliptical. As a result of this ellipticity, approximately 12% of the power is lost on the next optical element - the input polarizer of the faraday isolator. This isolator, with a measured isolation ratio of (41.7±1.0) dB, serves to prevent the return of light from the optical layout back to the laser - often such return light induces poor laser noise performance. The light out of the isolator is linearly polarized, and a half waveplate is then used to adjust it to s-polarization with respect to the subsequent steering mirrors.

A lens is utilized to make a narrow, collimated beam so that it can pass through the subsequent optical apertures. After the first steering mirror, there is a flip-up mirror used to couple large laser power into a fiber. This high power beam is only utilized in the removal of sacrificial pads. In usual operation, the flipper mirror is kept out of the way of the beam. The beam passed then through an amplitude modulator and polarizing beam splitter, which usually serve as the actuation point for the external intensity stabilization servo (see section 4.2).

At this point, the beam is split into two paths via a beam splitter. The paths were designed to have similar lengths, and therefore similar mode profiles at the ends. The first path is coupled directly into a single-mode polarization-maintaining fiber and is used in the optical lever setup. The beam in the second path goes through a phase modulator and then through another combination of amplitude modulator and polarizing beam splitter before being coupled into fiber. The phase modulator is used to introduce phase sidebands, used in certain locking schemes such as Pound-Drever-Hall stabilization. The amplitude modulator is mainly used as an input point for the measurement of optomechanical transfer functions (such as those derived in section 3.7). A half waveplate is used immediately before the fiber couplers, in order to align the polarization axis of the beam to the slow axis of the fiber. This procedure minimizes thermally-induced environmental drift of the light out of the fiber. The similarity of the two path lengths, along with the adjustability of the fiber coupler lenses, allowed for similarly high coupling efficiencies for both paths.

Overall, the laser system is capable of both phase and amplitude modulation, and any combination thereof. The main laser system is laid out on a portable breadboard and housed in a custom-built enclosure, with all the laser light coming out via optical fibers. This serves to increase the ease of potentially re-locating the laser system, and minimizes effects of dust and airborne particulates traversing the beamline or

accumulating on optical surfaces.

4.2 Intensity stabilization servo

The laser intensity noise couples into the measurement via two methods - firstly the direct transmission of laser intensity fluctuations through the cavity, and secondly via the direct driving of the mirror position. For this reason, the laser intensity noise must be reduced to the shot noise level of the cavity input power. Usually, it is the case that one can have a beam which is shot noise limited at a power much greater than the power entering the cavity, and so ensure that classical laser noise does not enter the measurement. This reduction of intensity noise to shot noise level is achieved via control feedback. The details of this feedback are presented in this section.

As stated in section 4.1, the laser used in this experiment possesses a built-in intensity noise suppression system (known as a noise-eater). However, the noise-eater only serves to reduce intensity oscillations at the laser's relaxation oscillation frequency, which is dependent on both current and temperature and typically occurs at several hundred kilohertz. Turning on the noise-eater prevents the output light from having a sharp spike of intensity noise at that frequency, via internal active sensing and feedback. However, this feedback is band-limited, and is therefore insufficient to provide shot noise limited intensity stability at frequencies of a few kilohertz. At these low frequencies, the intensity noise is dominated by classical intensity fluctuations.

To counteract these classical fluctuations, and reveal the quantum fluctuations of the light as a true coherent state, an external intensity stabilization servo is required. This servo works by directly sensing intensity noise on a pickoff beam and feeding back to an intensity actuator to reduce those fluctuations. Provided one can make the electronics noise of this loop negligible while maintaining reasonably high loop gain and avoiding loop saturation, it is possible to produce a beam of light which has intensity fluctuations limited by the quantum shot noise of the sensed light.

There are 3 major elements of the intensity noise reduction sub-system:

- Sensor photodiode and monitor photodiode
- Servo loop filter

- Intensity actuator

These are now detailed individually and their combined performance is provided.

4.2.1 Intensity stabilization sensor and monitor photodiodes

The intensity stabilization servo system has two photodiodes. One photodiode is in-loop and acts as an intensity noise sensor, while the other is out-of-loop and serves as an external monitor of the noise performance of the servo. These two photdiodes are made from the same electronic board (see E), but with different populated components. Functionally, the main difference lies in the inclusion of a zero-pole stage in the sensor photodiode after the transimpedance stage. This stage owes its origin to historical problems, within LIGO and LIGO-like experiments such as the 1g ponderomotive experiment, of loop saturation by large classical intensity fluctuations common at low frequencies. The ratio of the high-frequency to low-frequency sensor photodiode gain was designed to be 21 in order to avoid such problems, and has been measured to agree with design. The pole occurs at approximately 1kHz, so the sensor gain is still high within the measurement band of the experiment. The out-of-loop monitor photodiode does not possess this zero-pole stage. The overall bandwidth of these photodiodes is greater than 100kHz, but the monitor photodiode has an extra pole at 122kHz which was put into place to act as an extra anti-aliasing filter for the data acquisition machine (SR785).

4.2.2 Intensity noise servo filter

The purpose of the servo loop filter (see E) is to amplify and filter the sensor photodiode signal, and shape it appropriately for feedback to an actuator. It is required to have low noise and high bandwidth and, for this purpose, it was designed around THS3001 current feedback operational amplifiers. While being extremely well suited to this purpose, it is critical to make sure that these op-amps are not capacitively loaded. Even the stray capacitances on a board or the input capacitance of a downstream op-amp is enough to cause large oscillations at high frequencies (80-100MHz typically). These oscillations cause significant heating of the devices, degrades their performance and increases their failure rate. Placing small 50Ω resistors at the output pin of the THS3001 op-amps prevents these oscillations and does not impact the overall bandwidth.

4.2.3 Intensity actuator

The intensity actuator is a combination of a broadband modulator and polarizing beam splitter, and serves to imprint the control signal of the intensity stabilization loop onto the optical beam. The modulator electro-optically alters the polarization of the output beam, and the polarizing beam splitter converts those polarization modulations into intensity modulations. This actuator functions better than direct actuation to the laser current because it is capable of much larger feedback bandwidth. Loop bandwidths in excess of 1.1MHz are regularly achieved in this sub-system of the experiment, limited by the array of mechanical resonance of the amplitude modulator crystal, the first of which occurs at approximately 1.5MHz. This mechanical resonance is thought to come from the fact that the lithium niobate ($LiNbO_3$) crystal, as well as being an electro-optic material, also possesses a non-zero piezo-electric coefficient. Therefore an applied voltage at a particular frequency (related to the shape of the crystal and its electric contacts) is capable of significantly exciting a mechanical resonance.

4.2.4 Performance of the intensity stabilization servo

The residual intensity noise (noise power divided by DC power) of the stabilized laser beam is shown in Figure 4.3. It shows suppression of the classical laser intensity noise down to the $7\times10^{-9}\mathrm{Hz}^{-\frac{1}{2}}$ level which corresponds to the shot noise of approximately 28mW, the power incident on the sensor photodiode. It should be noted that the noise level can thus be lowered by simply sending more power to that photodiode. However, given that only a few microwatts of cavity input power are necessary, one can be very confident that classical intensity noise does not couple to the measurement.

4.3 Cryostat and cavity

Using the state-of-the-art mechanical oscillators presently available, the cryogenic part of this experiment is crucial to the successful demonstration of quantum noise through increase of the mechanical quality factor and reduction of the Brownian component of motion. This sub-system consists of a re-designed Janis ST-500 continuous flow cryostat (Serial #), with internal and external custom-built modifications for housing an optical cavity in a low vibration environment. The cryostat houses three attocube translation stages

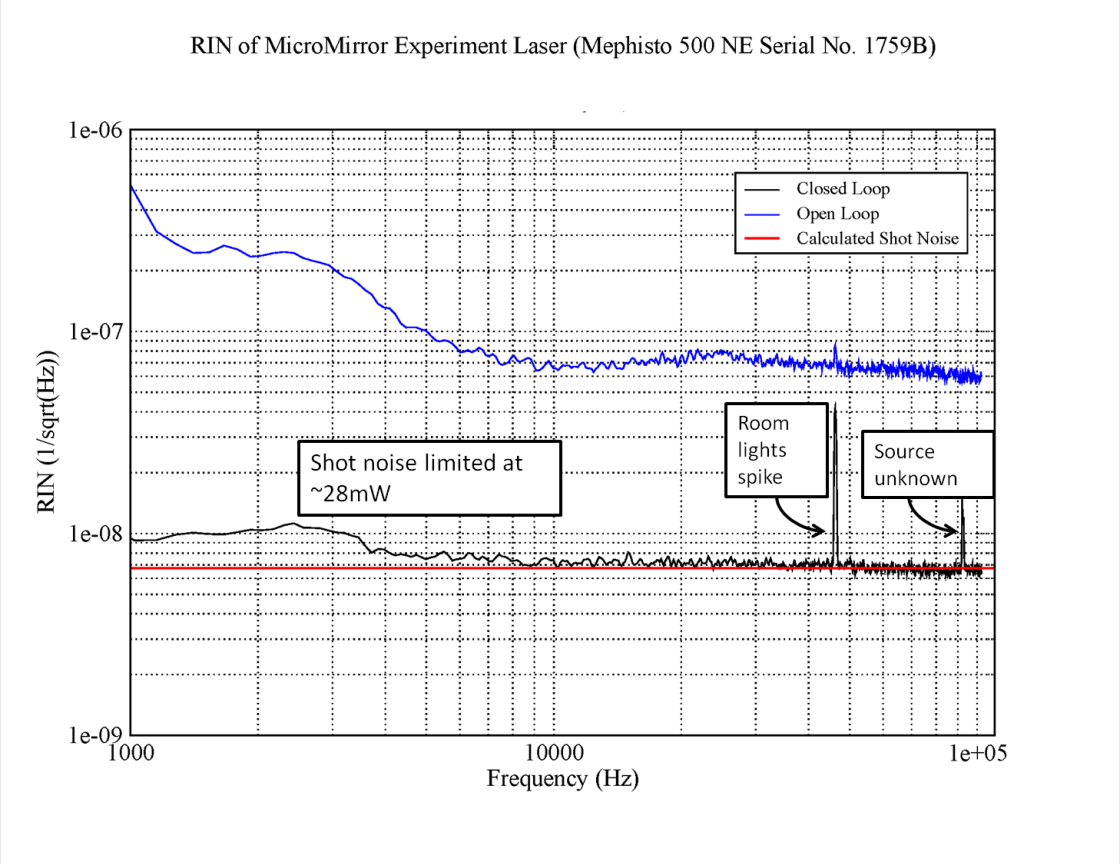

Figure 4.3: Residual Intensity Noise (RIN) of the laser system used in this experiment. Open loop indicates the Intensity stabilization loop is not in use, closed loop indicates that it is. The calculated shot noise line corresponds to approximately 28mW.

(ANPz101, ANPx101) which are capable of 5mm travel in 10nm increments at 10K. The standard procedure for cooling and re-warming the cryostat are included in Appendix A.

The cryostat is illustrated in cross-section in Figure 4.4. Liquid helium from a storage dewar flows into a helical heat exchanger which cools a cold plate. The cavity input coupler mounting tube and the radiation shield are both connected to this block, thus cooling in-vacuum metal surfaces. Sitting atop the cold plate are the three attocubes, with x and y direction attocubes on top of the z-attocube because of loading limitations (the z-attocube has a 200g load limit, compared to a 100g limit for both x and y). Immediately on top of the attocube stack is an aluminum sample block which houses a 25W heating resistor. The chip holder mounts

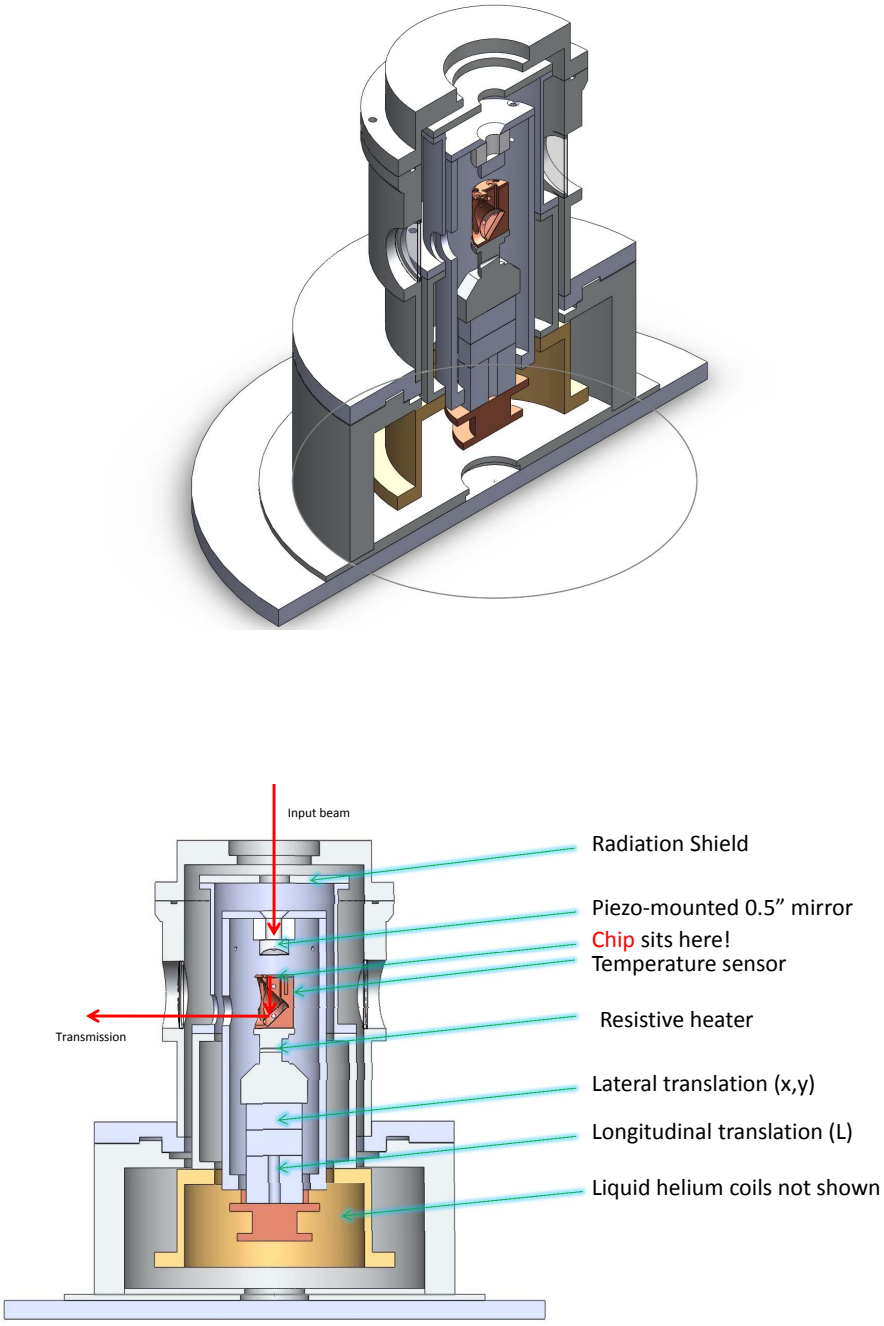

Figure 4.4: Cryostat overview.

directly to this sample block, and not only houses the chip, but also holds a 45-degree folding mirror for directing the cavity transmission beam through the available window. The cavity input coupler is connected first to an invar spacer, which itself is connected to a piezo. This piezo is then directly attached to the lid of the mounting tube. The purpose of the invar spacer is to match the temperature dependent properties of the glass mirror to those of the piezo. The emissivity of the invar is much larger than the mirror itself and the large contact area helps to conduct heat away from the mirror. Additionally, the coefficients of thermal expansion of the mounting tube lid, piezo, invar spacer and mirror are all sufficiently matched that none of the epoxy bonds (made using cryogenic-capable, thermally-conductive Stycast 2850 Epoxy) exceed the shear limits.

We now look specifically at the operation of the attocube stages, and the performance parameters of the optical cavity input coupler and piezo.

4.3.1 Attocube performance

Attocubes are cryogenically operable translator stages operated externally by the application of a control voltage. They are stackable, allowing for translation in all three spatial dimensions and are used in a wide variety of optomechanical experiments [57, 58, 59, 60]. Attocubes have been known to cause significant excessive displacement noise and are generally difficult to integrate into low noise precision measurement systems. However, with appropriate foresight and information about the types of attocube noise, attocubes and the associated driver electronics have been successfully employed in this experiment. Furthermore, the attocubes presently form an essential part of the ability to optically address an individual mechanical device on a chip-scale array consisting of numerous devices. The excess displacement noise can be broken down into two main categories, both of which have been successfully mitigated:

- **Normal mode motion of the attocube stack** – The stack of attocubes has been known to possess a significant flagpole motional mode. In other experiments which utilize attocubes, this motion has prevented optical cavity lock acquisition because it is thought to be more than a wavelength (λ=1.064μm) in amplitude at very low frequencies. A solution which has worked in other research groups is the use of other attocubes to push and clamp the main stack, thus preventing motion.

However, in this micro-mirror experiment, the cavity has been designed to be insensitive to the flagpole motion of the attocube. This design dictates a vertical cavity so that, to first order, cavity length is unaffected by the normal mode motion of the attocube stack.

- **Controller noise** – With the above design criterion in place, it is clear that the majority of excess noise from the attocubes come from the individual driver electronics for each attocube. In particular, the electronic output noise of the z-attocube driver module couples most significantly to the cavity length. There are two solutions to this problem, both of which are employed at various times in the experiment. Firstly, the attocube driver modules can be grounded at their output by a relay triggered from the user interface screen. This procedure should be done before any displacement data acquisition. The second method of mitigation of the electronic noise is to low pass filter the output of the driver before it goes to the attocube. Since the attocubes operate via an asymetric triangle wave stick-slip mechanism, this low pass filter unfortunately prevents translation of the attocube stage. However, the small range changes of the attocube stage are still possible by inserting a low-noise DC voltage into the DC input of the driver module. This low pass method is useful when aligning the cavity, or adjusting the cavity length to a specific value. The low pass filter was made to be employed or disengaged using a toggle switch, so as not to have to remove cabling or components. Figure 4.5 shows the effect of driver module noise on a displacement measurement.

4.3.2 Cavity alignment using attocubes

The inclusion of a 100μm mirror pad into an optical cavity leads to certain unique problems associated with the small lateral dimensions. Chief among these problems is the alignment of the optical beam to the mirror surface. Solving this problem was important in order to have a large percentage of the optical power in the TEM 00 cavity mode (which experiences the smallest diffraction losses of all the transverse cavity modes). Minimizing the diffraction losses leads to a higher coupling between the mechanical element and the intracavity optical field, and therefore a better sensitivity to quantum effects.

The first step in the proper alignment to the mechanical device is aligning to the chip edge. The chip

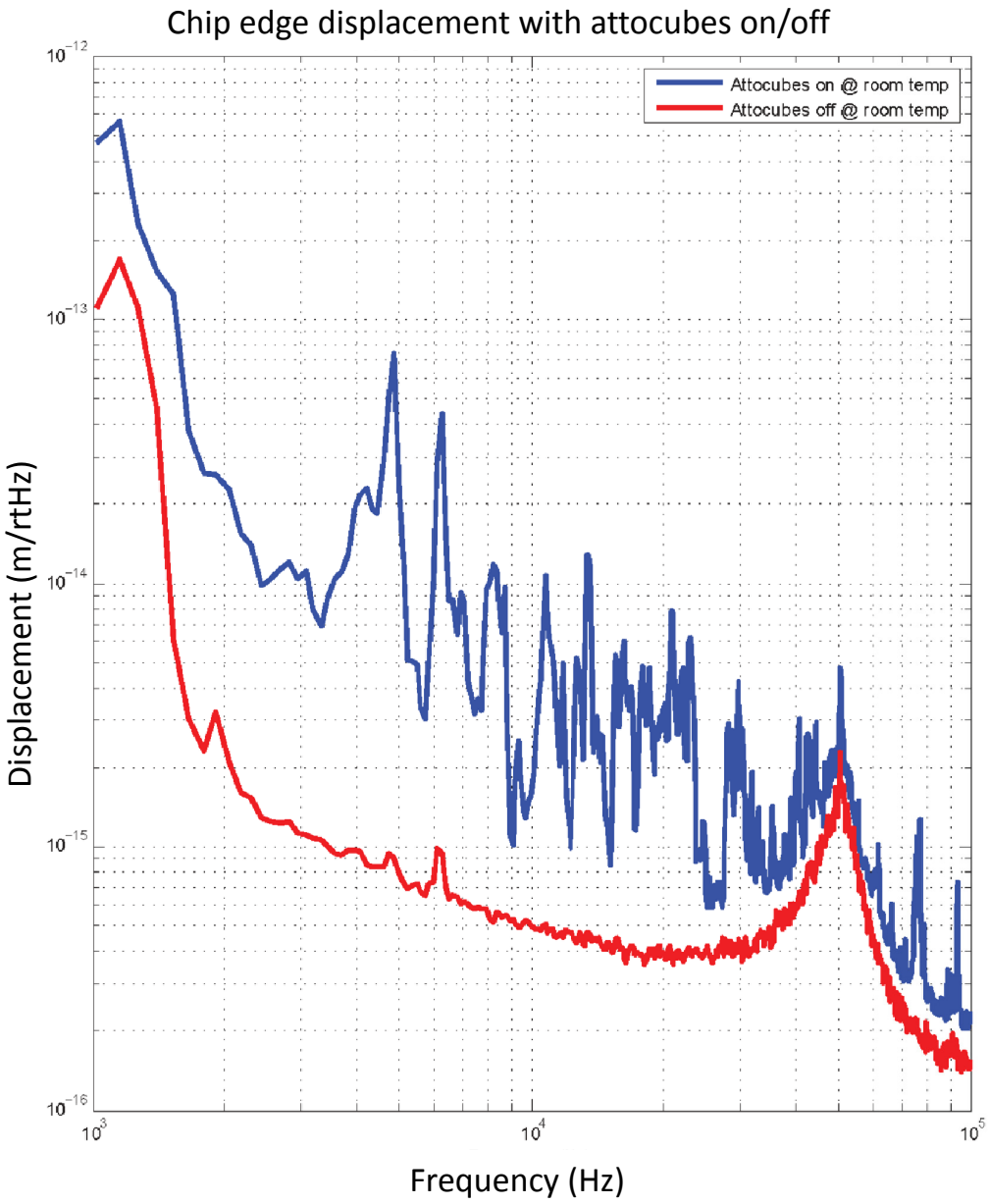

Figure 4.5: The effect of attocube driver noise on the chip-edge displacement measurement. The lower trace is a combination of thermal noise, acoustic environmental noise and electronics noise (solved in later measurements - see sections 4.7 and 4.7.1).

edge is as reflective as the oscillator itself, but does not have added complications due to the mechanical motion. Additionally, the chip edge is very close to parallel to the oscillator surface, and so it allows a close approximation to alignment to the device. The chip is translated into place using the attocubes. The reflection dip can be used as a measure of the coupling, and optimum alignment to the chip edge results in approximately a 25 % reflection dip. Note that the cavity length must be set to an appropriate value (close to the radius of curvature of the large input mirror) for the reflection dip to be a useful measure.

After aligning to the chip edge, the chip is once again translated so that the cantilever pad is in the cavity beam line. This is initially done without adjusting the input alignment into cavity. The optical lever damping loop is turned on, and the cavity length is scanned using the input coupler piezo. Often this results in the observance of broad resonance modes in the transmitted light intensity signal, but usually the modes can be narrowed significantly by fine-tuning the cantilever position to avoid light missing the device. Also, it has been noticed that the cantilevers sometimes sag, so that the cavity length is slightly longer on the cantilever compared to the chip edge. This sag is not attributable to gravity and it is thought to come from stresses in the material, possibly from the parent wafer, or from the fabrication and/or transportation of the devices.

At this point in the alignment procedure, it is usually possible to lock the cavity using the transmitted light. Once lock is acquired, the best measure for the coupling to between the mechanical device and the optical field is the optical spring. The optical spring is measured by a transfer function from, say, input frequency to transmitted intensity. By maintaining a fixed detuning and input power, this becomes a measure of the intracavity power. Small steps of the cantilever position will result in a measureable increase or decrease in the optical spring frequency, with the goal being to maximize the optical spring frequency at a particular input power and detuning.

Once this step is complete, it is useful to measure the displacement noise of the system as described in section 4.7.1. Here, one will often observe several additional mechanical modes coupling strongly to the readout. These modes are usually side-to-side modes which modulate the transmitted light intensity. By moving the mirror pad using the attocubes, one can usually decrease their coupling to the intensity readout. Figure 4.6 shows these additional modes in a displacement spectrum and compares it with a spectrum having

improved alignment.

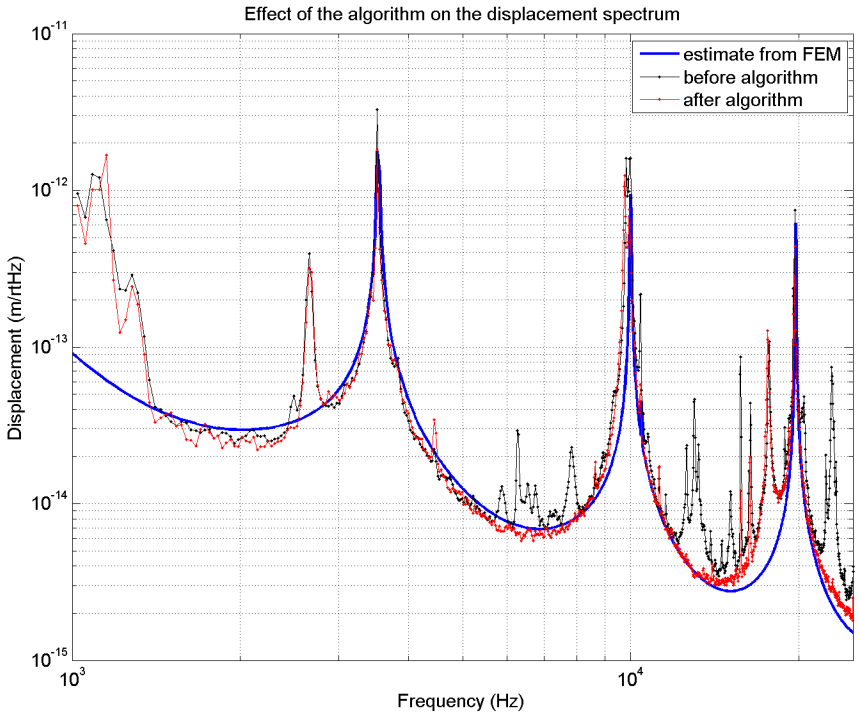

Figure 4.6: Effect of the alignment algorithm on the displacement spectrum of the oscillator. The extra mechanical modes in the black spectrum correspond to predicted frequencies in Ch. B but have lower modal mass due to the misalignment.

4.3.3 Cavity piezo

The design, characterization and installation of the cavity piezo are now detailed. As stated previously, the cavity piezo is the actuator for the length-path of the control loop stabilizing the laser to the cavity.

There are two parameters of significance for the cavity piezo - the piezo bandwidth and the full range for achievable voltages. Additionally, the properties of the piezo-electric material change with temperature and, at very low cryogenic temperatures, the piezo behaves markedly different from its performance at room

temperature. This change due temperature dependence of the piezo-electric material is manifested both as a decrease in the piezo range (displacement per unit applied voltage) and as a change in the mechanical resonances of the piezo. One key performance criterion is that the piezo must return to its original performance after a full thermal cycle is completed. In this experiment, it has been found that multilayer piezos tend to delaminate upon thermal cycling and their mechanical resonances shift downward in frequency. When this occurs, it renders them unusable since the parameters of the cavity control electronics must be repeatedly altered in a drastic fashion to compensate for the change. For this reason, a single layer piezo (Piezomechanik # Pit $10\times36\times1$) was selected for use as the cavity in-loop actuator piezo.

The piezo was first cut and sanded to approximately 9mm – a length which, along with the mounting tube spacer, allows the z-attocube to change the cavity length from an unstable cavity (L>1cm) to a stable one (L<1cm). The metallic sides of the piezo were gently brushed with an abrasive scrub to remove the oxide layer in preparation for soldering electrical wires. The piezo was then rinsed and the electrodes were wiped clean with acetone. Electrical wiring (single-strand cryogenic manganin wire, Lakeshore #WSL-32-100) were then soldered on with vacuum compatible solder. The piezo was then bonded to the mounting tube lid using Stycast 2850 cryogenic epoxy. After curing, the invar spacer was then similarly bonded to the piezo and then, in turn, the cavity input mirror was attached to the invar spacer.

Firstly, the bandwidth of the piezo – especially in a cryogenic setting – is the factor which most significantly determines the crossover between the length path and frequency path of the cavity locking control loop. The bandwidth is determined by the frequency of the first mechanical resonance of the device, which depends on the piezo's construction, shape, material composition and temperature. Fig. 4.7 shows a measurement of the mechanical resonance of the piezo at room temperature before thermal cycling, at cryogenic temperature, and after a complete thermal cycle. The measurement was performed by creating a Michelson interferometer with the piezo-mounted input coupler and a fixed mirror. By then sitting on the side of an optical fringe, the motion of the piezo-mounted mirror can be mapped onto detectable amplitude fluctuations of thelight from the Michelson interferometer.The before-cycling and after-cycling piezo performance is found to be identical, even after several thermal cycles.

Additionally the cryogenic range of the piezo, in comparison to the expected deflection of a device,

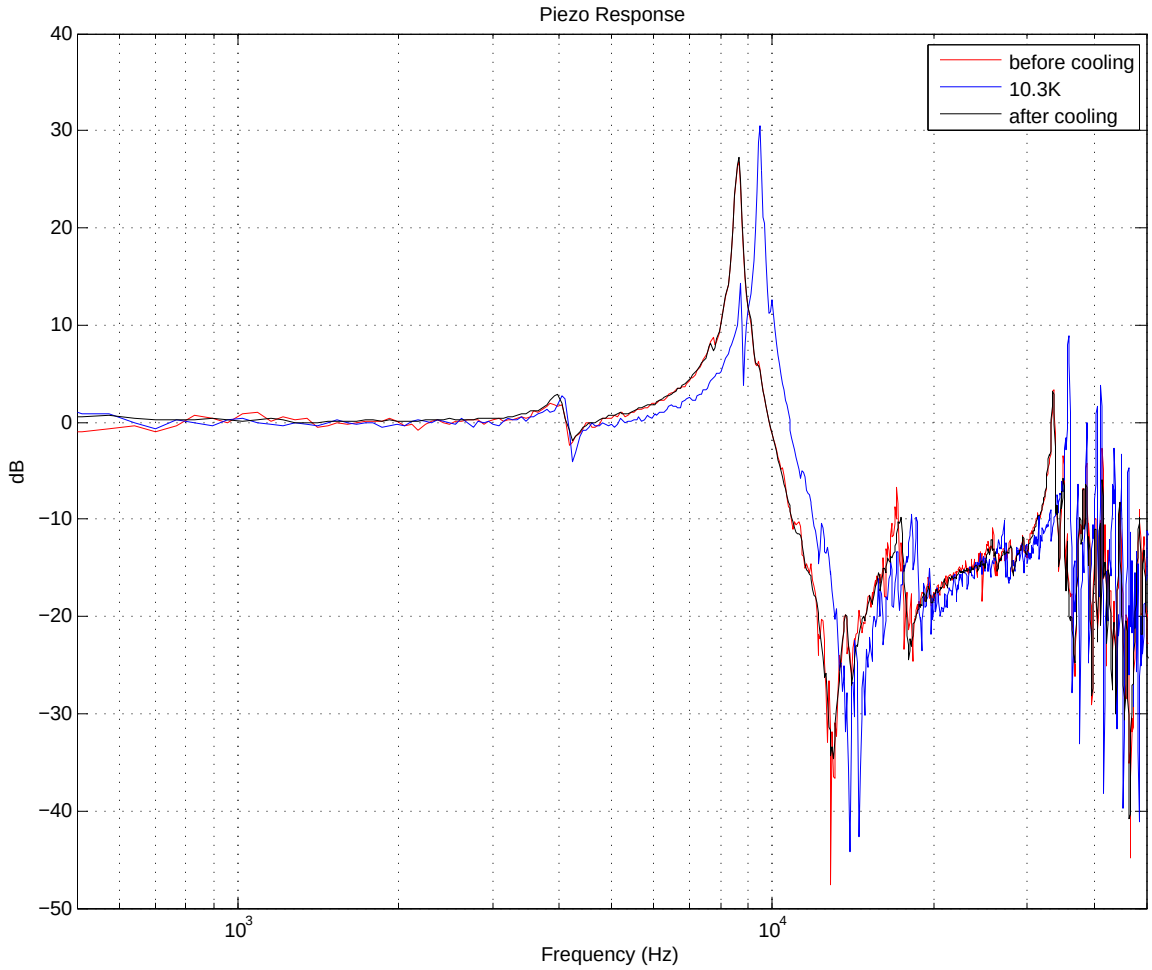

Figure 4.7: Mechanical response of the single-layer cavity length actuation piezo (normalized to DC) at cryogenic temperatures as well as at room temperature before and after thermal cyling. The measurement was performed by creating a Michelson interferometer with the piezo-mounted input coupler and a fixed mirror.

determines whether the locking servo can follow the motion of the device and keep the system stably locked. In this experiment, the most significant contribution to the DC deflection of the mechanical device is due to the radiation pressure force of the circulating field:

$$F_{\text{rad, DC}} = \frac{2P_{\text{circ}}}{c} \approx 5 \times 10^{-10}\text{N at } 100\text{mW} \tag{4.1}$$

where c is the speed of light in vacuum. The spring constant of a mechanical device can be found simply by

$k = m\omega_{\rm r}^2$ where m is the modal mass of the first mechanical resonance and ω_r is its resonance frequency. If one then requires that the piezo range be more than the DC radiation pressure deflection, one arrives at the requirement that

$$R_{\rm piezo} > \frac{2P_{\rm circ}}{m\omega_{\rm r}^2 c} \tag{4.2}$$

where $R_{\rm piezo}$ is the accessible piezo range for available voltages. The piezo currently used in this experiment has a maximum estimated range of 3.1μm for 850V applied at room temperature. Cryogenically, this range is found to decrease by a factor of approximately 10. Using this piezo, and for mechanical oscillators currently available in this experiment, the requirement in Equation(4.2) limits the resonant frequency to approximately 500Hz with a modal mass of approximately 1ug. These parameters are sufficient to be able to observe quantum radiation pressure with presently available oscillators.

4.3.4 Cavity input coupler

The cavity input coupler, along with the AlGaAs Bragg devices, determines the optical properties of the cavity. The mirror vendor specifications are listed in Table 4.1. In addition to the vendor specifications, laboratory characterization of the mirror was undertaken.

Laser-Optik Coatings and Substrates	
Art. No.	L-06078
Batch No.	02060q2
HR 532nm + 1064nm/6° s	
RS. : AR 532nm +1064nm/0°	
2 Q2 ∅12.7 × 6.35mm r=-10mm	

Table 4.1: Vendor specifications for the cavity input coupler

Two identical mirrors were used to form a Fabry-Perot cavity of length 16.5mm. The length was limited by the radius of curvature of the mirrors (1cm) and the optical cavity stability requirement (see section 3.2.3). By scanning the cavity length and observing the full-width half-maximum (FWHM) of the of

the transmission fringes in comparison to the free spectral range (FSR), the cavity finesse $\mathcal{F}$ was determined by $\mathcal{F} = \frac{\text{FSR}}{\text{FWHM}}$ to be approximately 130000. This gives a mirror reflectivity of $1 - (25 \pm 10)$ppm at 0° incidence. It was necessary to conduct this measurement inside a vacuum enclosure to avoid air currents, and the cavity length was scanned very slowly to avoid issues related to the photodiode bandwidth (50MHz). Along with the AlGaAs Bragg multilayer reflectivity, this mirror is sufficient to create a cavity with a high enough optical finesse to observe quantum radiation pressure with the current mechanical devices. These measurements are in agreement with those made on similar coatings (see Appendix D), tested separately for use in the LIGO Hanford H1 Squeezing Experiment and under consideration for use in prototype filter cavities [61].

4.4 Vacuum system

The vacuum system of this experiment serves to mitigate damping due to dissipation in a gaseous environment, and force noise due to background gas collisions. Truly accurate models of this source of dissipation and noise rely on geometry specific numerical simulations such as those presented [62]. However, in the free molecular flow regime where gas pressure is high enough for gas-damping to occur but simultaneously low enough for the mean free path of molecules to be large compared to the oscillator size, device quality factors are expected to have an inverse dependence on pressure $Q_m \propto \frac{1}{P}$ [63]. In this experiment, the mechanical quality factors have remained constant over approximately 2 orders of magnitude of pressure - this seems to indicate that gas damping does not significantly contribute to the overall mechanical loss.

In order to ensure this lack of pressure dependence, a clean low-vacuum enclosure was necessary. There are two main pumping systems for this experiment, a Hi-Cube turbo pump (with integrated diaphragm backing pump) and an ion pump (which is always left turned on, but is valved off at appropriate times). The turbo pump is a high volume pump but acoustically and vibrationally noisy. Once a pressure of approximately 10^{-6} torr is obtained, the turbo pump is valved off and powered down (to reduce vibration coupling to the experiment). The ion pump alone is sufficient to maintain 10^{-6} torr pressure at room temperature.

During cryostat cooldown, the ion pump alone has access to the experimental vacuum space. The pressure drops from 10^{-6} torr to 10^{-8} torr as the cryostat goes from room temperature to 10K, and often

it is possible to valve off the ion pump when the cryostat is cold – the cold cryostat becomes a better pump than the ion pump, which sometimes begins to outgas. Warmup is a critical stage for the vacuum system as there is a pressure spike which occurs at approximately 190 K. This spike is often capable of overwhelming and saturating the ion pump so, as the cryostat warms, it is necessary to engage the turbo pump and valve off the ion pump until the cryogenic system reaches room temperature.

4.4.1 Environmental perturbations and acoustic noise

Due to the low resonant frequency and high mechanical quality factor of the mechanical oscillator, environmental perturbations need to be guarded against. Despite being housed in a high vacuum cryostat, external acoustic noise still couples to the measurement by mechanical means. The main sources of these external perturbations are non-laminar flow in nearby ventilation ducts in Rm 069 and the high capacity cleanroom blowers housed in the same laboratory. Those sources make it impossible to make thermal noise limited measurements below 1 kHz. Once lock is acquired, these perturbations are not sufficient to break lock but nevertheless may impact the baseline displacement sensitivity of the measurement. The solution to these perturbations has been to turn off all cleanroom fans and adjust flow in the ducts to minimize impact to the experiment. Additionally, there are short-duration burst events which interrupt measurement. These have been traced to anthropogenic sources and are significantly smaller and less frequent when the building is less populated and the optical table is floated. Fig. 4.10 also shows a wall of acoustic noise below 1 kHz which prevents measurements at very low frequencies.

4.5 Optical lever and motional damping

The optical lever, as utilized during the course of the experiment, is a means of reducing the damping time of a highly-excited mechanical mode. It is usually not used when the cavity is locked (optical lever light is manually blocked), but is highly useful in damping the oscillator so lock can be acquired. It speeds up the process of aligning a cantilever to the cavity beam because translating the chip excites significant mechanical motion and active damping reduces the ringdown time. The optical lever damping system consists simply of motional detection, bandpassed filtering, and feedback to device motion.

The motional detection consists of a 80MHz-shifted optical beam which bounces off the back of the mechanical oscillator at a significant angle. The shift in the frequency of the optical lever beam with respect to the cavity beam not only prevents the cavity from being resonant to the optical lever but also looks ahead to demodulation-type locking, which should be insensitive to the optical lever light. The light reflected off the back of the oscillator is then sent to a split photodiode. As the oscillator moves, the beam spatially moves from one side of the split photodiode to the other side. The difference signal of the two halves of the split photodiode therefore contains information about the motion of the oscillator. This technique is commonly used in the optical detection of motion from AFM cantilevers [64, 65], as well as on a large scale with LIGO [66, 67]. Transfer functions from driven cantilever motion to the optical lever photodiode difference signal show spikes at the mechanical resonances due to the pronounced motion at those frequencies.

Once the motion is detected, the signal is bandpassed to isolate motion from the mechanical resonances. It is advantageous to use SR560 and/or SR650 adjustable filters, so that damping filters can be easily modified for different mechanical oscillators within the same chip. The phase of the feedback signal can be adjusted by changing cable lengths and feedback sign, as well as the bandpass filter properties. It is not required to have the exact correct phase, since it is not completely necessary to have a critically-damped oscillator - only an increased ringdown rate is necessary.

This filtered motional signal is then fed back to the device motion via the attocubes, using the AC inputs of the attocube controller. It is possible to simultaneously damp both the transverse and longitudinal motion of the cantilever by feeding back the appropriately bandpassed signals to the corresponding attocube inputs. Extreme care should be taken to monitor the optical lever signal when first initiating the damping loops because the wrong sign of feedback will lead to an increasing motional amplitude and possible damage to the mechanical device. Additionally, the damping feedback may become unstable if the device is translated significantly, due to the fact the the optical lever beam spot may be hitting a different part of the cantilever motional shape.

In addition to the active damping of the cantilever motion via optical lever feedback, it is also possible to passively damp the motion when the cantilever is cryogenic. This is simply accomplished by turning on a bright visible light source, possibly by a mechanism similar to that presented in [68]. Note that

the exact mechanism for this damping has not been extensively studied in this experiment, but one possible hypothesis entails charge-carrier generation within the cantilever leading to dissipation of mechanical energy. This passive damping method has the advantage of being easy to do, since no alignment is necessary, and once the visible light source is turned off, the mechanical quality factors return to their original values. However, it is only possible at cryogenic temperatures and the ringdown times achieved via this passive method are usually still longer than those obtained via active damping. The experiment is usually operated in a darkened room - to avoid stray room lights reducing the oscillator's mechanical quality factor.

4.6 Imaging

The imaging of the cantilever devices is very important, since it aids in alignment and reduction of diffraction losses by proper micro-mirror positioning. It is possible in this experiment because of the back-side window etching (see §3.3), which produces completely free-standing mechanical structures. Therefore optical access is possible from both sides of the device. The same visible light source which is used to passively damp the cryogenic mechanical devices also is utilized to provide a shadow image of the cantilever. The transmission path is common to the main signal beam, but the visible imaging light is always turned off during measurement to avoid data corruption. A partially reflective beam splitter separates part of the transmitted light, both visible and infrared, for detection on a CCD camera. This camera produces real-time images such as those shown in Fig. 4.8 on a monitor viewable from all parts of the laboratory. Often it is even possible to see the blurred and aliased motion of the cantilever, in the side-to-side direction, on the monitor.

4.7 Cavity sensing and control

In this experiment, the cavity was locked using a DC transmitted side-of-fringe lock. The light through the cavity is detected by a photodiode (see Appendix E) and an adjustable DC offset (referred to as the error offset) is subtracted to produce the error signal. Although this means that the detuning can in principle never be zero, detunings as low as about 0.4 linewidths have been experimentally demonstrated in this experiment using this method. Therefore the loss of sensitivity to quantum noise due solely to non-zero

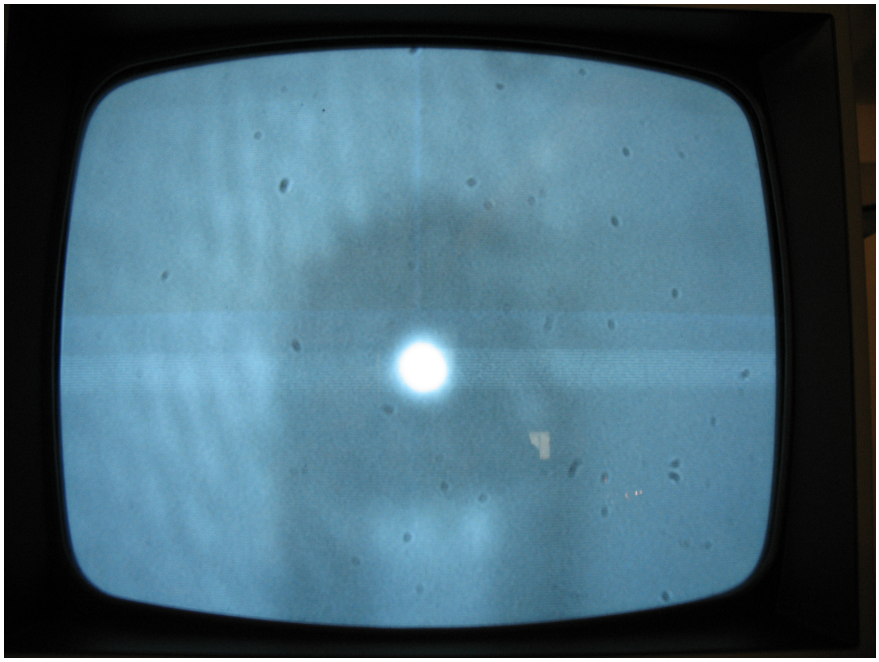

Figure 4.8: Image on the transmission CCD camera of a locked cavity mode. A dual-support device (device 7) is shown.

detuning is small. The error signal is filtered and appropriately split into two paths to feed back to both the laser frequency and the cavity length. This dual-path feedback is necessary in order to have both large loop bandwidth and large actuation range.

A combination of large signal gain at the photodiode and a differential receiver at the end of the transmission line helps to mitigate any laboratory pickup in the long cables. The signal is then passed through a low noise pole-zero gain stage which boosts it further before it is fed into a P-I controller (LB1010). The P-I controller possess large dynamic range, but unfortunately its effective noise figure is quite large, so the zero-pole gain stage is necessary for low noise loop operation.

4.7.1 Displacement sensing

The process of measuring the displacement noise of the optical cavity is now detailed. Displacement sensing consists of measuring an error signal at an appropriate point in the control loop and recording the appropriate calibration spectrum. Using these two pieces of information, one can re-calibrate into displacement noise units. With the optomechanical effects in this highly deformable cavity, including the

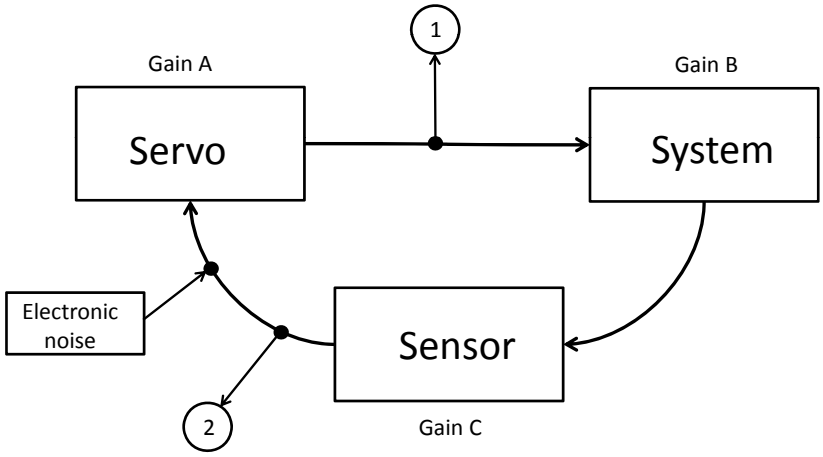

Figure 4.9: Block diagram of the control loop for locking the laser to the cavity. In the diagram, the Servo (with gain A) includes the control loop filter, the System (with gain B) includes the piezo drivers as well as the laser and optical cavity, and the Sensor (with gain C) includes the photodiode. Points 1 and 2 are measurement points discussed in the text. The majority of the electronic noise can be modeled to enter at the input to the servo box as shown.

response of the optical cavity is necessary to convert the error signal to a displacement. This response (calculated in section 3.7) is obtained by directly measuring the transfer function of an injected frequency excitation to the error signal at a point just after the PI controller. Measuring at this point is necessary, because it improves the signal to electronic noise of the measurement by a factor of the overall loop gain. This feature comes from the fact that the majority of the electronics noise originates in the P-I controller (see §4.7.2).

4.7.2 Electronics noise

It is a criterion for successful and robust measurement of quantum effects that electronics noise be lower than quantum noise. With modern low noise figure amplifiers, this is easy to achieve experimentally. The primary concern is knowing where in the control loop the noise is being introduced. For this experiment, the controller is the primary source of noise as stated in sections 4.7 and 4.7.1 and illustrated in figure 4.9.

If one measures at point 1 in figure 4.9, the relative gain of the signal compared to the electronic noise can be written as

$$\left(\frac{S}{N}\right)_1 = \frac{C(\omega)A(\omega)}{A(\omega)} = C(\omega) \tag{4.3}$$

where $C(\omega)$ is the sensor gain, $A(\omega)$ is the controller gain. Similarly, at point 2, this quantity becomes

$$\left(\frac{S}{N}\right)_2 = \frac{C(\omega)}{A(\omega)B(\omega)C(\omega)} = \frac{1}{A(\omega)B(\omega)} \tag{4.4}$$

where $B(\omega)$ is the system gain shown in figure 4.9. Dividing equation 4.3 by 4.4 shows that performing a measurement at point 1 in the loop has a benefit of suppressing the coupling of electronic noise to displacement by a factor of the total open loop gain $A(\omega)B(\omega)C(\omega)$. This effectively means that a recording of the error signal measurement after the controller in the control loop has the benefit of a boost to the overall signal-to-electronics-noise ratio by a factor of the overall loop gain compared to a measurement at the transmission photodiode, due to the fact that the noise is effectively introduced at the controller input. Fig. 4.10 shows a displacement measurement where the electronics noise was dominant because the error signal was acquired at the photodiode.

4.8 Noise estimations from noise coupling calculations

All the laser noise couplings have been calculated in section 3.7. This formalism, together with the associated code in Appendix C, allows the estimation of noise contributions to the total displacement spectrum. For instance, a transfer function from input amplitude to displacement can be obtained from the code and, since this response is normalized to shot noise, it represents the expected quantum radiation pressure noise. The expected contributions from classical amplitude and frequency noise can be obtained in a similar manner.

Figure 4.11 shows a best estimate for the expected performance of a displacement measurement made on device 7 for a cavity on optical resonance. Thermal noise curves are shown for both room temperature and achievable cryogenic temperature. The contributions due to classical amplitude noise and radiation pressure noise both indicate a series of nulls and peaks near the mechanical resonance. These features are inherently due to the mechanical susceptibility of the oscillator, as can be seen in the derivation presented in section 2.2.3, particularly equation 2.42 and also discussed in figure 3.11. As discussed in section 4.7.2, the electronics noise is dependent on the servo loop gain (higher loop gain gives lower noise) so a routinely achieveable ballpark is presented where the readout point has been moved to after the servo control filter

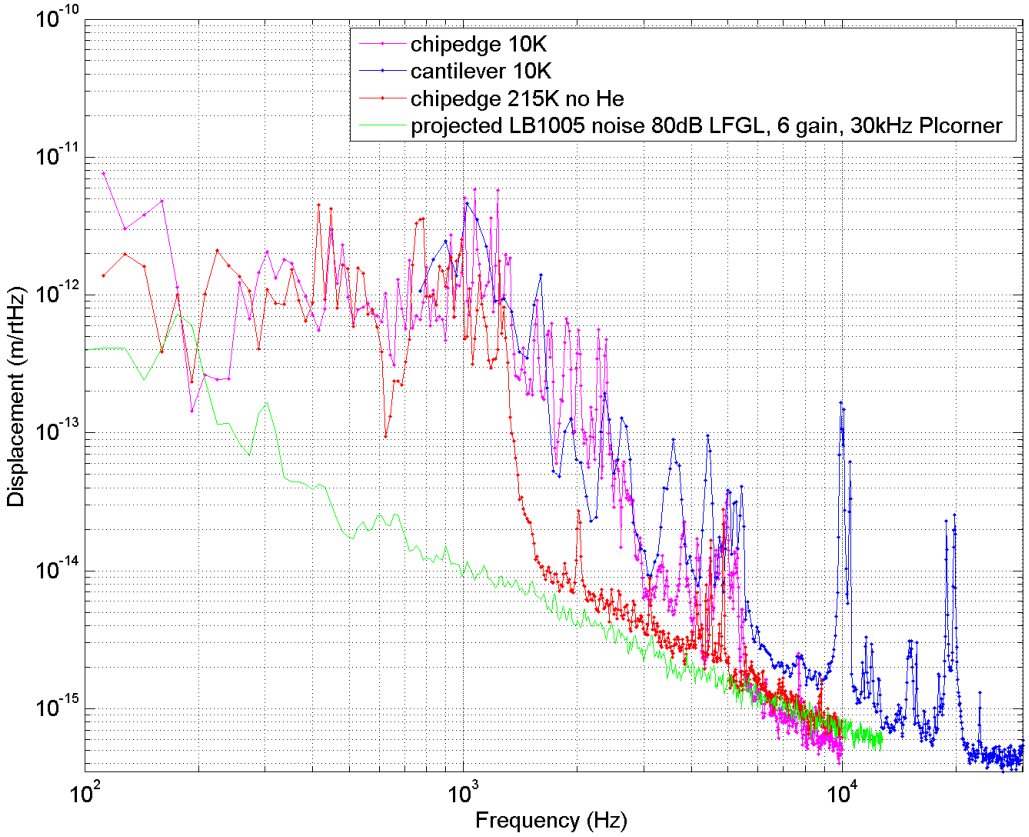

Figure 4.10: Sample displacement noise with dominant electronics contribution in the band of 2kHz to 20kHz. The environmental noise can also be seen in both the chip-edge and cantilever spectra below approximately 1kHz.

(instead of at the photodiode in figure 4.10). Note that the shape of the control loop gain will alter the form of the electronics noise. For example, in certain situations (particularly those involving a detuned cavity) the optomechanical response of the cavity causes peaks and nulls in the loop gain, resulting in corresponding features in the electronics noise contribution. The laser frequency noise coupling does not appear on this estimate, owing to the fact that it is predicted to have a negligible coupling to the measurement. Due to the fact that the cavity detuning is zero, the frequency noise coupling is fully expected to be small. In fact, the direct calculation of this coupling at zero detuning is limited to the numerical precision of the Matlab code presented in Appendix C. Note that other displacement noise sources, such as environmental perturbations

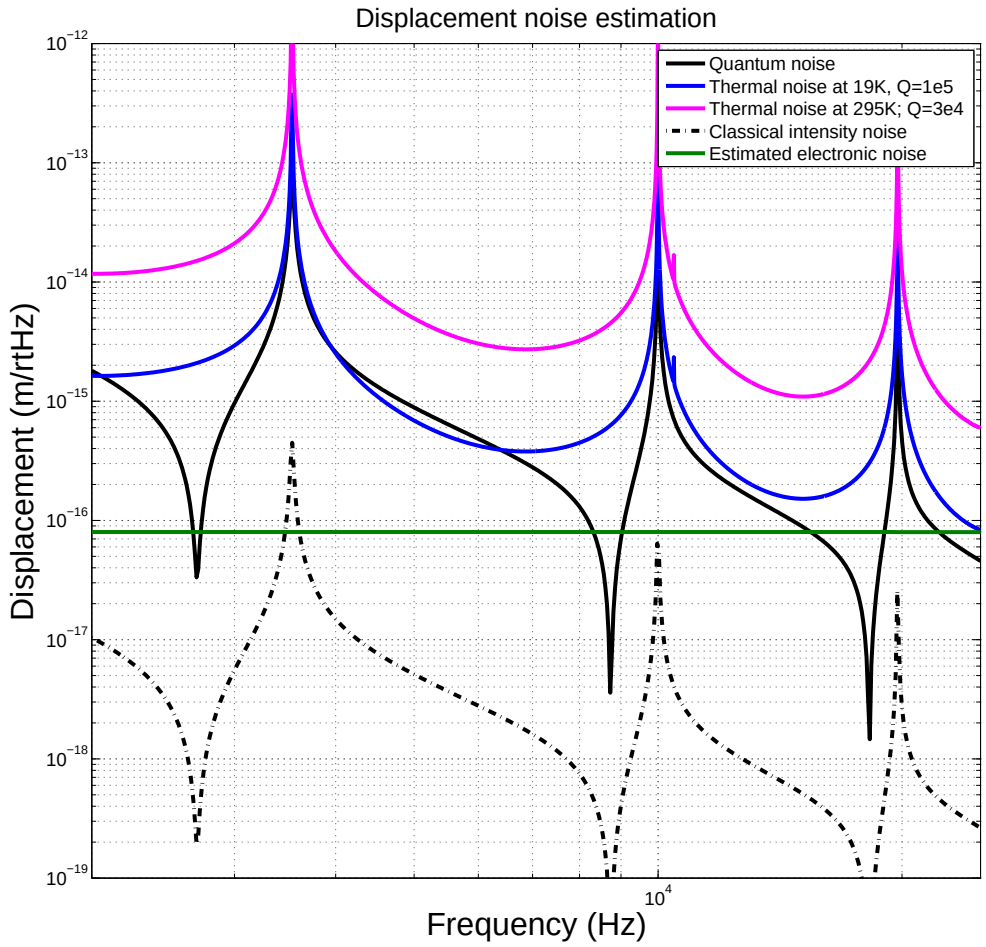

Figure 4.11: A reasonable estimate of the noise contributions for an optical cavity on resonance consisting of a feasible mechanical oscillator (in this case, device 7), with the qualitative form of the curves discussed further in the text of section §4.8. Other potential noise sources, such as environmental noise, are not presented.

from acoustic sources or helium flow, have not been estimated due to the difficulty in precisely modeling the coupling of these sources to the optical cavity. However, from the noise budget presented in figure 4.11, one can reasonably conclude that the best frequency to measure quantum effects would be near 5 kHz. At that frequency, the quantum noise contributes roughly half the total displacement imprecision.

4.9 Comparison between models and measurements for actual mechanical devices

Displacement measurements at room temperature and at cryogenic temperatures have both been observed to agree with the spectrum predicted by the finite element model (FEM). For example, Fig. 4.12 shows the close agreement at room temperature of the FEM and measured spectrum for device 10. Note that there is a mode at approximately 20 kHz which appears with a lower effective modal mass than expected. It is also observed to be alignment dependent. The FEM predicts a mode at this frequency, but it should oscillate in-plane and have very little coupling to the cavity length. However, it is believed that diffraction losses - though small - still allow a portion of the detected field to be modulated by in-plane motion, leading to an apparent longitudinal motion at that frequency.

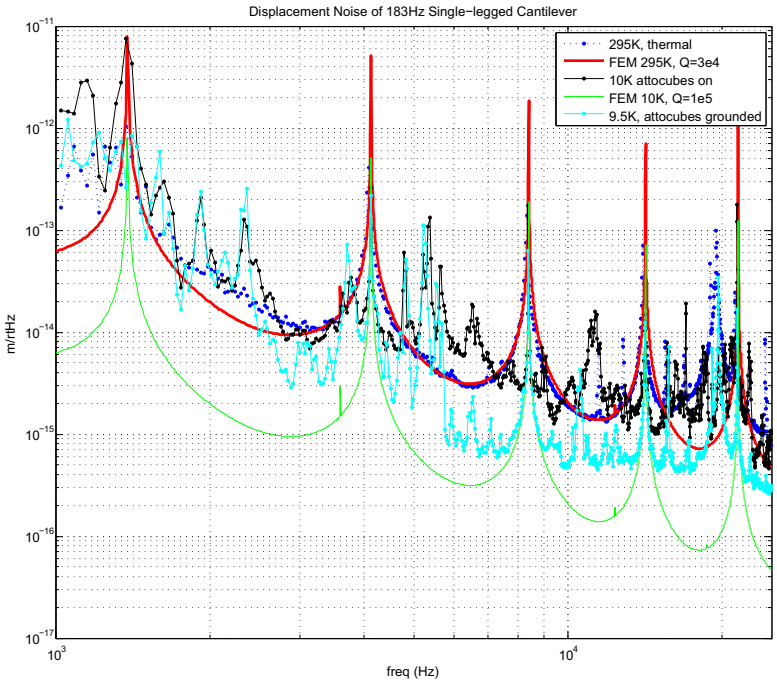

Figure 4.12: Displacement spectrum of a 183 Hz cantilever (device 10, freed from sacrificial pad). Due to cryogenic range limitations of the cavity length actuator (see §4.7), there is extra noise on the measured cryogenic spectrum which prevents an approach to the predicted 10K line.

Device 7 possesses a much higher fundamental resonance frequency and thus its motion was within the cryogenic range of the length actuator. As shown in Fig. 4.13, the FEM and measurement are in close agreement both at room temperature and cryogenic temperature. The modes between 10 kHz and 20 kHz illustrate the alignment dependence of the coupling of in-plane motion to the amplitude quadrature readout.

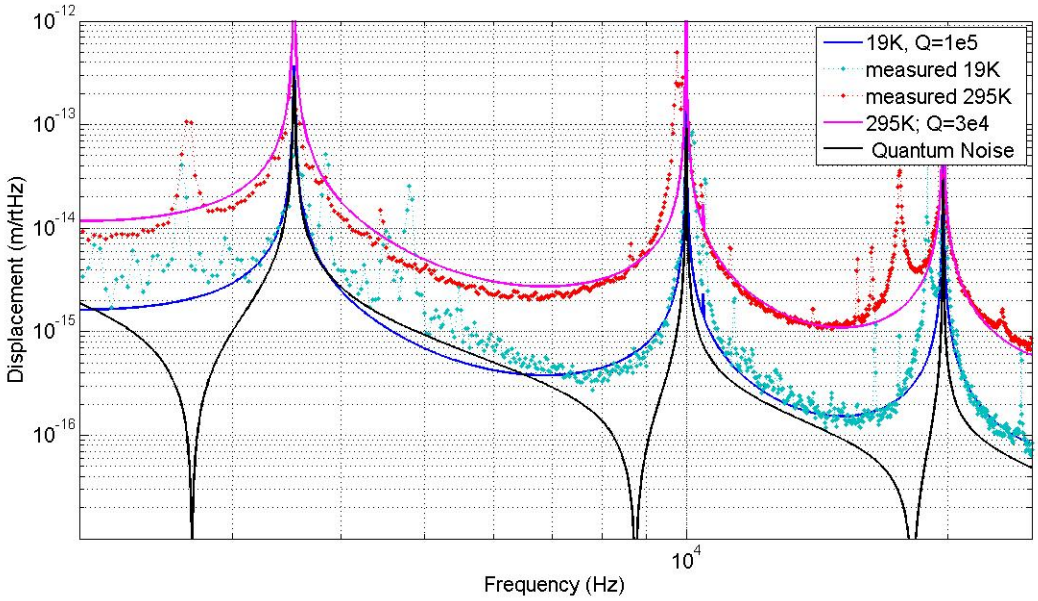

Figure 4.13: Displacement spectrum of device 7, with an estimate of the quantum backaction one would sense with a phase-sensitive readout system.

Near 5 kHz, the place of closest approach to quantum noise, the measured noise floor is seen to deviate from the thermal noise limited spectrum. The source of this excess noise has not been confirmed, and it is quite possible that it may result from environmental perturbations of the optical cavity.

Chapter 5

Quantum-limited displacement measurements and beyond

In this chapter, some of the future improvements to the experiment are detailed.

5.1 A deformable optical cavity on resonance

Undetuning the optical cavity is very important for the successful demonstration of quantum radiation pressure noise. As a function of detuning, the magnitude of the radiation pressure force F_{RP} scales as a Lorentzian

$$F_{RP} = \frac{4I_0\mathcal{F}}{\pi c}\frac{1}{1+\delta^2}$$

where $\mathcal{F}$ is the cavity finesse, $I_0$is the input intensity, and δ is the detuning in linewidths. This reduction in the effect cannot be compensated for by increasing the power, since the cavity is already operated near the breakage threshold of the oscillators. However, due in part to the high compliance of the oscillators and the formation of a significant optical spring, undetuning is not as straightforward as for a non-deformable (or low compliance) cavity.

For a cavity locked via a transmission side-of-fringe method, it is required to maintain a small detuning and thus a small reduction in the radiation pressure effect. It also means that optical springs should be expected. Even with other locking schemes, the cavity and oscillator parameters result in the astounding fact that in order to have an optical spring past the first mechanical resonance, a detuning of only 10^{-6} linewidths is required. Therefore, the locking system must be able to deal with these optical spring effects, because it is very difficult to avoid them.

Figure 5.1 shows a measurement of the magnitude of the loop gain for a locked cavity, repeated several times as the cavity is undetuned. It is clear that there are many unity gain crossings, all of which must remain stable not only at one particular detuning and power, but also during the process of reducing the detuning. Due to the change in the optical spring frequency, the optical transfer function is modifed and thus the loop gain is altered. From the most undetuned trace in figure 5.1 it was determined that the minimum achievable detuning was 0.4 linewidths - corresponding to a radiation pressure effect that is 86.2% of the predicted undetuned effect. This reduction is small enough that does not substantially impact the detection of quantum noise, but clearly the measurement would be easier if the remaining 13.8% was available. This improvement should be possible with a Pound-Drever-Hall type lock, or homodyne lock, so long as care is taken to avoid an unstable optical spring.

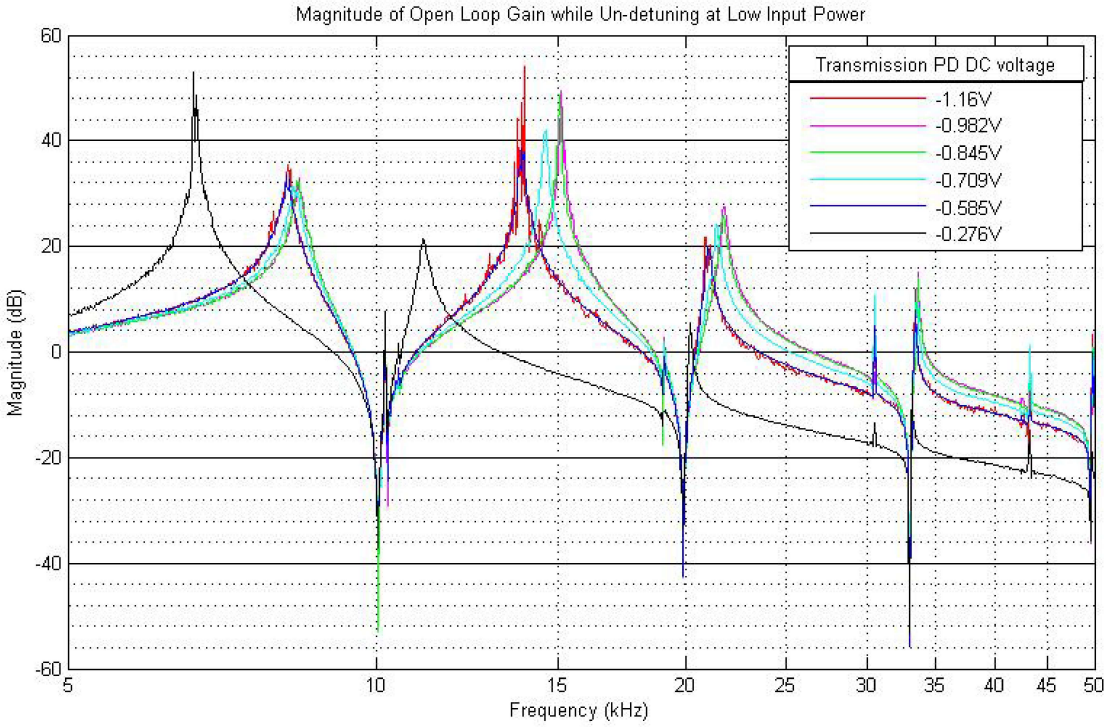

Figure 5.1: Magnitude of the loop gain as the cavity is undetuned. The optomechanical response of the cavity changes due to the shift of the optical spring - this leads to a change of the frequencies of multiple unity gain points. Using the transmission photodiode to illustrate the reduction of the frequency offset from optical resonance, one can see the optical spring move out to higher frequency then turn around and return towards lower frequency. The detuning corresponding to the maximum optical spring occurs at approximately 0.5 linewidths.

Finally, it has been noted that the optical cavity is more easily undetuned when it is cryogenic than at room temperature. Although this observation needs to be investigated further, it has been theorized that the change in the sign of the thermal expansion coefficient, coupled to optical absorption, may play a role.

5.2 Motional detection quadrature

Initially, at the start of the experiment, the assumption was made that the side-of-fringe measurement scheme was sufficient for measuring the backaction of the probe laser, but this has unfortunately proven to be incorrect. Numerical calculations imply that in the presence of a dominant optical spring, the cavity dynamics suppress the backaction of the probe on the optomechanical system if the amplitude quadrature of the transmitted light is measured.

This problem was discussed by several LIGO quantum measurement groups and a theory of the process involved became apparent. Following the method of [69], we can gain some physical intuition for this unexpected result. If one measured the amplitude quadrature, the field fluctuations δa seen by the transmission photodiode come from three sources:

$$\delta a = \delta a_{\mathrm{direct}} + \delta a_{\mathrm{BA}} + \delta a_{\mathrm{vac}} \tag{5.1}$$

(1) In-cavity amplitude fluctuations δI_q when the mirror is not moving couple to the detected output amplitude fluctuations

$$\delta a_{\mathrm{direct}} = \frac{\delta I_q}{2I_{\mathrm{in}}} \tag{5.2}$$

(2) Mirror motion δx coupling to output amplitude change

$$\delta a_{\mathrm{BA}} = \frac{1}{2I_{\mathrm{in}}}\left(\frac{\delta I_{\mathrm{in}}}{\delta x}\right)\delta x \tag{5.3}$$

(3) Directly reflected vacuum fluctuations from the output mirror δa_{vac}

However, in the presence of a strong optical spring, the motion of the mirror can be dominated by the optical spring force, leading to

$$\delta x = \frac{2\delta I_{\mathrm{q}}}{c}\frac{1}{k} \tag{5.4}$$

where $k = \frac{-2}{c}\left(\frac{\delta I_{\mathrm{in}}}{\delta x}\right)$ is the optical spring constant. Therefore, equation 5.3 becomes

$$\delta a_{\mathrm{BA}} = \frac{1}{2I_{\mathrm{in}}}\left(\frac{\delta I_{\mathrm{in}}}{\delta x}\right)\left(\frac{2\delta I_{\mathrm{q}}}{c}\right)\left(\frac{-2}{c}\left(\frac{\delta I_{\mathrm{in}}}{\delta x}\right)\right)^{-1} = -\frac{\delta I_q}{2I_{\mathrm{in}}} \tag{5.5}$$

Therefore, from equation 5.2 and equation 5.5, the amplitude quadrature measurement at the photodiode reduces equation 5.1 to

$$\delta a = \frac{\delta I_q}{2I_{\mathrm{in}}} + \left(-\frac{\delta I_q}{2I_{\mathrm{in}}}\right) + \delta a_{\mathrm{vac}} = \delta a_{\mathrm{vac}} \tag{5.6}$$

and the detected amplitude fluctuations is due entirely to the reflected vacuum fluctuations. It should be noted here that although this process relies on a radiation pressure sensitive optomechanical system and the radiation pressure is necessary in this derivation, it is not a direct canonical detection of radiation pressure.

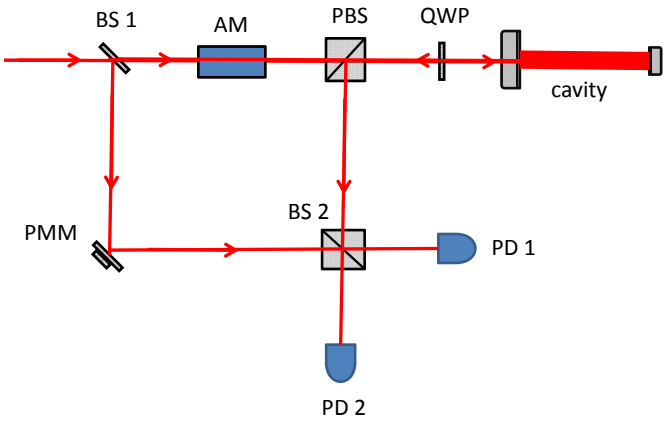

Figure 5.2: Another possible locking scheme, with the benefit of detection in a backaction-sensitive quadrature. Use depends on the suitability of the optical components (whether future cavities are overcoupled, undercoupled or impedance-matched) to a reflection-type lock. The labels refer to beamsplitter (BS1 and BS2), amplitude modulator (AM), polarizing beamsplitter (PBS), quarter-waveplate (QWP), Piezo-mounted mirror (PMM) and photodiode (PD1 and PD2).

For that, one would need to detect in the phase quadrature or avoid all optical spring effects. For this experiment, as stated in section §5.1, the avoidance of an optical spring past the first mechanical resonance is highly unlikely, especially at powers compatible with the observation of quantum backaction - so the only avenue is the change of detection quadrature.

5.3 Improved locking schemes

There are several locking schemes which are insensitive to this effect, by virtue of being phase quadrature measurements. The primary one is the use of demodulated transmitted phase sidebands to sense mirror motion (transmitted PDH technique), but there are others.

For example, consider the situation shown in figure 5.2. A laser beam is split into two paths - the first path goes through an amplitude modulator and interacts with the optical cavity. The modulator inroduces amplitude sidebands with a modulation index γ and at a frequency ω_{AM} (which is much greater than the cavity linewidth and, therefore, does not enter the cavity). The carrier, however, does enter the cavity. The two beam paths are then re-combined at a beamsplitter and both output ports are detected using photodiodes.

Assuming an equal splitting ratio at the beamsplitter, the photodiode signal at detector 1 is then

$$I_1 \propto \left| \frac{A}{2} e^{i\omega_0 t}(2\gamma \cos(\omega_{\mathrm{AM}} t) + R_{\mathrm{cav}}(\omega_0) e^{i\phi_{\mathrm{cav}}}) e^{i\pi} + \frac{B}{2} e^{i(\omega_0 t + \phi_{\mathrm{PL}})} \right|^2 \tag{5.7}$$

where $R_{\mathrm{cav}}(\omega_0)$ is the reflection coefficient of the cavity, ϕ_{cav} is the phase accumulated in the cavity and ϕ_{PL} is the relative phase shift due to difference in lengths of the two paths. Expanding out the squared term, and suppressing the dependence of R_{cav} on the carrier frequency, one can then write out the explicit form

$$\begin{aligned} I_1 \propto \tfrac{A^2}{2} \left(4\gamma^2 \cos^2(\omega_{\mathrm{AM}} t) + R_{\mathrm{cav}}^2 + 4\gamma \cos(\omega_{\mathrm{AM}} t)\cos(\phi_{\mathrm{cav}})\right) + \tfrac{B^2}{4} \\ - \tfrac{AB}{4} \left(4\gamma \cos(\omega_{\mathrm{AM}} t)\cos(\phi_{\mathrm{PL}}) + 2R_{\mathrm{cav}} \cos(\phi_{\mathrm{cav}} - \phi_{\mathrm{PL}})\right) \end{aligned} \tag{5.8}$$

This relationship can be written in terms of the components at DC and at ω_{AM}

$$I_1^{\mathrm{DC}} \propto \frac{A^2}{4}(R_{\mathrm{cav}}^2 - 2\gamma^2) - \frac{AB}{2} R_{\mathrm{cav}} \cos(\phi_{\mathrm{cav}} - \phi_{\mathrm{PL}}) \tag{5.9}$$

$$I_1^{\omega_{\mathrm{AM}}} \propto \gamma \cos(\omega_{\mathrm{AM}} t) \left(A^2 \cos(\phi_{\mathrm{cav}}) - AB \cos(\phi_{\mathrm{PL}})\right) \tag{5.10}$$

and all other terms are dropped. This same calculation can be performed for detector 2, giving

$$I_2^{\mathrm{DC}} \propto \frac{A^2}{4}(R_{\mathrm{cav}}^2 - 2\gamma^2) + \frac{AB}{2} R_{\mathrm{cav}} \cos(\phi_{\mathrm{cav}} - \phi_{\mathrm{PL}}) \tag{5.11}$$

$$I_2^{\omega_{\mathrm{AM}}} \propto \gamma \cos(\omega_{\mathrm{AM}} t) \left(A^2 \cos(\phi_{\mathrm{cav}}) + AB \cos(\phi_{\mathrm{PL}})\right) \tag{5.12}$$

Let us first consider the difference between the two photodiode output at DC. This differential signal is simply

$$I_2^{\mathrm{DC}} - I_1^{\mathrm{DC}} \propto AB R_{\mathrm{cav}} \cos(\phi_{\mathrm{cav}} - \phi_{\mathrm{PL}}) \tag{5.13}$$

The difference signal at the sideband frequency ω_{AM} can be obtained by demodulation of the full difference signal at ω_{AM} with a demodulation phase ϕ_{dm}

$$I_2 - I_1 \Big|_{\text{demod at } \omega_{\mathrm{AM}}} \propto AB\gamma \sin(\phi_{\mathrm{dm}}) \cos(\phi_{\mathrm{PL}}) \tag{5.14}$$

From equations 5.13 and 5.14, the differential photodiode output contains two components: one signal at RF which is proportional to $\cos(\phi_{PL})$ where ϕ_{PL} is the path length difference between homodyne arms, and one signal at DC which is proportional to $\cos(\phi_{\mathrm{cav}} - \phi_{PL})$ where ϕ_{cav} is the phase shift of the light due to mirror motion. The RF component is demodulated and this error signal is driven to zero using a piezo

actuator (PMM in figure 5.2), implying a $\frac{\pi}{2}$ phase difference between the homodyne arms. This condition then forces the DC signal to be proportional to $\phi_{\rm cav}$ for small cavity phase deviations, and thus a useful measure of mirror motion. There are also several other such techniques which are available for phase sensitive detection in the optical regime.

5.4 Sensitive modulation techniques

The introduction of modulation techniques can be very useful for improving the sensitivity to quantum noise. Consider the the introduction of a slow modulation of the input light intensity at a frequency much less than the fundamental mechanical resonance. If one were to then bandpass the displacement signal at a frequency of maximum quantum-to-thermal noise ratio, a demodulation of the bandpass signal would lead to a much greater sensitivity to power dependent sources such as quantum radiation pressure. In fact, using this method one can be sensitive to quantum fluctuations which are much smaller than the thermal Brownian fluctuations.

One point to note about such schemes is the requirement that the displacement signal be continuously calibrated as the input power is slowly varied. This is especially tricky when dealing with substantial optical springs, but it can be accomplished by the introduction, demodulation and recording of multiple calibration lines of the displacement signal.

5.5 Oscillator improvement

It is clear that the majority of the thermal noise in the measured band is not contributed by the fundamental mechanical resonance, and this has prompted the development of better oscillator designs. One such possible design utilizes thinner supports for the mirror pads. This design change has the effect of lowering the modal mass (which increases the ratio of quantum to thermal noise as $\sqrt{m}$). Special wafers, with a pre-grown stop layer in the midst of the Bragg layers, are utilized in a modified version of the fabrication method presented in section §3.3. The thin support allows the cantilever to be made very short, approximately a few hundred microns, whilst maintaining similar fundamental resonant frequencies to the present design. The accuracy of the finite element analysis developed during the course of this work allows

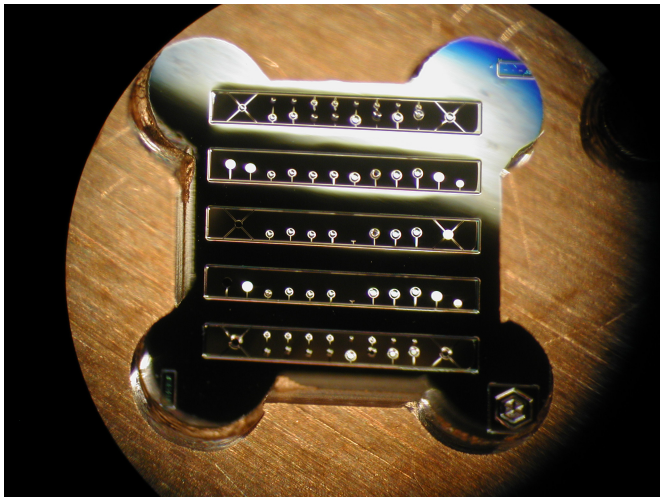

Figure 5.3: Photograph of an improved oscillator design. The chip itself is situated in a copper holder utilized for safe transportation and storage. There are several rows of devices - the oscillator pads can be seen as reflective circular pads on single supports or as multi-support structures. The design is based upon the FEM analysis detailed in section §3.4.

confidence in designing such structures. Provided the new geometries do not suffer from lower breakage thresholds or reduced Q_m, it is possible to increase the ratio of quantum to thermal noise by increasing the spacing between mechanical modes, as well as decreasing the modal mass.

Additionally, the optical loss of the wafer from which the mechanical oscillators are etched is thought to be approximately 70 ppm (measured using photothermal common path interferometry by G. Cole and collaborators). Ideally, for the oscillators to be used in an interferometer incorporating squeezing, those losses would be reduced. Little is known about the source of the optical losses in the AlGaAs multilayer. Investigations have been made into the carbon content of the parent wafer. It was theorized that the carbon was the source of the optical losses, ultimately leading to the development and use of low-carbon wafers. However, these new wafers showed no improvement in absorption losses and, in some cases, proved to be more absorptive.

The process of oscillator improvement using the finite element model has already begun, and is primarily headed by the Corbitt group at Louisianna State University (LSU). Figure 5.3 shows a chip made with several new geometries with expected improvement in performance.

5.6 Cryogenics

Given that thermal noise is second only to quantum noise as the largest expected noise contribution, it is clear that the experiment would benefit from achieving lower temperatures. Although it has been accomplished [70], the simultaneous operation of a sub-kelvin dilution refrigerator and an optical system is a daunting prospect. Unlike the experiments with optical systems in dilution refrigerators, this experiment has a very low measurement frequency and fundamental mechanical resonance frequency. The chief concern at frequencies of a few hundred hertz is the introduction of vibrations into the measurement. This worry can clearly be overcome by appropriate suspension systems, but in a confined enclosure with limited cooling power, it becomes difficult. Nevertheless, should one overcome these problems, the benefit is clear - not only is the thermal noise reduced directly as the square-root of the bath temperature, but the Q_m is also expected to continue to increase as the temperature is lowered.

Chapter 6

Concluding remarks

In this thesis, I have presented research on an experiment which is capable of realizing a long-held goal of the optomechanics community - an optical interferometer with a sensitivity limited by the quantum fluctuations of the probe field. This work involved the development of suitable oscillators and the integration with an optical cavity. Furthermore, I described the measurement of the most significant source of non-quantum noise - the thermal motion of the mirror - and its mitigation through the implementation of cryogenic cooling. The modeling of this mirror and its resulting thermal spectrum have been investigated and advanced significantly over the course of this research.

This experiment is at a very interesting and exciting point. It is believed that, were it not for the backaction suppression effect described in 5.2, there would be a strong possibility of having an overall displacement noise spectrum with a significant contribution from quantum radiation pressure noise. Although this unforeseen effect was a somewhat unfortunate hindrance in our search for quantum radiation pressure noise, it has opened up new ideas to the optomechanics community - for instance, concerning backaction evasion in double optical spring systems [71]. Significantly, the noise suppression effect does not occur in the phase quadrature of motion (even with an optical spring present). This implies that a change to the system to allow for phase quadrature detection will ultimately result in the measurement of broadband quantum noise, and that venture is currently underway.

Finally, this experiment has much potential for the near and long term future. With detection of quantum noise in this system, comes the possibility of significant advances in the injection - or ponderomotive generation [72, 73]- of squeezed states at low frequencies. Additionally, the experimental realization of small-

scale quantum filter cavities will be within reach [74, 75, 76]. These experiments are very interesting and important for precision measurement (and specifically Advanced LIGO) and, partially as a result of the work presented in this thesis, these studies are closer to becoming a tangible reality.

Bibliography

[1] Noise for the 5th science run. LIGO Document Control Center G070366-00.

[2] S. Hild. Beyond the second generation of laser-interferometric gravitational wave observatories. Classical and Quantum Gravity, 29(12):4006, 2012.

[3] Albert Einstein. Über das relativitätsprinzip und die aus demselben gezogene folgerungen (on the relativity principle and the conclusions drawn from it). Jahrbuch der Radioaktivität und Elektronik (Yearbook of Radioactivity and Electronics) 4, 1907.

[4] Albert Einstein. Einfluss der schwerkraft auf die ausbreitung des lichtes (on the influence of gravity on the propagation of light). Annalen der Physik, 35, 1911.

[5] Albert Einstein. Die feldgleichungen der gravitation. Sitzungsberichte der Preussischen Akademie der Wissenschaften zu Berlin, 1915.

[6] Albert Einstein. Die grundlage der allgemeinen relativitätstheorie. Annalen der Physik, 49, 1916.

[7] Albert Einstein. Kosmologische betrachtungen zur allgemeinen relativitätstheorie. Sitzungsberichte der Preußischen Akademie der Wissenschaften, 1917.

[8] R.A. Hulse and J.H. Taylor. Discovery of a pulsar in a binary system. The Astrophysical Journal, 195:L51–L53, 1975.

[9] J.H. Taylor, R.A. Hulse, L.A. Fowler, G.E. Gullahorn, and J.M. Rankin. Further observations of the binary pulsar psr 1913+ 16. The Astrophysical Journal, 206:L53–L58, 1976.

[10] J.H. Taylor and J.M. Weisberg. A new test of general relativity-gravitational radiation and the binary pulsar psr 1913+ 16. The Astrophysical Journal, 253:908–920, 1982.

[11] J. M. Weisberg and J. H. Taylor. The Relativistic Binary Pulsar B1913+16: Thirty Years of Observations and Analysis. In F. A. Rasio and I. H. Stairs, editors, Binary Radio Pulsars, volume 328 of Astronomical Society of the Pacific Conference Series, 2005.

[12] C.W. Misner, K.S. Thorne, and J.A. Wheeler. Gravitation. WH Freeman, 1973.

[13] P.R. Saulson. Fundamentals of interferometric gravitational wave detectors. 1994.

[14] R.W.P. Drever, J.L. Hall, F.V. Kowalski, J. Hough, G.M. Ford, A.J. Munley, and H. Ward. Laser phase and frequency stabilization using an optical resonator. Applied Physics B: Lasers and Optics, 31(2):97–105, 1983.

[15] E.D. Black. An introduction to pound–drever–hall laser frequency stabilization. American Journal of Physics, 69:79, 2001.

[16] RL Ward, R. Adhikari, B. Abbott, R. Abbott, D. Barron, R. Bork, T. Fricke, V. Frolov, J. Heefner, A. Ivanov, et al. dc readout experiment at the caltech 40m prototype interferometer. Classical and Quantum Gravity, 25(11):114030, 2008.

[17] S. Hild, H. Grote, J. Degallaix, S. Chelkowski, K. Danzmann, A. Freise, M. Hewitson, J. Hough, H. Lück, M. Prijatelj, et al. Dc-readout of a signal-recycled gravitational wave detector. Classical and Quantum Gravity, 26(5):055012, 2009.

[18] T.T. Fricke, N.D. Smith-Lefebvre, R. Abbott, R. Adhikari, K.L. Dooley, M. Evans, P. Fritschel, V.V. Frolov, K. Kawabe, J.S. Kissel, et al. Dc readout experiment in enhanced ligo. Classical and Quantum Gravity, 29(6):065005, 2012.

[19] A. Abramovici, W.E. Althouse, R.W. Drever, Y. Gürsel, S. Kawamura, F.J. Raab, D. Shoemaker, L. Sievers, R.E. Spero, K.S. Thorne, et al. Ligo: The laser interferometer gravitational-wave observatory. Science (New York, NY), 256(5055):325, 1992.

[20] B.P. Abbott, R. Abbott, R. Adhikari, P. Ajith, B. Allen, G. Allen, R.S. Amin, S.B. Anderson, W.G. Anderson, M.A. Arain, et al. Ligo: the laser interferometer gravitational-wave observatory. Reports on Progress in Physics, 72(7):076901, 2009.

[21] C. Bradaschia, R. Del Fabbro, A. Di Virgilio, A. Giazotto, H. Kautzky, V. Montelatici, D. Passuello, A. Brillet, O. Cregut, P. Hello, et al. The virgo project: a wide band antenna for gravitational wave detection. Nuclear Instruments and Methods in Physics Research Section A: Accelerators, Spectrometers, Detectors and Associated Equipment, 289(3):518–525, 1990.

[22] B. Caron, A. Dominjon, C. Drezen, R. Flaminio, X. Grave, F. Marion, L. Massonnet, C. Mehmel, R. Morand, B. Mours, et al. The virgo interferometer for gravitational wave detection. Nuclear Physics B-Proceedings Supplements, 54(3):167–175, 1997.

[23] B. Caron, A. Dominjon, C. Drezen, R. Flaminio, X. Grave, F. Marion, L. Massonnet, C. Mehmel, R. Morand, B. Mours, et al. The virgo interferometer. Classical and Quantum Gravity, 14(6):1461, 1999.

[24] F. Acernese, P. Amico, N. Arnaud, D. Babusci, R. Barille, F. Barone, L. Barsotti, M. Barsuglia, F. Beauville, MA Bizouard, et al. Status of virgo. Classical and Quantum Gravity, 21(5):S385, 2004.

[25] F. Acernese, M. Alshourbagy, P. Amico, F. Antonucci, S. Aoudia, P. Astone, S. Avino, L. Baggio, F. Barone, L. Barsotti, et al. Virgo: a large interferometer for gravitational wave detection started its first scientific run. In Journal of Physics: Conference Series, volume 120, page 032007. IOP Publishing, 2008.

[26] B. Willke, P. Aufmuth, C. Aulbert, S. Babak, R. Balasubramanian, B.W. Barr, S. Berukoff, S. Bose, G. Cagnoli, M.M. Casey, et al. The geo 600 gravitational wave detector. Classical and Quantum Gravity, 19(7):1377, 2002.

[27] B. Willke et al. Geo600: status and plans. Classical and Quantum Gravity, 24(19):S389, 2007.

[28] H. Grote and L.S. Collaboration. The status of geo 600. Classical and Quantum Gravity, 25(11):114043, 2008.

[29] S.R. (contribution by B. S. Sathyaprakash) Edited by Wadia. The Legacy of Albert Einstein: A Collection of Essays in Celebration of the Year of Physics. World Scientific Publishing Company Incorporated, 2007.

[30] A. Weinstein. Advanced ligo optical configuration and prototyping effort. Classical and Quantum Gravity, 19:1575, 2002.

[31] J.R. Smith. The path to the enhanced and advanced ligo gravitational-wave detectors. Classical and Quantum Gravity, 26:114013, 2009.

[32] G.M. Harry. Advanced ligo: the next generation of gravitational wave detectors. Classical and Quantum Gravity, 27:084006, 2010.

[33] G. Losurdo. Ground-based gravitational wave interferometric detectors of the first and second generation: an overview. Classical and Quantum Gravity, 29(12):124005, 2012.

[34] H.B. Callen and T.A. Welton. Irreversibility and generalized noise. Physical Review, 83(1):34–40, 1951.

[35] P.R. Saulson. Thermal noise in mechanical experiments. Physical Review D, 42(8):2437, 1990.

[36] S. Rowan, J. Hough, and D.R.M. Crooks. Thermal noise and material issues for gravitational wave detectors. Physics Letters A, 347(1):25–32, 2005.

[37] Roy J. Glauber. Coherent and incoherent states of the radiation field. Phys. Rev., 131:2766–2788, Sep 1963.

[38] Z. Bialynicka-Birula. Properties of the generalized coherent state. Physical Review, 173(5):1207, 1968.

[39] M.T. Jaekel and S. Reynaud. Quantum limits in interferometric measurements. EPL (Europhysics Letters), 13(4):301, 2007.

[40] A.D. O'Connell, M. Hofheinz, M. Ansmann, R.C. Bialczak, M. Lenander, E. Lucero, M. Neeley, D. Sank, H. Wang, M. Weides, et al. Quantum ground state and single-phonon control of a mechanical resonator. Nature, 464(7289):697–703, 2010.

[41] J.D Teufel, T. Donner, D. Li, J.W. Harlow, M.S. Allman, K. Cicak, A.J Sirois, J.D. Whittaker, K.W. Lehnert, and R.W. Simmonds. Sideband cooling of micromechanical motion to the quantum ground state. Nature, 475(7356):359–363, 2011.

[42] I. Tittonen, G. Breitenbach, T. Kalkbrenner, T. Müller, R. Conradt, S. Schiller, E. Steinsland, N. Blanc, and N. F. de Rooij. Interferometric measurements of the position of a macroscopic body: Towards observation of quantum limits. Phys. Rev. A, 59:1038–1044, Feb 1999.

[43] D. Kleckner, W. Marshall, M.J.A. de Dood, K.N. Dinyari, B.J. Pors, W.T.M. Irvine, and D. Bouwmeester. High finesse opto-mechanical cavity with a movable thirty-micron-size mirror. Physical review letters, 96(17):173901, 2006.

[44] D. Kleckner and D. Bouwmeester. Sub-kelvin optical cooling of a micromechanical resonator. Nature, 444(7115):75–78, 2006.

[45] G.D. Cole, S. Gröblacher, K. Gugler, S. Gigan, and M. Aspelmeyer. Monocrystalline algaas heterostructures for high-reflectivity high-q micromechanical resonators in the megahertz regime. Applied Physics Letters, 92:261108, 2008.

[46] S. Gröblacher, J.B. Hertzberg, M.R. Vanner, G.D. Cole, S. Gigan, KC Schwab, and M. Aspelmeyer. Demonstration of an ultracold micro-optomechanical oscillator in a cryogenic cavity. Nature Physics, 5(7):485–488, 2009.

[47] G.D. Cole, I. Wilson-Rae, M.R. Vanner, S. Groblacher, J. Pohl, M. Zorn, M. Weyers, A. Peters, and M. Aspelmeyer. Megahertz monocrystalline optomechanical resonators with minimal dissipation. In Micro Electro Mechanical Systems (MEMS), 2010 IEEE 23rd International Conference on, pages 847–850. IEEE, 2010.

[48] G.D. Cole, I. Wilson-Rae, K. Werbach, M.R. Vanner, and M. Aspelmeyer. Phonon-tunnelling dissipation in mechanical resonators. Nature Communications, 2:231, 2011.

[49] D. Kleckner, W.T.M. Irvine, S.S.R. Oemrawsingh, and D. Bouwmeester. Diffraction-limited high-finesse optical cavities. Physical Review A, 81(4):043814, 2010.

[50] L. Siegman. University science books. Mill Valley, CA, pages 858–890, 1986.

[51] J.T. Verdeyen. Laser electronics. 1989.

[52] Yu. Levin. Internal thermal noise in the ligo test masses: A direct approach. Phys. Rev. D, 57:659–663, Jan 1998.

[53] D.G Blair, E.J Howell, L. Ju, and C. Zhao. Advanced gravitational wave detectors. Cambridge University Press, 2012.

[54] A. Buonanno and Y. Chen. Scaling law in signal recycled laser-interferometer gravitational-wave detectors. Physical Review D, 67(6):062002, 2003.

[55] T. Corbitt, Y. Chen, E. Innerhofer, H. Müller-Ebhardt, D. Ottaway, H. Rehbein, D. Sigg, S. Whitcomb, C. Wipf, and N. Mavalvala. An all-optical trap for a gram-scale mirror. Physical review letters, 98(15):150802, 2007.

[56] M. Tröbs, S. Barke, J. Möbius, M. Engelbrecht, D. Kracht, L. d'Arcio, G. Heinzel, and K. Danzmann. Lasers for lisa: Overview and phase characteristics. In Journal of Physics: Conference Series, volume 154, page 012016. IOP Publishing, 2009.

[57] R. Riviere, S. Deleglise, S. Weis, E. Gavartin, O. Arcizet, A. Schliesser, and T.J. Kippenberg. Optomechanical sideband cooling of a micromechanical oscillator close to the quantum ground state. Physical Review A, 83(6):063835, 2011.

[58] A. Schliesser, O. Arcizet, R. Rivière, G. Anetsberger, and T.J. Kippenberg. Resolved-sideband cooling and position measurement of a micromechanical oscillator close to the heisenberg uncertainty limit. Nature Physics, 5(7):509–514, 2009.

[59] I. Favero, S. Stapfner, D. Hunger, P. Paulitschke, J. Reichel, H. Lorenz, E.M. Weig, and K. Karrai. Fluctuating nanomechanical system in a high finesse optical microcavity. Optics express, 17(15):12813–12820, 2009.

[60] A.G. Krause, M. Winger, T.D. Blasius, Q. Lin, and O. Painter. A microchip optomechanical accelerometer. arXiv preprint arXiv:1203.5730, 2012.

[61] F. Magaña-Sandoval, R. Adhikari, V. Frolov, J. Harms, J. Lee, S. Sankar, P.R. Saulson, and J.R. Smith. Large-angle scattered light measurements for quantum-noise filter cavity design studies. Arxiv preprint arXiv:1204.2528; accepted to JOSA A, 2012.

[62] R. Dolesi, M. Hueller, D. Nicolodi, D. Tombolato, S. Vitale, PJ Wass, WJ Weber, M. Evans, P. Fritschel, R. Weiss, et al. Brownian force noise from molecular collisions and the sensitivity of advanced gravitational wave observatories. Physical Review D, 84(6):063007, 2011.

[63] S.S. Verbridge, H.G. Craighead, and J.M. Parpia. A megahertz nanomechanical resonator with room temperature quality factor over a million. Applied Physics Letters, 92(1):013112–013112, 2008.

[64] S. Alexander, L. Hellemans, O. Marti, J. Schneir, V. Elings, PK Hansma, M. Longmire, and J. Gurley. An atomic-resolution atomic-force microscope implemented using an optical lever. Journal of Applied Physics, 65(1):164–167, 1989.

[65] N.P. DCosta and J.H. Hoh. Calibration of optical lever sensitivity for atomic force microscopy. Review of scientific instruments, 66(10):5096–5097, 1995.

[66] S.J. Waldman et al. Status of ligo at the start of the fifth science run. Classical and Quantum Gravity, 23(19):S653, 2006.

[67] N. Mavalvala, D. Sigg, and D. Shoemaker. Experimental test of an alignment-sensing scheme for a gravitational-wave interferometer. Applied optics, 37(33):7743–7746, 1998.

[68] H. Okamoto, D. Ito, K. Onomitsu, T. Sogawa, and H. Yamaguchi. Controlling quality factor in micromechanical resonators by carrier excitation. Applied Physics Express, 2(3):5001, 2009.

[69] Yanbei Chen. private communication, 2012.

[70] S. Groeblacher, W. Wieczorek, P. Christ, M. Buehler, D. Wernicke, J. Hoehne, and M. Aspelmeyer. A closed-cycle dilution refrigerator with free-space and fiber optical access for quantum optomechanics experiments at 25mk. Bulletin of the American Physical Society, 56, 2011.

[71] W.Z. Korth, H. Miao, T. Corbitt, G.D. Cole, Y. Chen, and R.X. Adhikari. A quantum radiation pressure noise-free optical spring. arXiv preprint arXiv:1210.0309, 2012.

[72] T. Corbitt and N. Mavalvala. Review: Quantum noise in gravitational-wave interferometers. Journal of Optics B: Quantum and Semiclassical Optics, 6(8):S675, 2004.

[73] T. Corbitt, Y. Chen, F. Khalili, D. Ottaway, S. Vyatchanin, S. Whitcomb, and N. Mavalvala. Squeezed-state source using radiation-pressure-induced rigidity. Physical Review A, 73(2):023801, 2006.

[74] F.Y. Khalili. Optimal configurations of filter cavity in future gravitational-wave detectors. Physical Review D, 81(12):122002, 2010.

[75] F.Y. Khalili. Increasing future gravitational-wave detectors' sensitivity by means of amplitude filter cavities and quantum entanglement. Physical Review D, 77(6):062003, 2008.

[76] T. Corbitt, N. Mavalvala, and S. Whitcomb. Optical cavities as amplitude filters for squeezed fields. Physical Review D, 70(2):022002, 2004.

Appendix A

Standard operating procedure for helium transfer through Janis ST-500 cryostat

The following details the procedure for cooling the cryostat, as initiated by Thomas Corbitt and Shannon Sankar, and instructed/supervised by Richard Mittleman on 4/30/2010. This method may not be the same as the manufacturer recommended method, but for storage dewars with capacities of 30L or more, this is the only feasible procedure.

Cool-down Procedure

(1) Ensure the transfer line has been pumped out, and the cryostat is under vacuum.

(2) Ensure the pressure is in the safe region (0-5psi) and the bleed valve is open.

(3) Ensure the flow regulator on the transfer line is completely open. With the ball valve closed, insert the dewar bayonet into the neck of the dewar. Seal the o-ring finger tight.

(4) Open the ball valve. Close the bleed-off valve. Slowly push the dewar bayonet downwards. The pressure may rise, and one should be able to **carefully** feel cold gas escaping the other end of the transfer line.

(5) Insert the bayonet into the cryostat. Seal the bayonet o-ring finger tight.

(6) Ensure gas is escaping through the helium exhaust end of the cryostat. Ensure the pressure is still within acceptable limits. If not, the bleed valve should be opened immediately to prevent damage to personel and the cryostat.

(7) The cryostat temperature should begin to fall rapidly. Insert the dewar bayonet all the way in, and then retract a few centimeters to prevent frozen debris getting into the line.

(8) Adjust flow regulator to achieve maximum cooling rate with minimum helium flow rate.

(9) Once the base temperature is reached (5.4K or so), reduce flow until the temperature begins to rise slowly. Re-adjust the flow rate to keep the temperature constant at the base temperature, whilst using up a minimum of helium.

(10) Helium gas should not be allowed to build up in the room. This involves a vent line being run to a well-ventilated area.

Warm Up

Cryogenic gloves should be used for this phase of operation.

(1) Close flow regulator. Open bleed valve.

(2) Loosen the o-ring and remove bayonet from cryostat.

(3) Slowly pull the dewar bayonet upwards, until it is nearly out. The bayonet will be **cold** - use of cryogenic gloves is mandatory.

(4) Check to see if the ball valve will close. If not, pull the bayonet out another inch.

(5) Repeat step 4 until the ball valve closes. With the ball valve closed, withdraw the bayonet completely. The bayonet will be **cold** - avoid skin contact.

(6) Place the transfer line in its storage space. Remove the o-ring and nut from the dewar.

(7) Allow the cryostat to warm to room temperature (approximately 48-hour timescale), or use the 25Ω heater to warm the sample block slowly.

Appendix B

Modal masses and eigenfrequencies for device 7

In this Appendix, the FEM-predicted modal masses and eigenfrequencies of Device 7 are recorded. This has proven to be the most useful of the presently available cantilevers, because of two competing factors: limitations on cryogenic actuation range and the desire for light, highly compliant oscillators. The predicted frequencies below have been found to agree with the measured mode frequencies to better than 4% error.

Eigenfrequency (Hz)	Modal Mass (kg)
555.79	1.22E-09
3533.54	1.72E-09
3884.19	1.19E-03
4541.13	2.20E+01
9997.01	2.30E-09
10462.1	6.52E-05
11561	5.67E+00
16768.9	4.95E+00
19713.2	6.90E-06
19756.3	3.04E-09
30634.2	2.27E-06
31852.3	4.79E-01
32875	3.95E-09

38053.1	9.57E+00
43293.7	1.43E-06
49365.7	5.04E-09
59555.1	1.60E-06
62399.7	4.30E+00
68724.3	4.46E-02
69231.8	6.36E-09
79952.3	2.01E-06
92470.4	7.97E-09
103057	1.81E+04
104217	2.45E-06
108746	2.39E+00
119072	9.94E-09
132092	2.89E-06
149027	1.24E-08
153781	2.69E+00
158015	1.83E+00
163489	3.35E-06
182318	1.56E-08
198244	3.99E-06
214508	1.53E+00
215992	4.18E-01
218930	1.98E-08
236030	5.62E-06
258807	2.60E-08

266492	9.61E-07
270724	2.08E-04
281823	9.33E+01
285165	2.39E-01
285840	2.02E-06
302066	3.36E-08
326038	2.97E-06
348540	4.62E-08
352872	9.59E-01
365654	3.29E+00
374240	3.56E-06
393113	2.69E+00

Appendix C

Numerical cavity response transfer functions

In this appendix, the numerical solution to the cavity relations in section 3.7 are presented. The following code is designed to run in Matlab and solves for the transfer functions between any field component (amplitude or phase/frequency) to any other field component. Additionally, the displacement X of the cantilever due to an excitation in any field component can be retrieved. The code utilizes a mechanical susceptibility (coded as "chi") which can be obtained from finite element modeling or by direct measurement.

```
%%%%%%%%%%%%%%%%%%%%%%%%%%%%%%%%%
% Micromirror cavity response   %
%                               %
% modified by SS (12/2011)      %
% modified by SS (08/2011)      %
% modified by TC & SS (05/2011) %
% modified by TC & SS (04/2011) %
% coded by TC (04/2011)         %
%%%%%%%%%%%%%%%%%%%%%%%%%%%%%%%%%

% 8 fields, a-h

%       M1            M2
% a --> || c --> e --> || g -->
% b <-- || d <-- f <-- || h <--
% laser comes in with a (a1 = laser amplitude, a2 = phase/frequency)
% r = b at 0 carrier phase (ie rotate so that r1 is amplitude, r2 is phase)
% t = g at 0 carrier phase ...

hbar = 1e-34;       % reduced Planck's constant
lambda = 1064e-9;   % wavelength of laser light used
L = 0.01;           % cavity length
c = 3e8;            % speed if light
w0 = 2*pi*c/lambda; % optical carrier frequency

T1 = 200e-6;        % mirror 1 properties
R1 = 1-T1;

T2 = 50e-6;         % mirror 2 properties
R2 = 1-T2;

Pin = 10e-6;        % power input
dL = 2;             % detuning in linewidths

dL = dL*lambda*(T1+T2)/8/pi;
f = logspace(3,10,1000);
R = f;


% mechanical suspectibility -- mass at high frequency is reduced mass of
% all modes

freqMass = importdata('dev7_freq_mass.txt'); % imports a file from FEM
resFreqs = freqMass(:,1);
modalMasses = freqMass(:,2);
```

```
chi = 0;
for count=1:length(resFreqs)
    chi = chi+1./(modalMasses(count)*(4*pi*pi*(resFreqs(count).^2-f.^2)+...
            i*f*1e3));
end

% first solve for DC fields
M0 = zeros(8); %M0 * (a--h) = inputs, a=1, b=2, etc
for z = 1:8
    M0(z,z) = -1;
end;


% the coefficient matrix
M0(2,1) = sqrt(R1); %b = rho1 * a + tau1*d
M0(2,4) = sqrt(T1);

M0(3,1) = sqrt(T1); %c = tau1 * a - rho1*d
M0(3,4) = -sqrt(R1);

M0(4,6) = exp(i*w0*dL/c); % d gets phase shift from length

M0(5,3) = exp(i*w0*dL/c); % e gets ...

M0(6,5) = -sqrt(R2); % f = -rho2*e + tau2*h
M0(6,8) = sqrt(T2);

M0(7,5) = sqrt(T2); % g = tau2*e + rho2*h
M0(7,8) = sqrt(R2);

M0(8,8) = 1;
iM0 = inv(M0);
P=1:1:8;
for z=1:8
    P(z) = iM0(z,1)*sqrt(Pin); % amplitude of carrier at each point
end


% solve for sidebands
M = zeros(22);

% indices
a1 = 1;
a2 = 2;
b1 = 3;
b2 = 4;
c1 = 5;
c2 = 6;
```

```
d1 = 7;
d2 = 8;
e1 = 9;
e2 = 10;
f1 = 11;
f2 = 12;
g1 = 13;
g2 = 14;
h1 = 15;
h2 = 16;
X = 17; % small displacement on end mirror
F = 18; % force on end mirror
r1 = 19;
r2 = 20;
t1 = 21;
t2 = 22;

for z = 1:22
    M(z,z) = -1;
end;

for z=1:length(f)
O = -2*pi*f(z); % sideband frequency


M(b1,a1) = sqrt(R1); % b = rho1*a + tau1*d
M(b1,d1) = sqrt(T1);
M(b2,a2) = sqrt(R1);
M(b2,d2) = sqrt(T1);

M(c1,a1) = sqrt(T1); % c = tau1*a - rho1*d
M(c1,d1) = -sqrt(R1);
M(c2,a2) = sqrt(T1);
M(c2,d2) = -sqrt(R1);

M(d1,f1) = exp(i*O*L/c)*cos(w0*dL/c); % phase shift & rotation
M(d1,f2) = exp(i*O*L/c)*sin(w0*dL/c)*-1;
M(d2,f1) = exp(i*O*L/c)*sin(w0*dL/c);
M(d2,f2) = exp(i*O*L/c)*cos(w0*dL/c);

M(e1,c1) = exp(i*O*L/c)*cos(w0*dL/c);
M(e1,c2) = exp(i*O*L/c)*sin(w0*dL/c)*-1;
M(e2,c1) = exp(i*O*L/c)*sin(w0*dL/c);
M(e2,c2) = exp(i*O*L/c)*cos(w0*dL/c);

mag = -2*sqrt(R2)*w0/c/sqrt(hbar*w0)*sqrt(2); %X to reflected field
M(e1,X) = mag*imag(P(5));
M(e2,X) = -mag*real(P(5));
```

```
M(X,F) = chi(z); % suspectibility

mag = sqrt(hbar*w0/c^2); % radiation pressure on end mirror
Pe = P(5);
Pf = P(6);
Pg = P(7);

M(F,e1) = sqrt(2)*real(Pe)*mag;
M(F,e2) = sqrt(2)*imag(Pe)*mag;
M(F,f1) = sqrt(2)*real(Pf)*mag;
M(F,f2) = sqrt(2)*imag(Pf)*mag;
M(F,g1) = sqrt(2)*real(Pg)*mag;
M(F,g2) = sqrt(2)*imag(Pg)*mag;


M(f1,e1) = -sqrt(R2); % f = tau1*h - rho1*e
M(f1,h1) = sqrt(T2);
M(f2,e2) = -sqrt(R2);
M(f2,h2) = sqrt(T2);

M(g1,e1) = sqrt(T2); % g = rho1*e + tau1*h
M(g1,h1) = sqrt(R2); %
M(g2,e2) = sqrt(T2);
M(g2,h2) = sqrt(R2);

M(r1,b1) = cos(-phase(P(2)));
M(r1,b2) = -sin(-phase(P(2)));
M(r2,b1) = sin(-phase(P(2)));
M(r2,b2) = cos(-phase(P(2)));

M(t1,g1) = cos(-phase(P(7)));
M(t1,g2) = -sin(-phase(P(7)));
M(t2,g1) = sin(-phase(P(7)));
M(t2,g2) = cos(-phase(P(7)));

warning('off')
iM = inv(M);
warning('on')

%R(z) = iM(X,F);  % response including optical spring
%R(z) = sqrt(abs(iM(X,a1)).^2+abs(iM(X,a2)).^2); % displacement
%caused by shot noise of incoming laser
R(z) = iM(t1,a1); % transfer function of input to transmitted
end
```

```
loglog(f,abs(R),'k')
xlim([2e3 25e5])
xlabel('Frequency (Hz)','fontsize',24)
ylabel('Magnitude','fontsize',24)
grid minor
```

Appendix D

Measurements on superpolished, supercoated mirrors

This appendix contains the reflectivity measurements of a batch of custom low-scatter, low-loss mirrors. These mirrors are utilized in the 1gram ponderomotive experiment as well as the H1 squeezer experiment.

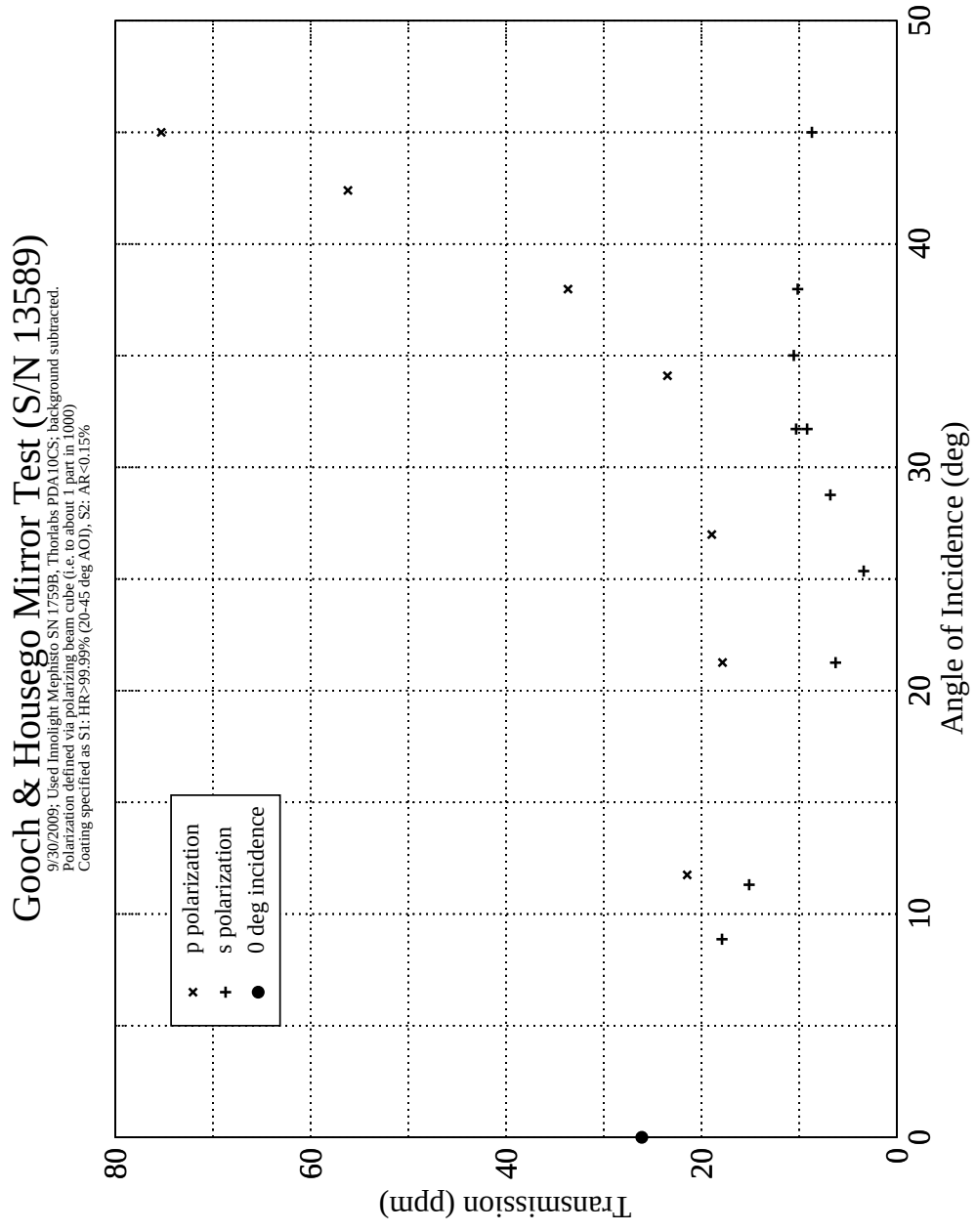
Gooch & Housego Mirror Test (S/N 13589)
9/30/2009; Used Innolight Mephisto SN 1759B, Thorlabs PDA10CS; background subtracted.
Polarization defined via polarizing beam cube (i.e. to about 1 part in 1000)
Coating specified as S1: HR>99.99% (20-45 deg AOI), S2: AR<0.15%
p polarization
s polarization
0 deg incidence
Transmission (ppm)
Angle of Incidence (deg)
0
20
40
60
80
0
10
20
30
40
50

Appendix E

Electronic diagrams

This appendix houses the schematics of electronics used in the experiment for the purpose of documentation. Additionally, many LIGO designs were utilized and can be found on the LIGO Document Center.

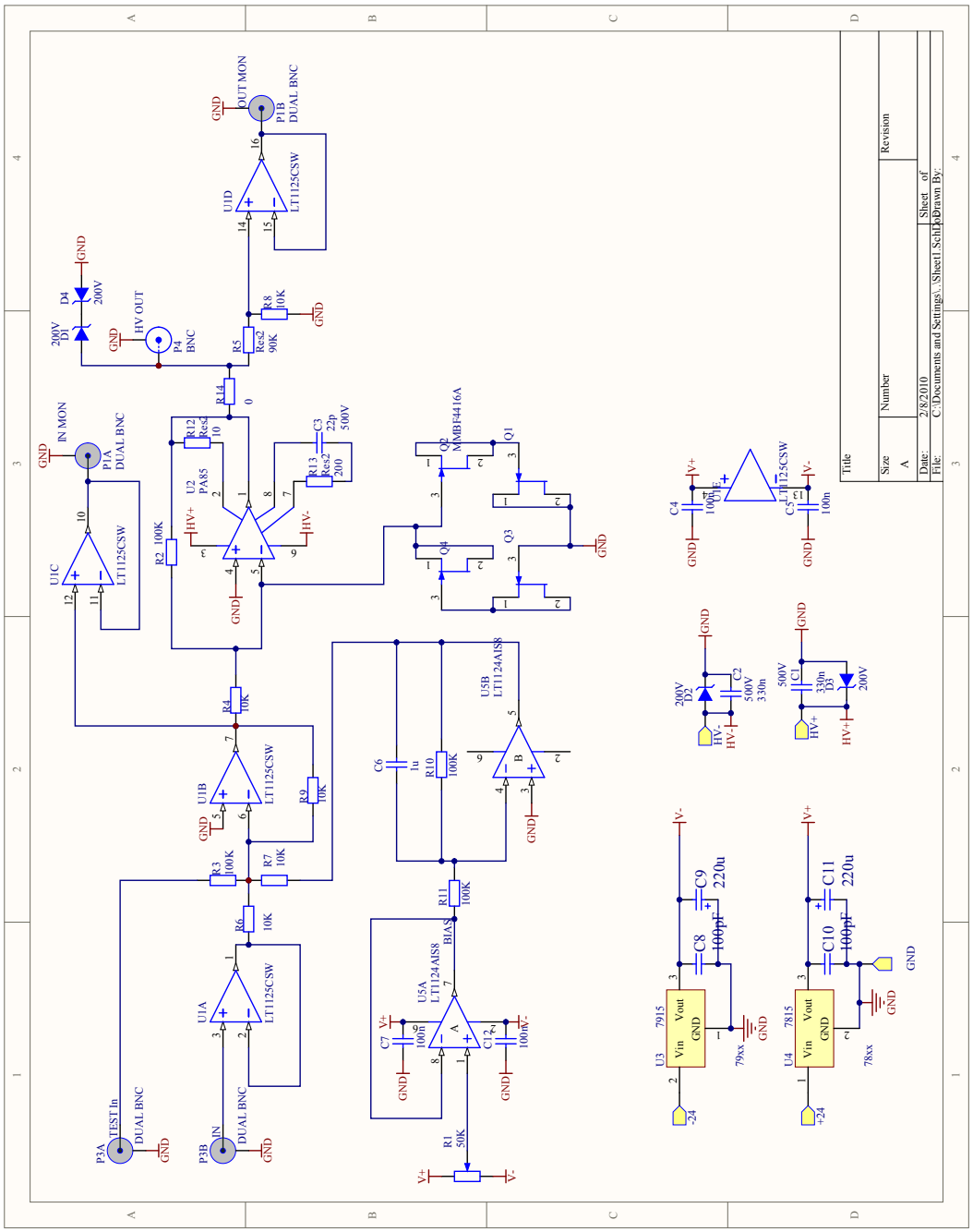
Title
Size
A
Number
Revision
Date: 2/8/2010
Sheet of
File: C:\Documents and Settings\...\Sheet1.SchDoc
Drawn By:
OUT MON
P1B
DUAL BNC
LT1125CSW
U1D
D4
200V
D1
200V
HV OUT
P4
BNC
R5
Res2
90K
R8
10K
R14
0
IN MON
P1A
DUAL BNC
U1C
R12
Res2
10
R13
Res2
200
C3
22p
500V
U2
PA85
R2 100K
MMBF4416A
Q2
Q1
Q4
Q3
R4
10K
U1B
R9
10K
R3
100K
R7
10K
R6
10K
U1A
C6
1u
R10
100K
U5B
LTT124AIS8
R11
100K
U5A
LTT124AIS8
C7
100n
C12
100n
R1
50K
TEST In
P3A
DUAL BNC
P3B
IN
DUAL BNC
C4
100n
C5
100n
200V
D2
C2
500V
330n
500V
C1
330n
D3
200V
C9
220u
C8
100pF
U3
7915
Vin
Vout
GND
79xx
-24
C11
220u
C10
100pF
U4
7815
78xx
+24

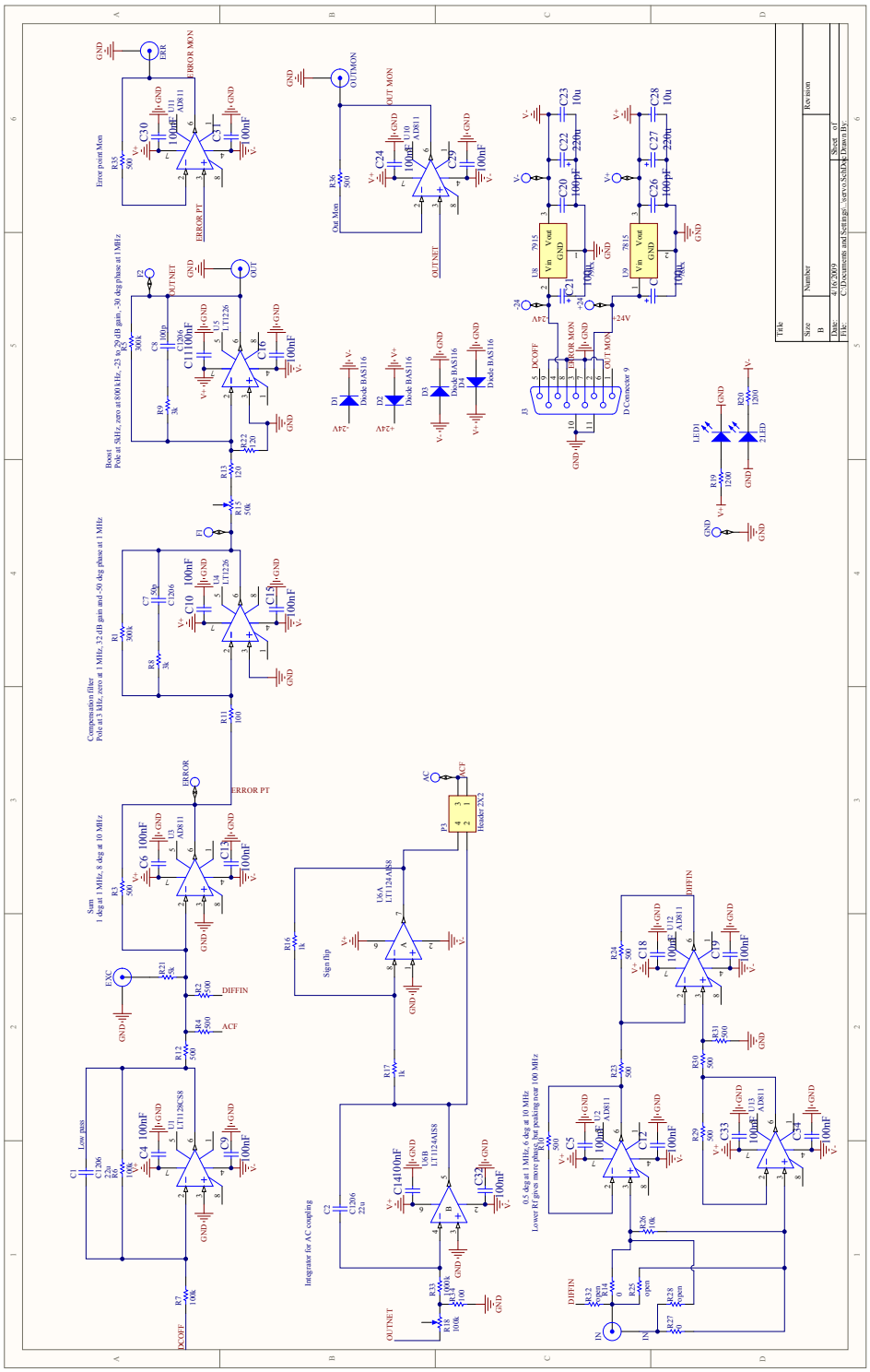
Error point Mon
Out Mon
Boost
Pole at 5kHz, zero at 800 kHz, -23 to 29 dB gain, -30 deg phase at 1MHz
Compensation filter
Pole at 3 kHz, zero at 1 MHz, 3.2 dB gain and -50 deg phase at 1 MHz
Sum
1 deg at 1 MHz, 8 deg at 10 MHz
Low pass
Sign flip
Integrator for AC coupling
0.5 deg at 1 MHz, 6 deg at 10 MHz
Lower Rf gives more phase, less peaking near 100 MHz
D Connector 9
Header 2X2
Title
Size
B
Number
Revision
Date:
4/16/2009
Sheet of
File:
C:\Documents and Settings\...\servoSchX.sch
Drawn By:

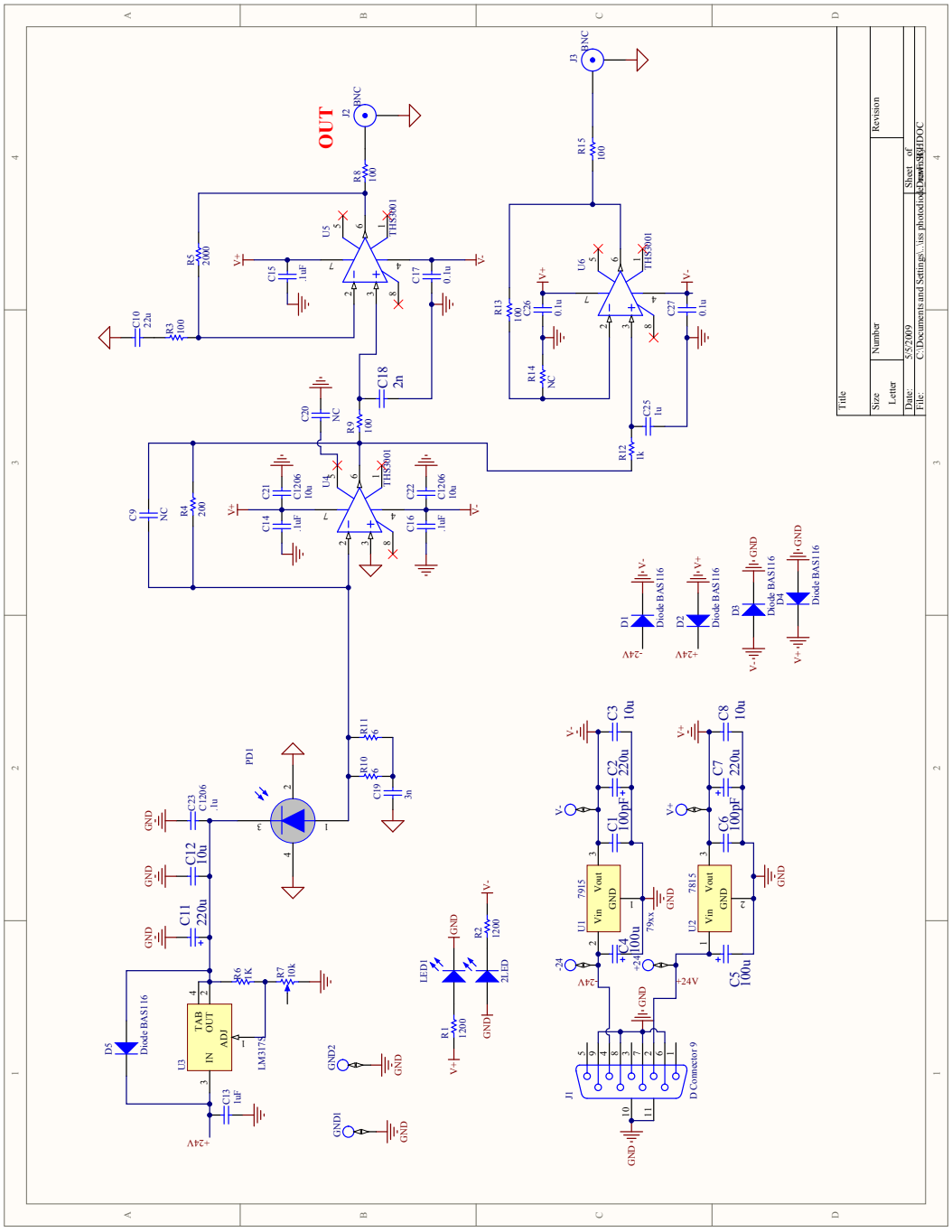
OUT
J2 BNC
J3 BNC
R8 100
R15 100
R5 2000
R3 100
C10 22u
U5 THS3001
U6 THS3001
U4 THS3001
C15 .1uF
C17 0.1u
C18 2n
C20 NC
R9 100
C21 C1206 10u
C14 .1uF
C22 C1206 10u
C16 .1uF
C9 NC
R4 200
R13 100
C26 0.1u
R14 NC
C27 0.1u
C25 1u
R12 1k
D1 Diode BAS116
D2 Diode BAS116
D3 Diode BAS116
D4 Diode BAS116
PD1
R11 26
R10 26
C19 3n
C23 C1206 .1u
C12 10u
C11 220u
R6 1K
R7 10k
U3 LM317
TAB OUT IN ADJ
D5 Diode BAS116
C13 1uF
LED1 2LED
R2 1200
R1 1200
GND2
GND1
C1 100pF
C2 220u
C3 10u
U1 7915
C4 100u
C6 100pF
C7 220u
C8 10u
U2 7815
C5 100u
J1 D Connector 9
L1 10
Title
Size Letter
Number
Revision
Date: 5/5/2009
Sheet of
File: C:\Documents and Settings\...\ths photodiode.SchDoc
Drawn By: